

# **Modeling and measuring the effects of individually optimized multi-channel transcranial direct current stimulation on the human brain**

Dissertation  
Zur Erlangung des akademischen Grades  
Doktor-Ingenieur (Dr.-Ing.)

vorgelegt der Fakultät für Informatik und Automatisierung  
Technischen Universität Ilmenau

**M.Sc. Asad khan**

**Vorgelegt am:**

**Gutachter:**

- 1.
- 2.
- 3.

# *Abstract*

Transcranial direct current stimulation (tDCS) is a non-invasive neuromodulation technique that uses weak currents sent through electrodes on the scalp to transiently alter characteristics of the brain. Targeting specific cortical areas researchers have employed tDCS to influence motor functioning, emotion, memory, language processing and various other cognitive functions. Conventionally, a standard bipolar montage is used in tDCS to stimulate a certain brain region of interest that resulted in variable outcomes throughout the literature. Recently, multi-channel tDCS (mc-tDCS) optimization methods have gained interest in accurately targeting a specific brain area that have the potential to produce more controlled and consistent results. In this thesis, a novel mc-tDCS approach, the distributed constrained maximum intensity approach (D-CMI), is proposed to stimulate the human brain's somatosensory P20/N20 target source at Brodmann area 3b. To reconstruct the P20/N20 target source at Brodmann area 3b accurately for tDCS, an integrated and combined magnetoencephalography (MEG) and electroencephalography (EEG) source analysis with individualized skull conductivity calibrated realistic head modeling is proposed. The D-CMI method is investigated targeting the somatosensory P20/N20 target source at Brodmann area 3b with first a simulation study and then experimental validation study. In the simulation study, simulated electric fields (EF) for the new D-CMI method and the already known state of the art maximum intensity (MI) and standard bipolar methods were produced and compared for the individualized P20/N20 somatosensory targets. The practical applicability of the D-CMI approach is tested in an experimental study to stimulate the somatosensory P20/N20 target source in Brodmann area 3b and compare it with standard bipolar tDCS and Sham tDCS conditions. For comparisons, recording of the electrically finger stimulated somatosensory evoked fields (SEF) data before and after the application of the three different tDCS conditions (D-CMI, standard bipolar and Sham) is conducted. Specifically, the 20ms SEF peak amplitudes are compared before and after the application of the three tDCS condition to test the performance of D-CMI compared to Sham and standard bipolar tDCS.

The results obtained in this thesis from the simulation study showed that the individualized D-CMI mc-tDCS montages showed high current intensities at the target compared to the standard bipolar method. Another aspect of individualized D-CMI montages is potentially reduced side effects and skin sensations. In this regard, the D-CMI takes into account the most important stimulation parameters such as high target directionality (DIR) with the potential of lower skin sensations and electric field amplitude in distant brain areas. The statistical comparisons 20ms SEF peak amplitudes from the experimental study in this thesis showed that the D-CMI approach outperforms the standard bipolar tDCS approach targeting the somatosensory Brodmann area 3b. Reduced skin sensation and consistency throughout the experiment with D-CMI based sham conditioning was also successful.

In conclusion, individualized mc-tDCS D-CMI montages provide a good balance between high current intensities at the target and reduced side effects and skin sensations. The results in this thesis indicate that the D-CMI method together with highly individualized skull conductivity calibrated realistic head modeling can lead to better control over stimulation outcomes outperforming the standard tDCS methods. An integrated combined MEG and EEG source analysis with D-CMI montages for mc-tDCS stimulation potentially can improve control, reproducibility and reduce sensitivity differences between sham and real simulations.

# Zusammenfassung

Die transkranielle Gleichstromstimulation (tDCS) ist eine nicht-invasive Technik zur Neuro-Modulation, bei der schwache Ströme durch Elektroden auf der Kopfhaut gesendet werden, um die Eigenschaften des Gehirns vorübergehend zu verändern. Durch die gezielte Beeinflussung bestimmter kortikaler Bereiche haben Forscher die tDCS eingesetzt, um Motorik, Emotionen, Gedächtnis, Sprachverarbeitung und verschiedene andere kognitive Funktionen zu beeinflussen. Konventionell wird bei der tDCS eine bipolare Standardmontage verwendet, um eine bestimmte Hirnregion von Interesse zu stimulieren, was in der Literatur zu unterschiedlichen Ergebnissen führte. In jüngster Zeit haben Optimierungsmethoden für die mehrkanalige tDCS (mc-tDCS) an Interesse gewonnen, die genau auf einen bestimmten Hirnbereich abzielen und das Potenzial haben, kontrolliertere und konsistentere Ergebnisse zu erzielen. In dieser Arbeit wird ein neuartiger mc-tDCS-Ansatz, der Distributed Constrained Maximum Intensity Approach (D-CMI), vorgeschlagen, um die somatosensorische P20/N20-Zielquelle des menschlichen Gehirns im Brodmann-Areal 3b zu stimulieren. Um die P20/N20-Zielquelle im Brodmann-Areal 3b für die tDCS genau zu rekonstruieren, wird eine integrierte und kombinierte Magnetoenzephalographie (MEG) und Elektroenzephalographie (EEG) Quellenanalyse mit individualisierter, auf die Leitfähigkeit des Schädels kalibrierter realistischer Kopfmodellierung vorgeschlagen. Die D-CMI-Methode wird für die somatosensorische P20/N20-Zielquelle im Brodmann-Areal 3b zunächst in einer Simulationsstudie und anschließend in einer experimentellen Validierungsstudie untersucht. In der Simulationsstudie wurden simulierte elektrische Felder (EF) für die neue D-CMI-Methode und die bereits bekannten, dem Stand der Technik entsprechenden Maximalintensitäts- (MI) und Standard-Bipolarmethoden erzeugt und für die individualisierten somatosensorischen P20/N20-Ziele verglichen. Die praktische Anwendbarkeit des D-CMI-Ansatzes wird in einer experimentellen Studie zur Stimulation der somatosensorischen P20/N20-Zielquelle im Brodmann-Areal 3b getestet und mit bipolaren Standard-TDCS- und Sham-TDCS-Bedingungen verglichen. Für den Vergleich werden die Daten der mit dem Finger elektrisch stimulierten somatosensorisch evozierten Felder (SEF) vor und nach der Anwendung der drei verschiedenen tDCS-Bedingungen (D-CMI, bipolare Standard- und Sham-Bedingungen) aufgezeichnet. Insbesondere werden die 20ms SEF-Spitzenamplituden vor und nach der Anwendung der drei tDCS-Bedingungen verglichen, um die Leistung von D-CMI im Vergleich zu Sham und bipolarer Standard-TDCS zu testen.

Die in dieser Arbeit aus der Simulationsstudie gewonnenen Ergebnisse zeigten, dass die individualisierten D-CMI mc-tDCS-Montagen im Vergleich zur bipolaren Standardmethode hohe Stromintensitäten am Ziel zeigten. Ein weiterer Aspekt der individualisierten D-CMI-Montagen ist die potenzielle Reduzierung von Nebenwirkungen und Hautempfindungen. In dieser Hinsicht berücksichtigt die D-CMI die wichtigsten Stimulationsparameter, wie z. B. eine hohe Zielgerichtetheit (DIR) mit dem Potenzial geringerer Hautsensationen und elektrischer Feldamplituden in entfernten Hirnarealen.

Die statistischen Vergleiche der 20ms SEF-Spitzenamplituden aus der experimentellen Studie in dieser Arbeit zeigten, dass der D-CMI-Ansatz den bipolaren Standard-TDCS-Ansatz, der auf das somatosensorische Brodmann-Areal 3b abzielt, übertrifft. Eine reduzierte Hautempfindung und Konsistenz während des gesamten Experiments mit D-CMI-basierter Scheinkonditionierung war ebenfalls erfolgreich.

Zusammenfassend lässt sich sagen, dass individualisierte mc-tDCS D-CMI-Montagen ein gutes Gleichgewicht zwischen hohen Stromintensitäten am Zielort und reduzierten Nebenwirkungen und Hautempfindungen bieten. Die Ergebnisse dieser Arbeit zeigen, dass die D-CMI-Methode in Verbindung mit einer hochindividualisierten, kalibrierten Schädelkonduktivität und einer realistischen Kopfmodellierung zu einer besseren Kontrolle der Stimulationsergebnisse führen kann als die Standard-tDCS-Methoden. Eine integrierte kombinierte MEG- und EEG-Quellenanalyse mit D-CMI-Montagen für die mc-tDCS-Stimulation kann möglicherweise die Kontrolle und Reproduzierbarkeit verbessern und die Empfindlichkeitsunterschiede zwischen Schein- und realen Simulationen verringern.

# *Acknowledgements*

I would like to show my gratitude to people who supported me during my PhD studies, particularly:

- My thesis supervisor Prof. Dr. rer. nat. Carsten Wolters who motivated me to come to Germany giving me the great opportunity to do my studies in an interdisciplinary environment, advised me valuably (for scientific and non-scientific aspects) and guided me in a professional manner.
- Prof. Dr.-Ing. Jens Haueisen for accepting me as a PhD student and his scientific support.
- Prof. Dr.-Ing. Christo Pantev and Prof. Dr. Joachim Gross for giving me a safe place at the Institute for Biomagnetism and Biosignalanalysis in Münster and for sharing their scientific knowledge.
- Andreas Wollbrink for helping me with the setups of the experiments and the technical issues. Karin, Hildegard and Ute for their help with the EEG, MEG, MRI measurements.
- All my colleagues at IBB for a friendly working environment.
- My family for their significant support throughout my PhD.

Finally, I am grateful to thank Prof. Dr. rer. nat. Carsten Wolters for the funding of this PhD by the Bundesministerium für Gesundheit (BMG as project ZMI1-2521FSB006, under the frame of ERA PerMed as project ERAPERMED2020-227, by the Deutsche Forschungsgemeinschaft (DFG, projects WO1425/10-1 and WO1425/5 2), by DAAD (project 57523877) and by the Onassis Scholarship Foundation to MA). Special thanks also to the Alexander Onassis"Foundation for accepting me as scholar and supporting my PhD studies.

# Contents

<b>List of Figures</b>	<b>ix</b>
<b>List of Tables</b>	<b>xi</b>
<b>List of Abbreviations</b>	<b>xii</b>
<b>1 Introduction</b>	<b>1</b>
1.1 Thesis motivation and contribution . . . . .	1
1.2 Organization of thesis . . . . .	3
<b>2 Basics and theory</b>	<b>5</b>
2.1 The human brain . . . . .	5
2.2 Neuronal basis . . . . .	7
2.3 History of transcranial electrical stimulation (tES) . . . . .	9
2.4 Transcranial direct current stimulation (tDCS) . . . . .	12
2.4.1 Stimulation parameters . . . . .	12
2.4.2 Neurophysiological mechanisms for tDCS . . . . .	14
2.4.3 Measurement of tDCS effects . . . . .	14
2.4.4 Safety of tDCS . . . . .	17
2.4.5 Sham stimulation . . . . .	17
2.4.6 Clinical applications of tDCS . . . . .	18
2.5 The human somatosensory system . . . . .	18
2.6 Somatosensory evoked responses . . . . .	20
2.7 Measurement modalities . . . . .	22
2.7.1 Overview . . . . .	22
2.7.2 MRI (magnetic resonance imaging) . . . . .	22
2.7.3 EEG and MEG . . . . .	24
2.8 Realistic volume conduction modeling . . . . .	25
2.9 Theoretical basis for source analysis . . . . .	28
2.9.1 Overview . . . . .	28
2.9.2 EEG and MEG forward modeling . . . . .	29
2.9.2.1 Forward problem . . . . .	29
2.9.2.2 Forward solution . . . . .	31
2.9.3 Inverse modeling for EEG and MEG . . . . .	32
2.9.3.1 Inverse problem . . . . .	32
2.9.3.2 Inverse algorithm . . . . .	33
2.9.4 Combined EEG and MEG source analysis . . . . .	34

<b>3</b>	<b>A novel mc-tDCS optimization method with integrated EEG/MEG source analysis</b>	<b>35</b>
3.1	Introduction . . . . .	35
3.2	Methods and materials . . . . .	37
3.2.1	Subjects . . . . .	37
3.2.2	EEG and MEG parameters . . . . .	37
3.2.3	SEP and SEF measurement and pre-processing . . . . .	38
3.2.4	MRI measurements and parameters . . . . .	39
3.2.5	Source reconstruction pipeline . . . . .	39
3.2.5.1	Realistic head segmentation . . . . .	40
3.2.5.2	Mesh creation . . . . .	40
3.2.5.3	Tissue compartment conductivities . . . . .	41
3.2.5.4	Source space creation . . . . .	41
3.2.5.5	EEG and MEG leadfields creation . . . . .	42
3.2.5.6	Individualized skull conductivity calculation . . . . .	42
3.2.5.7	Somatosensory source reconstruction . . . . .	43
3.3	tDCS forward modeling . . . . .	44
3.4	Multi-channel tDCS formulation and optimization methods . . . . .	44
3.4.1	Overview . . . . .	44
3.4.2	Alternating direction method of multipliers (ADMM) . . . . .	46
3.4.3	Maximum intensity (MI) . . . . .	47
3.4.4	Distributed constrained maximum intensity (D-CMI) . . . . .	48
3.5	Standard 2 – Patch . . . . .	49
3.6	Quantification metrics . . . . .	49
3.7	Results . . . . .	50
3.7.1	Individualized head modeling . . . . .	50
3.7.2	Somatosensory targeting . . . . .	51
3.7.3	Individual parameter identification study for D-CMI . . . . .	52
3.7.3.1	Parameter investigation for a single subject . . . . .	52
3.7.3.2	Parameter investigation for a group of subjects . . . . .	54
3.7.4	Comparison of the tDCS methods . . . . .	57
3.7.4.1	Visual analysis . . . . .	57
3.7.4.2	Statistical analysis . . . . .	60
3.8	Discussion . . . . .	63
3.8.1	Targeted mc-tDCS using MEG/EEG source analysis . . . . .	63
3.8.2	Comparison of stimulation methods and contribution of D-CMI compared to MI and CMI . . . . .	64
3.8.3	Potential of D-CMI . . . . .	66
<b>4</b>	<b>Targeted and individually optimized mc-tDCS experimental stimulation of the somatosensory cortex</b>	<b>68</b>
4.1	Introduction . . . . .	68
4.2	Materials and methods . . . . .	70
4.2.1	Subjects . . . . .	70
4.2.2	Data acquisition for source reconstruction and tDCS targeting . . . . .	70
4.2.2.1	MRI data acquisition and registration . . . . .	70

4.2.2.2	SEP and SEF measurement and pre-processing	70
4.2.3	Source analysis and tDCS montage simulations	70
4.2.4	Source reconstruction in calibrated head models	72
4.2.5	Generation of tDCS montages	72
4.3	Experimental design	73
4.4	Data analysis	75
4.5	Results	76
4.6	Discussion	83
<b>5</b>	<b>Analysing inter-individual variability for simulated individually optimized transcranial electric fields</b>	<b>89</b>
5.1	Introduction	89
5.2	Materials and methods	89
5.2.1	Participants	90
5.2.2	Data acquisition	90
5.2.3	FEM head models	90
5.2.4	Simulated brain targets and scalp electrodes	91
5.2.5	Multi-channel inverse optimization montages and induced electric fields flow simulations	92
5.2.6	Quantification and statistical analysis of modeling results	93
5.3	Results and discussion	94
5.3.1	Individual targeting adapts to individual stimulation requirements	94
5.3.2	Targeted electric field orientations	96
5.3.3	Targeted stimulation intensities	98
5.3.4	Targeted electric field distribution and bias	100
5.3.5	Homogeneity of electric fields across target orientations	104
5.3.6	Target dependent individual stimulation profiles	104
5.4	Conclusion	105
5.5	Author's contribution	106
<b>6</b>	<b>Conclusion and outlook</b>	<b>107</b>
6.1	Summary	107
6.2	Discussion and future perspective	108

# List of Figures

2.1	The basic structure of a human brain. <b>(a)</b> The human brain structure divided into different lobes <b>(b)</b> The internal structure of the human brain. (adapted from bioninga.com) . . . . .	6
2.2	Neuronal anatomy and mechanism . . . . .	8
2.3	The above illustration shows the application of galvanism to patients . . . . .	10
2.4	The above two Figures show the intracortical recording of anesthetized animals . . . . .	11
2.5	Different types of devices for applying transcranial electrical stimulation(tES) . . . . .	12
2.6	Different waveforms for tES produced by commercially available hardware (adapted from [35]) . . . . .	13
2.7	Direction of current flow and effects on neurons . . . . .	15
2.8	The measurement of MEPs with TMS and EMG . . . . .	16
2.9	The signaling pathway for the human somatosensory system . . . . .	19
2.10	Somatic sensory areas of the cortex . . . . .	21
2.11	Three different MRI images are shown . . . . .	23
2.12	EEG and MEG schematics of sensor positions . . . . .	24
3.1	Finite element (FEM) mesh . . . . .	40
3.2	Source space . . . . .	42
3.3	MEG and EEG sensors with topographies 20 ms . . . . .	51
3.4	D-CMI approach for a single subject . . . . .	53
3.5	Relationship between $\lambda$ (0–2000), number of tDCS electrodes . . . . .	55
3.6	Directionality (DIR) boxplots (10 subjects) . . . . .	56
3.7	Optimized montages for the three methods . . . . .	58
3.8	Current density distributions and montages for the different stimulation approaches . . . . .	59
3.9	Performance of ADMM, MI and D-CMI . . . . .	60
4.1	Schematic diagram of the simulation pipeline for targeting . . . . .	71
4.2	Experimental design to stimulate the somatosensory S1 with transcranial direct current stimulation (tDCS) . . . . .	74
4.3	The results for the D-CMI mc-tDCS method are shown . . . . .	77
4.4	Grand averaged source waveforms of M20 are shown . . . . .	78
4.5	After effects of the three tDCS stimulation conditions . . . . .	80
4.6	T-value topography differences . . . . .	81
5.1	Isosurfaces of SC, GM and WM compartments . . . . .	91

5.2	Three-dimensional illustration of the grand average electrode montages . . . . .	95
5.3	Close-up of the finite-element vector field and target vectors for all methods . . . . .	97
5.4	Target current densities (CD) plotted . . . . .	99
5.5	Close-up of the finite-element vector field and target vectors for all methods (from left to right . . . . .	101

## List of Tables

3.1	Results of a one-way repeated measures ANOVA . . . . .	61
3.2	Results are shown for post-hoc paired-samples t-test . . . . .	62
3.3	Maximum injected currents at anodes for D-CMI . . . . .	63
4.1	The table shows mean and standard deviation . . . . .	79
4.2	Results of a two way repeated measures ANOVA (RM-ANOVA)	79
4.3	M20 source waveform peak amplitude results are shown for post-hoc paired-samples t-test . . . . .	79
4.4	Group comparisons on intensity of perceived sensations (Itch- ing, Pain, Burning and Warmth/Heat) . . . . .	82
4.5	The judgment of perceived stimulation as real or sham is shown	82
5.1	Descriptive data for the bias and parallelity of the current den- sity vector field . . . . .	96
5.2	Results of repeated measures ANOVA's testing differences in target intensity and spatial extent . . . . .	102
5.3	Follow-up t-tests of the method x target orientation interaction	102

# List of Abbreviations

<b>ADMM</b>	Alternating direction of method of multiplier
<b>AMG-CG</b>	Algebraic MultiGrid preconditioned Conjugate Gradient
<b>ANOVA</b>	Analysis of variance
<b>BEM</b>	Bounded element method
<b>CI</b>	Confidence interval
<b>CMI</b>	Constrained maximum intensity
<b>CSF</b>	Cerebrospinal fluid
<b>CT</b>	Computed tomography
<b>DIR</b>	Directionality
<b>DT-MRI</b>	Diffusion tensor MRI
<b>DTI</b>	Diffusion tensor imaging
<b>EEG</b>	Electroencephalography
<b>ERP</b>	Evoked response potential
<b>EIT</b>	Electric impedance tomography
<b>EEG/MEG</b>	Combined EEG and MEG
<b>EMG</b>	Electromyography
<b>EP</b>	Evoked potential
<b>FOC</b>	Focality
<b>FDM</b>	Finite difference method
<b>FDI</b>	First dorsal interosseous
<b>FEM</b>	Finite element method
<b>GM</b>	Grey matter
<b>GOF</b>	Godness of fit
<b>IT</b>	Intensity in target region
<b>INT</b>	Intensity in non-target regions
<b>LVGCC</b>	L-type voltage gated calcium channel
<b>MEG</b>	Magnetoencephalography
<b>MEP</b>	Motor evoked potential
<b>MRI</b>	Magnetic resonance imaging
<b>M1</b>	Primary motor
<b>M20</b>	SEF component and 20ms
<b>NMDA</b>	N-methyl-D-aspartate
<b>PAR</b>	Parallelity
<b>PET</b>	Positron emission tomography
<b>P20/N20</b>	SEP component at 20ms
<b>ROI</b>	Region of interest
<b>RV</b>	Residual variance
<b>RF</b>	Radio frequency
<b>SC</b>	Skull compacta
<b>SDS</b>	Single dipole scans

<b>SEF</b>	Somatosensory evoked fields
<b>SEP</b>	Somatosensory evoked potentials
<b>SI</b>	Primary somatosensory cortex
<b>SOA</b>	Contralateral supraorbital area
<b>SS</b>	Skull spongiosa
<b>T1w MRI</b>	T1-weighted magnetic resonance imaging
<b>T2w MRI</b>	T2-weighted magnetic resonance imaging
<b>tES</b>	Transcranial electrical stimulation
<b>tDCS</b>	Transcranial direct current stimulation
<b>TMS</b>	Transcranial magnetic stimulation
<b>VP</b>	ventral posterior
<b>WM</b>	White matter

# 1 Introduction

## 1.1 Thesis motivation and contribution

Transcranial electrical stimulation (tES) is one of the various non-invasive neuromodulatory techniques which incorporated passing a mild electric current to cortical regions of the brain through electrodes placed on the scalp. The effects of tES, after applying it for a few minutes or more, can modulate brain activity in the targeted regions which can outlast the duration of the stimulation for upto or beyond minutes to hours [1], [2]. The most commonly used form of tES is transcranial direct current stimulation (tDCS). In tDCS direct current (constant flow of electric charge) is applied transcranially which effects the polarization of neuronal tissue. Neuronal tissue polarization causes a shift in neuronal membrane potential which affects neuronal excitability. The applications of tDCS by researches for specific cortical areas have shown that tDCS can influence motor functioning, emotion, memory, language processing and various other cognitive functions. There have been increasing number of positively reported results that aimed at improving functioning in both healthy people and patients suffering from depression and epilepsy. There exists, however, a significant discrepancy with the application of tDCS in individualized patient's efficacy. This leads to inter-subject variability in various studies and applications. Various studies have emphasized that although the in-going current to the brain is the same, the electric field experienced by the brain varies among subjects due to anatomical differences. So in this regard, it is very important to individually optimize the stimulation parameters before application.

Optimization of the stimulation parameters individually requires computational realistic head volume conduction modeling. Volume conduction modeling remains the most viable option to calculate the electric field inside the brain before experimental stimulation. The experimental tDCS stimulation parameters can be individually optimized if a realistic head model takes into account the neuronal target's location and orientation in the brain individually. Such simulations can provide insights before stimulation such as (a) the maximal electric field in the targeted region and (b) the direction of the electric field relative to neuronal fibers of the targeted region.

Electroencephalography (EEG) and magnetoencephalography (MEG) are two complementary modalities that measure the underlying brain activity recorded at the scalp. Using a combined EEG and MEG source analysis (forward and inverse modeling) approach, the individualized location and orientation of the targeted neurons can be accurately estimated. Moreover,

usually standard conductivity values are used in research for different tissue compartments in realistic head volume modeling while in reality, considerable inter-subject variability exists for the conductivity values [3], [4]. Skull conductivity is the most affected parameter in head modeling while conducting source analysis for EEG [5], [6] and tDCS simulations. Magnetic resonance imaging (MRI) integrated with combined EEG/MEG is proposed for this thesis to individually estimate the skull conductivity which leads to individualized source reconstruction of the underlying target's location and orientation.

Traditionally, a standard bipolar montage (positively charged patch anode and negatively charged patch cathode) is used to stimulate the brain in tDCS. The bipolar montage affects a larger area of the brain which (a) can lead to inter-subject variability [7], [8], as they do not consider an individualized (location and orientation) targeting approach and (b) makes it difficult to target a specific region in the brain. Recently, advances in multi-channel tDCS (mc-tDCS) hardware and electrode optimization approaches [9]–[15] has made it possible to individually optimize a montage that takes into account the individually estimated location and orientation of a subject's or patient's targeted region. For this thesis work, the chosen brain region of interest (ROI) is the somatosensory network, specifically, the somatosensory Brodmann area 3b in the primary somatosensory cortex. The somatosensory network is a thoroughly researched and reproducible network when measured with EEG and MEG [16]. In this thesis work, significant importance is given to the reconstruction of the underlying neuronal activity of somatosensory evoked fields (SEF) and potentials (SEP) 20 ms component at the Brodmann area 3b. The reconstruction of the 20 ms component at Brodmann area 3b is first individually estimated with combined EEG/MEG source analysis and then individually optimized mc-tDCS montages are created to be later validated in a tDCS experimental paradigm.

One of the main contributions of this thesis work is a study that proposes of a novel mc-tDCS approach, the distributed constrained maximum intensity (D-CMI). In this study, the D-CMI is developed and investigated while targeting the reconstructed combined EEG/MEG P20/N20 dipole component at the Brodmann area 3b from source analysis. In this study, the D-CMI approach is compared, in simulations, to the standard bipolar tDCS and the state-of-the-art current intensity and focality based tDCS approaches such as the maximum intensity (MI) and the alternating direction method of multipliers (ADMM), respectively. Moreover, to the best of our knowledge, the novelty also comes from the fact that this study conducts mc-tDCS targeting and optimizations for a combined EEG/MEG source reconstructed dipole target in skull conductivity calibrated realistic head models for a group of 10 healthy subjects.

The second significant contribution to this thesis is a follow-up experimental study with 13 healthy subjects. In this study, for the first time the individually optimized tDCS montages produced by the novel D-CMI mc-tDCS approach is applied in an experimental paradigm targeting the Brodmann area 3b. Right-hand index finger stimulated SEFs recorded before and

after the D-CMI based tDCS are analysed and compared with standard bipolar tDCS montage and a D-CMI based sham tDCS condition for 13 subjects. A comparison of the 20 ms SEF signal component before and after the three tDCS conditions (D-CMI, SB and Sham) is conducted. These comparisons are conducted to answer the question of whether can the individually optimized, D-CMI based, mc-tDCS montages, targeting the Brodmann area 3b, reconstructed from a combined EEG/MEG skull conductivity calibrated source analysis, provide more controlled stimulation effects compared to the standard bipolar tDCS condition.

## 1.2 Organization of thesis

In **Chapter 2**, the fundamentals of the topics covered in this thesis are introduced. The chapter starts with a brief introduction and explanation of the human brain's anatomical parts, their functions and neuronal functioning. Further explanations about the history, basics and applications for tDCS are given. Next, an explanation of the human somatosensory system and its functioning is given, as this is the system that is target in simulations and experimental work. An explanation about the imaging modalities such as magnetic resonance imaging (MRI) and recording modalities, the EEG and MEG are given. In the last part of Chapter 2, a detailed theoretical background for EEG and MEG source analysis, solutions for the forward and inverse problems in EEG and MEG, and detailed explanations about the head tissues that are significantly influential for EEG and MEG source analysis.

In **Chapter 3**, a novel mc-tCS optimization approach, the D-CMI is introduced, analysed and compared to the state of the art intensity, focality and standard tDCS approaches. These tDCS methods are the intensity based approaches, the MI and CMI, the focality based tDCS approach, the ADMM, and standard bipolar tDCS approach. The chapter starts with introduction of a combined EEG/MEG source analysis pipeline with skull conductivity calibration while reconstructing the underlying P20/N20 somatosensory target at the Brodmann area 3b as a dipole, with individualized location and orientation for each subject (10 subjects in total). Next, an explanation of the theoretical and mathematical formulation, for tDCS in general and for mc-tDCS optimization methods with hardware constraints is described in detail. Furthermore the D-CMI, ADMM and MI are formulated and explained. In the results section the D-CMI is investigated in detail for a single subject and then a group of 10 subjects. Current vector fields and tDCS montages are simulated for the described tDCS methods and compared with the D-CMI approach with visual and statistical analysis. Finally, in the discussion section, the results are interpreted and discussed.

In **Chapter 4**, the validity of the D-CMI approach is tested and compared with standard bipolar and a D-CMI based Sham tDCS condition in finger stimulated somatosensory SEF/tDCS/SEF experiment. The combined EEG/MEG source analysis pipeline with skull conductivity calibration for the P20/N20 is again conducted for 13 different subjects and reconstructing individualized dipole targets. D-CMI montages are for each subject and a

group analysis is performed. The simulated D-CMI montages are applied in an experimental paradigm, SEF/tDCS/SEF, with standard bipolar and a sham condition resulting in three different sessions for each subject. Only MEG is recorded before and after tDCS condition and the 20 ms SEF signal component is compared with statistical analysis for the three conditions. Questionnaire data for skin sensations and sham perception is also taken and statistically analysed in the results section. Finally, in the discussion section the practicability of the D-CMI approach is discussed and the advantages it can have compared to standard tDCS methods.

In **Chapter 5**, as a co-authored study, tDCS induced electric fields and montages are simulated for 21 participants in finite element method (FEM) realistic head models. Standard brain atlas was used to define the tDCS dipole target's location at the parietal cortex with three orthogonal orientations as Target 1 (radial to the scalp surface, RAD), Target 2 (tangential to the scalp with anterior-posterior orientation, tangential<sub>a-p</sub> TAP) and Target 3 (tangential with a left-right orientation, tangential<sub>l-r</sub> TLR). Electric fields and montages from CMI and ADMM mc-tDCS methods are produced and compared with the non-individually optimized fixed 5x1 control mc-tDCS method in simulations. Variability in quantification parameters for the simulated electric fields along these three different orientations for the three methods (CMI, ADMM, 5x1) is statistically analysed and investigated in group study of 21 subjects.

**Chapter 6** provides a summary of the thesis while discussing the main findings and highlighting points for future research.

## 2 Basics and theory

### 2.1 The human brain

The human brain is one of the most biologically complex structures that controls all functions of the body, interprets and processes sensory information and relays motor responses to organs. It is divided into several functional and anatomical regions and is encased in several hard and soft layers of tissues. It is composed of billions of interconnected nerve cells or neurons and supporting glial cells or glia [17]. It is divided into external and internal parts that have specific roles. The three main external parts are the cerebrum, brain stem and cerebellum. The internal parts are made up of the pituitary gland, hypothalamus, and corpus callosum (Figure 2.1).

**Cerebrum:** The cerebrum is composed of grey matter and white matter layers. It is the largest part of the brain by volume. The cerebral cortex is the grey matter of the cerebrum. The cerebral cortex is mainly folded by surfaces called the gyri. The gyrus is separated by deep fissures called the sulci. The cerebral cortex consists of the right and left hemispheres, and each of them consists of four distinct lobes: the frontal lobe, parietal lobe, temporal lobe and occipital lobe (Figure 2.1(a)). The frontal lobe controls motor related tasks and activities associated with memory, attention, language, personality and other cognitive functions. The parietal lobe processes touch and pain related sensations and is also concerned with visuospatial navigation such as determining where the body is located within a space or how to avoid an obstacle. The temporal lobe fundamentally role is auditory processing and language comprehension. It also consists of components essential for long term memory retention by classifying memory into facts and events. The occipital lobe is the visual processing center of the brain with the capacity for sight, size, motion, color and dimension recognition.

**Brain stem:** The brain stem lies in the posterior region of the human brain. It connects the brain to the spinal cord from which signals are relayed to and from the body. There are three main parts to the brain stem, the pons, the medulla oblongata (often called medulla) and the midbrain (Figure 2.1). It is basically the control center for the respiratory, cardiovascular and other basic systems of human body. The brain stem is responsible for controlling involuntary and automatic functions such as heart rate, breathing, swallowing, hunger and thirst etc.

**Cerebellum:** The cerebellum lies in the posterior region of the brain below the temporal and occipital lobes behind the brainstem and is composed of a small portion of the cerebrum. The function of the cerebellum is to coordinate unconscious motor functions such as movement and balance. Damage to cerebellum could lead to muscle contractions and loss of equilibrium.

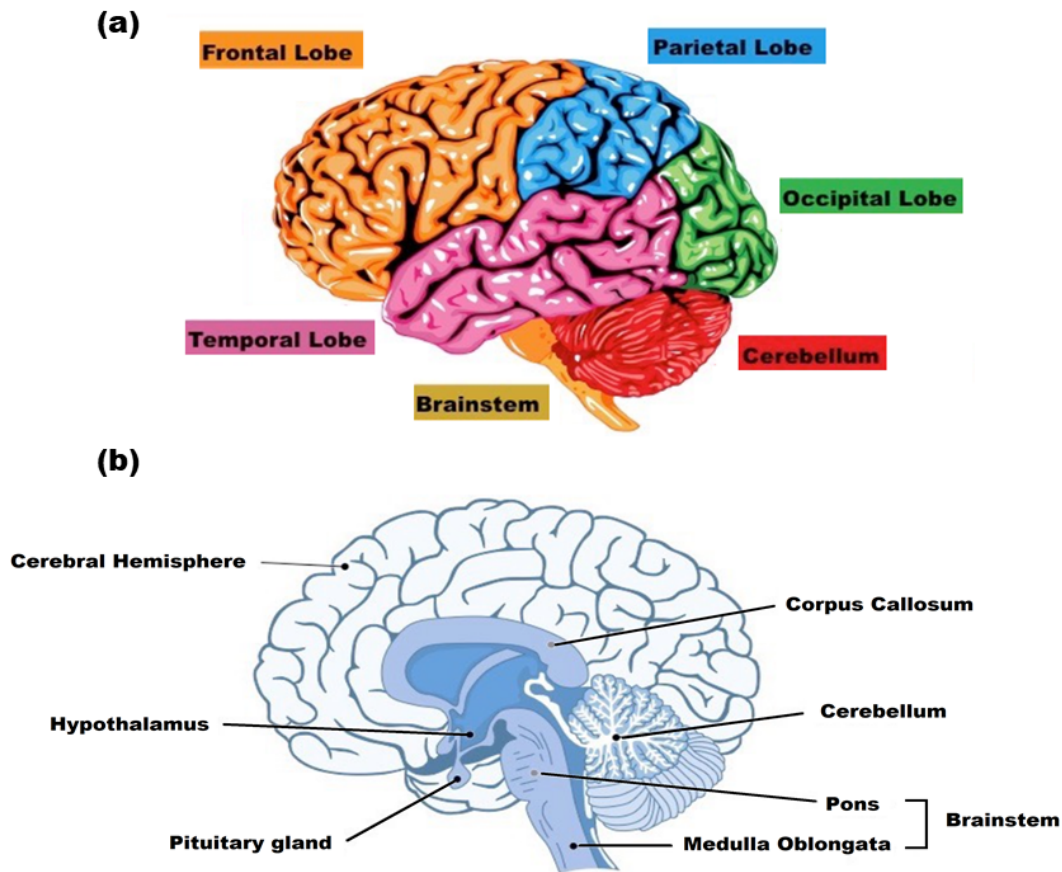


FIGURE 2.1: The basic structure of a human brain. (a) The human brain structure divided into different lobes (b) The internal structure of the human brain. (adapted from [bioninga.com](http://bioninga.com))

**Pituitary gland:** The pituitary gland acts as the master gland that regulates all other glands and target organs through hormonal production in the human body. It is mainly responsible for the flow of hormones from those organs of the human body that are associated with growth, physical maturation sexual maturation and functioning.

**Hypothalamus:** The hypothalamus is situated above the pituitary gland and functions as an interface to the pituitary gland. It acts as a command center for governing and coordinating neural and endocrine activity. It regulates and maintains homeostasis of the body by changing physiological parameters such as blood pressure and temperature of the body. It tries to optimally adapt to reestablish homeostasis by first comparing accessed sensory information to the biological options set for optimal cell function and then by enabling behavioral and endocrine responses. Through this process, it controls body temperature, synchronizes sleep patterns, controls hunger and thirst and also plays a role in some aspects of memory and emotion.

**Corpus callosum:** The corpus callosum lies in the middle of the brain filled with nerve fibers that connects the two left and right hemispheres of the cerebral cortex. It is the largest white matter structure of the brain and

enables the two sides of the brain to communicate. If the corpus callosum is damaged, it might lead to less communication between the two sides of the brain leading to brain disorders.

## 2.2 Neuronal basis

The neurons form the fundamental part of the central nervous system (CNS) and the brain and transmit electrical signals within the nervous system. Neurons are supported by other nerve cells called glial cells for energy and to feed the neurons. The nervous system together with the brain is able to detect, interpret and respond to external and internal stimuli by the functioning of neurons. There are different types of neurons that differ according to their role such as motor, relay and sensory, but most share the same features to permit their intercommunication. The basic parts of a neuron are the soma (cell body), the dendrites, the axons and the axon terminal (presynaptic terminal) (Figure 2.2(a)).

**Soma:** The soma is the neuronal cell body that has the nucleus and organelles, containing all genetic information. It functions as the metabolic center by synthesizing cell proteins to maintain cell survival. Additionally, it enables two processes the dendrites and the axons. **Dendrites:** The dendrites are tree-shaped short branched fibers that handle incoming signals from other nerve cells and act as receptors. Initially, these incoming signals are chemical information signals which are then converted to electrical signals.

**Axons:** The axon is a long and thin extension fiber of the neuron cell body originating from the area called the axon hillock. The axon acts as a transmission line that transfers electrical signals called action potentials. These action potential signals are originated in a trigger region near the axon hillock called the initial segment and they travel down the axon with high speed and without loss of information. The axon, in some neurons, is covered with an insulating layer called the myelin sheath. The myelin sheath increases the conduction speed of the action potentials along the axon by means of specifically shaped sheaths at regular intervals called nodes of Ranvier.

**Axon terminal:** The axon terminal lies at the end of the axon which transmits an electro-chemical signal to another neuron or cell type. It contains synapses that are specialized button-shaped structures where neurotransmitter chemicals are released into a gap called the synaptic cleft between the terminals and the dendrites of the next target neuron to communicate.

**Action Potentials:** In the brain, neural signal processing is conducted through the inter-neural-exchange of electrical neural signals called action potentials (AP) (Figure 2.2(c)). An AP is generated when a potential difference is created between intracellular and extracellular space, which are separated by a cellular membrane (Figure 2.2(b)). An AP requires an influx of positive ions across the semi-permeable neural membrane to produce a specific change in voltage (threshold value). During the resting period, the potential difference across the membrane is  $-70\text{mV}$  or  $-90\text{mV}$  and is called

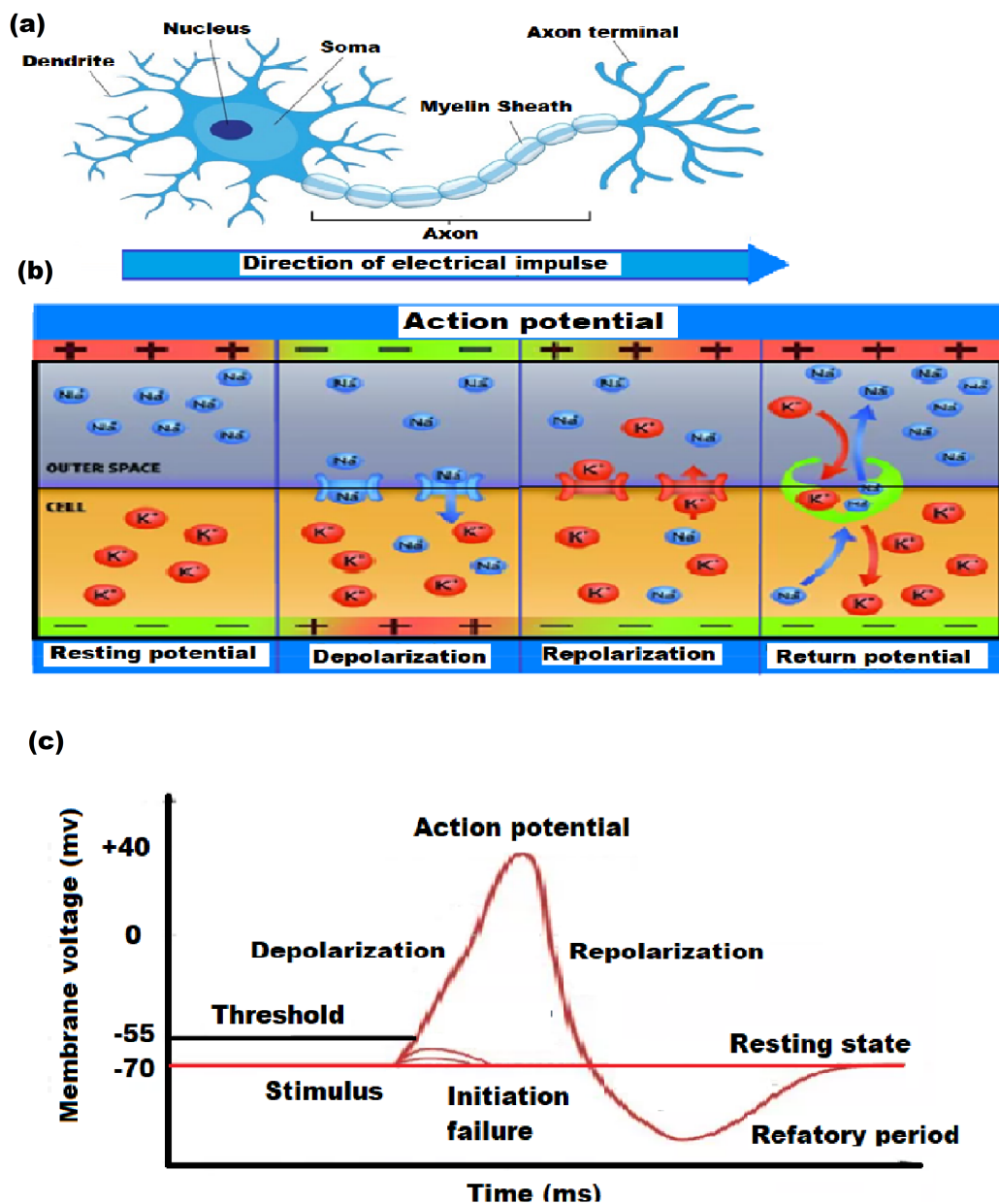


FIGURE 2.2: Neuronal anatomy and mechanism (a) Illustration of the basic anatomy of a neuron (b) Basic mechanisms of the flow of ions and ion channels during an action potential in a neuron (c) Basic shape of the process of an action potential.(adapted from bioninga.com)

“resting membrane potential”. AP occurs in a sequence of three stages, depolarization, repolarization and refractory period.

**Depolarization:** Depolarization takes place when the signal is initiated at a dendrite, in response to an outside stimulus, and sodium channels open within the membrane of the axon. As more  $\text{Na}^+$  ions are concentrated outside of the membrane, the opening of the sodium channels leads to an influx of positively charged sodium channels which causes the inner side of the

membrane to become more positive (Figure 2.1(b) and (c)). When a threshold potential of  $-55\text{mV}$  across the membrane is reached an AP is initiated.

**Repolarization:** For the propagation of an AP along the axon, the inward flow of the positively charged sodium channels also later causes the potassium channels to open within the membrane of the axon (Figure 2.2(b)). As the positively charged  $\text{K}^+$  potassium ions were more concentrated inside the membrane it causes the outward flow of these ions. The outward flow of  $\text{K}^+$  causes the membrane potential to start returning to a more negative potential difference. This is known as repolarization (Figure 2.2(b) and (c)). Following repolarization, the positively charged ions continue to exit the membrane as the ion channels take time to respond. During this lack of immediate response, the potential inside the membrane continues to become negatively charged until it reaches a threshold value between  $-71\text{mV}$  and  $-75\text{mV}$  known as hyperpolarization. During hyperpolarization, the voltage-gated channels close and a resting potential of  $-70\text{mV}$  is reached again through the sodium-potassium pump (refractory period) (Figure 2.2(b) and (c)). In general, polarization refers to an increase or decrease in membrane potential compared to its resting state potential.

In this thesis, we will examine (simulation and practical stimulation) the effects of electric fields on the brain in simulations (Chapter 3 and 5) and a practical study (Chapter 4). In order to understand the underlying mechanisms of these effects produced from the externally applied electric fields, a theoretical basis of the neuron and its mechanisms is explained. As explained before, when a neuron is exposed to an external stimulus, in this case, an external electric field, it can lead to polarization. However, polarization, and the subsequent characteristics of generation and propagation of APs, depend on neuronal morphology, biophysical parameters, orientation with respect to the electric field and the electric field strength. We can stimulate the brain non-invasively by a technique known as transcranial direct stimulation which is a sub-category of the general approach of transcranial electrical stimulation.

## 2.3 History of transcranial electrical stimulation (tES)

The use of electricity as a medical treatment has been reported to be used since the Roman and Greek times. Around 43–48 CE Roman physician, Scribonius Largus, used torpedo fish to treat headaches with electrical pulses [18]. Along with being reported as the first use of electricity as a medical treatment, it is also the first known study for electrical brain stimulation. Although these early studies were reported, prior to the 17th century, little was understood about the effect of electricity on a body.

In the 18th century, the basis for modern-day electrophysiology has been credited to Luigi Galvani. Galvani, through his work on the effects of electricity on dead bodies, revolutionized the understanding and scientific thinking about the relationship between electricity and animal bodies. Galvani demonstrated [19] that dead bodies (mostly frogs) could be made to move using electricity. He was also the first person to show the electrical nature

of muscle contraction and nerve conduction [19]. Galvani's nephew, Giovanni Aldini, further researched about muscle contraction by experimenting on executed prisoners [19]. Aldini applied electrical currents on the head of executed prisoners to show muscle contraction. As Aldini believed electricity can be used as a useful medical tool, he also started using it to treat patients with mental disorders (Figure 2.3). There is also a documented case of Aldini treating a patient with melancholia (depression) [20].



FIGURE 2.3: The above illustration shows the application of galvanism to patients with mental disorders. The illustration is a reproduction of plate 5 from Luigi Aldini's 1804 essay. Effects of galvanism were optimized by connecting a voltaic pile to the head and hands. Other locations such as left and right panels were also considered [20].

In the 20th century, direct currents were used as stimulating or sedative treatment by several researchers. Their success in treating patients with depression was reported but variability still persisted in the results. In the 1940s and onwards, as electroconvulsive therapy (ECT, electricity-induced seizures) became highly successful and popular, interest in brain polarization diminished [21].

In the 1960s, effects of current stimulation on the brain and its inner workings first came to light by a series of electrophysiological measurements in animals. The effects of polarizing currents on neuronal cells were investigated by applying subthreshold currents directly to the cortex and measuring from within the cortex. Electrode with positive polarity (anode) on the cortex in anesthetized cats [22], [23] and rats [24] led to an increase in the frequency of spontaneous neuronal discharges and in the size of the sensory evoked potentials (Figure 2.4). Conversely, a negative polarity electrode (cathode) resulted in decreased neuronal firing. These results demonstrated that the application of subthreshold currents could modulate the activity of pyramidal neurons. Interestingly, opposite effects were observed from the polarity-dependent currents on deeper lying neurons [22] and non-pyramidal tract neurons [23] in the motor cortex (M1). These important findings suggested that the orientation of a neuron and its type influenced the directional response of a cell to polarization by an external source. A comparison of neuronal cell types revealed that pyramidal tract neurons were activated at higher stimulation intensities compared to non-pyramidal neurons, such as inter-neurons. In the following years between 1964 and 1980, a

series of current-controlled stimulation experiments were conducted on patients with psychiatric conditions such as depression and schizophrenia. The experimental trials, however also included healthy subjects [25]. Treatment of depression was still the most common application, with several clinicians reporting improvements in mood during and after stimulation [26]–[28]. In these studies, however, the stimulation parameters were as varied as the patients they were applied and typically were not consistent with those used in modern transcranial direct current stimulation (tDCS) applications. In animal studies, monkeys showed improved task performance for a reaction time task [29] and rats showed improvement for learning avoidance responses [30], [31] after direct stimulation of the dorsolateral prefrontal cortex (DLPC).

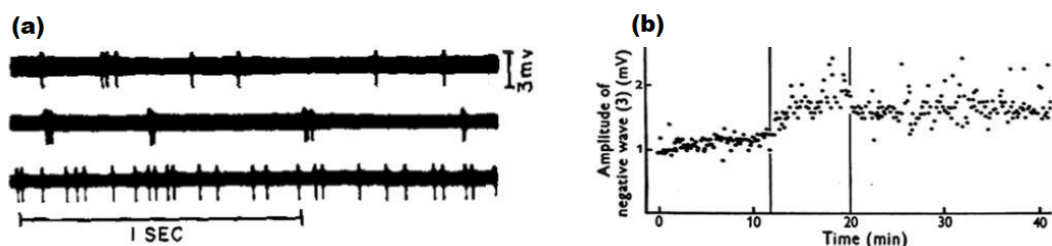


FIGURE 2.4: The above two Figures show the intracortical recording of anesthetized animals experiencing brain polarization (adaptation from [22] and [24]). (a) Neural activity (first-panel activity) decreased after negative applied current (second-panel activity) and increased (third-panel activity) after positive applied current to the cortex. (b) Peak values of Somatosensory evoked potentials increased after a positive current was applied to the cortex.

Investigations by Priori and colleagues [32] renewed interest in tDCS applications after nearly 35 years. In their study, the stimulation electrodes were placed over M1 and the chin. Weak direct currents (DC) ( $< 0.5$  mA) were passed through the cortex for seven seconds. In the stimulation paradigm, no effects were observed when only anodal or cathodal stimulation was conducted. However, anodal scalp DC, alternated with a cathodal DC (alternating anodal-cathodal stimulation) led to an increase in neuronal excitability. These observations provided evidence that a small electric field crosses the skull and influences the brain. Lack of effects from only anodal and cathodal DC stimulation was hypothesized as the result of sub-optimal electrode placement and a combination of short stimulation time periods [33]. In 2000, applying similar techniques, Michael Nitsche and Walter Paulus published their findings on tDCS-elicited excitability changes with a series of experiments that established much of the modern and standard approach to tDCS application [1].

## 2.4 Transcranial direct current stimulation (tDCS)

### 2.4.1 Stimulation parameters

The stimulation parameters for tDCS can be categorized into temporal and spatial parameters that affect the distribution of the applied electric field on the scalp and the brain [34]. Spatial parameters comprise of shape, size and positioning (montage) of the electrodes. The temporal parameters consist of the waveform, current intensity (i.e., current amplitude in mA), polarity (positive or negative current) and duration (in minutes) of the applied electric current for stimulation. The combination of all these parameters determines the “dose” of the stimulation and is therefore crucial for determining the outcome of the stimulation.

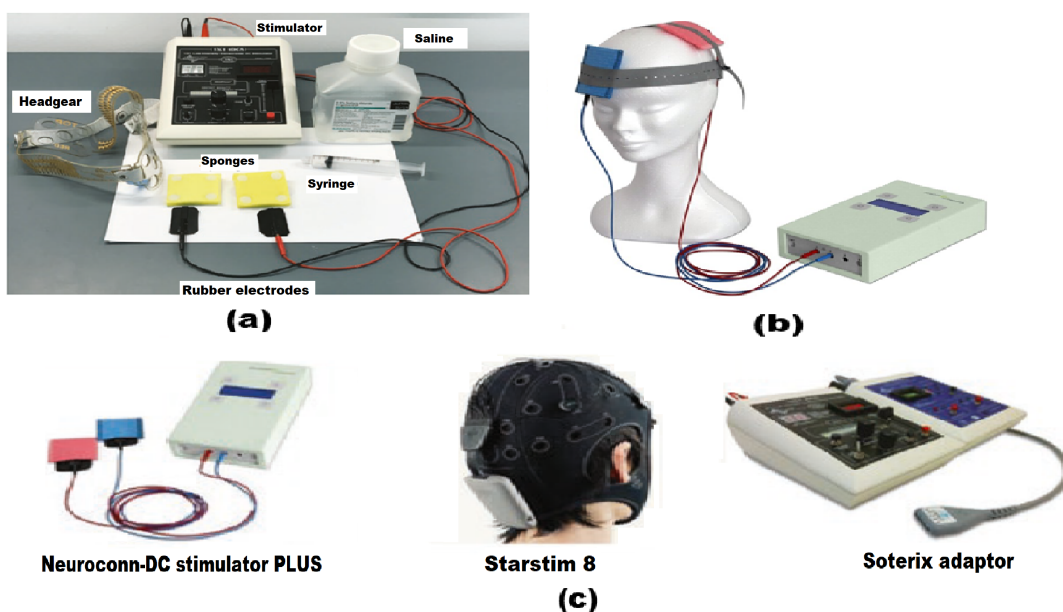


FIGURE 2.5: Different types of devices for applying transcranial electrical stimulation (tES). (a) The basic equipment needed to apply tES (b) Basic montage of applying tES (c) Commercially available tES devices (adapted from [35]).

**Size and shape of electrodes:** Typically, tDCS involves two sponges soaked with saline, electrodes made of conductive rubber, non-conductive elastic straps, cables, and a battery-powered device for delivering a current stimulation [36]. The pair of saline-soaked sponges are usually 20 to 35 cm<sup>2</sup> in size, with slits at both ends into which electrodes are inserted (Figure 2.5(a) and (b)). By designing the sponges in a way that promotes an even distribution of current over the stimulation area (2.5(b)), it has been possible to reduce the likelihood of skin burns caused by hotspots (electricity concentrations) at the sponge/skin interface [37], [38]. According to studies in the motor cortex, a reduction in the size of the active electrode can produce more robust and focused effects, while increasing the size of the return electrode can prevent any undesired effects for the non-target electrode [39].

**Polarity and duration:** In tDCS, where current travels in one way, stimulation is applied to two electrodes with different polarities. For a unidirectional stimulus, the current flows from the anode (positive electrode) to the cathode (negative electrode). When the anode, the positive electrode, is placed over the target area, we speak of anodal stimulation otherwise we speak of cathodal stimulation. Research on tDCS in the motor cortex suggests a stimulation duration of a minimum of approximately 10 minutes is necessary in order to produce effects lasting for up to an hour after stimulation [1], [40]–[42]. A general belief is that anodal tDCS stimulates and cathodal tDCS inhibits the underlying cortex, however, the reverse has been observed as well [43], [44]. It was found by Monte-Silva [45] that anodal tDCS applied for 26 minutes produced an opposite, inhibitory effect, indicating that duration plays a significant role in stimulation outcomes. It has also been reported that anodal tDCS, in general, results in more consistent effects than cathodal tDCS and is used more often [46].

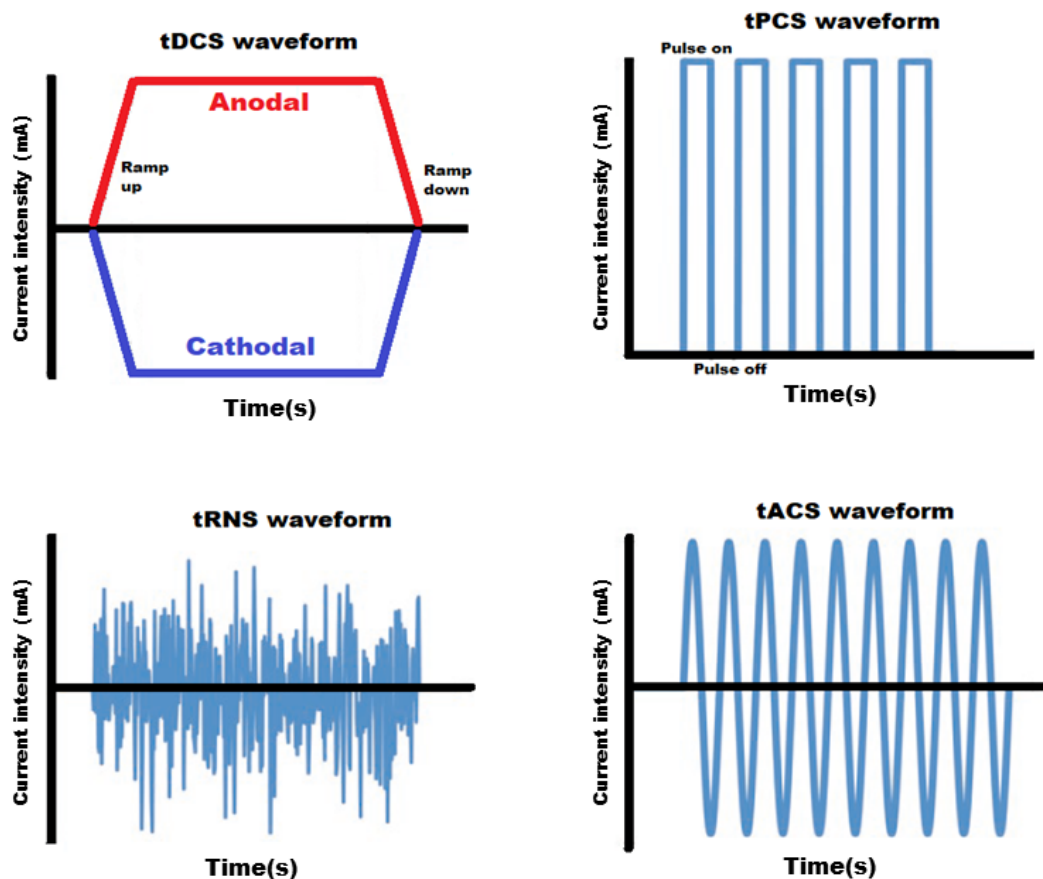


FIGURE 2.6: Different waveforms for tES produced by commercially available hardware (adapted from [35])

**Waveforms:** In the past few decades, other types of tES have been developed, e.g. tACS and tRNS. tACS uses a similar set of procedures and parameters as tDCS, except that the current applied changes over time. There is typically a sinusoidally oscillating current applied either in combination

with a DC offset [47], [48], or applied every half cycle [49], [50]. In case of tRNS, a combination of different frequencies was used by researchers producing randomly oscillating currents [51], [52]. In addition to affecting excitability and brain function [48], [49], [51], [52], these modes of stimulation can influence intrinsic brain oscillations as well [47], [50]. The devices that are commercially available (such as neuroConn, Soterix, and Starstim) (Figure 2.5(c)) already have pre-programmed waveforms and parameters (such as tDCS, tRNS, and tACS). The customisable waveform and current generators are capable of producing an endless variety of customised waveforms. However, the effects of such stimulation remain unknown. In Figure 2.6 the different tES waveforms are shown that can be produced by commercially available hardware.

### 2.4.2 Neurophysiological mechanisms for tDCS

In the case of using sponge electrodes on the scalp, the applied current will shunt at the scalp and as well as in the cerebrospinal fluid (CSF). This will result in some current penetrating the superficial layer of the brain [53]. Despite the low intensity of the resulting electric fields, the continuous electric fields generated during tDCS have the ability to alter transmembrane neuronal potentials, modulate nerve excitability and the synaptic responses [54], and even modulate individual neuronal firing rates [53], [55]. The effects of tDCS on neuroplasticity may be related to modulations in neuronal ionic channels, specifically L-type voltage-gated calcium channel (LVGCC), and N-methyl-D-aspartate (NMDA) receptors [2]. As tDCS injects only a small amount of current, it is a subthreshold stimulation i.e. it does not produce any action potentials but rather facilitates or modulates neuronal activity in a polarity (positive or negative) dependent manner.

Anodal stimulation (positive current) will result in the inward flow of the current and cathodal stimulation (negative current) will produce an outward flowing current (Figure 2.7a). This phenomenon is most likely due to the somatic depolarization of pyramidal cortical neurons and hyperpolarization of apical dendrites in the case of anodal stimulation and somatic hyperpolarization (Figure 2.7b) of pyramidal cortical neurons and depolarization of apical dendrites when cathodal stimulation is applied [57], [58]. Even moderate intensities of stimulation current and duration change brain activity, which is assumed to follow somatic polarization [1], [59]. While using conventional tDCS (anode and cathode) over a target region, the current is not only limited to the target area but it also flows through all cortical regions between and around the anode and cathode electrodes [60]. It is therefore very important for the placement of the tDCS electrodes to target specific regions of interest.

### 2.4.3 Measurement of tDCS effects

There are a number of methods to investigate the neuronal effects generated by tDCS. These methods are physiological measurements that allow researchers to quantitatively measure the basic effects of tDCS so they can

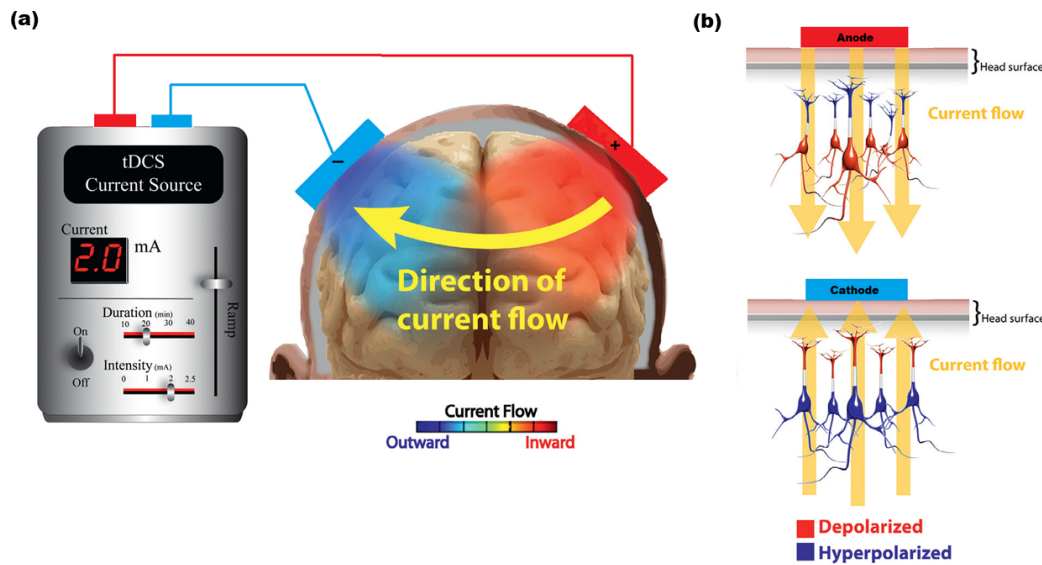


FIGURE 2.7: Direction of current flow and effects on neurons (a) Direction of current flow in anodal stimulation (b) Current flow direction effects on neurons for depolarization and hyperpolarization. The Figures were modified from [56]

better understand its mechanisms and design new protocols for different applications.

There are now several different types of neurophysiological and functional imaging technologies available today that allow researchers to study how tDCS affects our brains. To monitor the effect of tDCS applied to a particular brain region, the most used methods are monitoring of tDCS effects over sensory (e.g. somatosensory evoked potentials (SEP) and fields (SEF)) and motor cortices (e.g. Motor evoked potentials), event-related potentials (ERP), electroencephalography (EEG), a combination of transcranial magnetic stimulation (TMS) and electromyography (EMG) TMS/EMG, and neuroimaging tools such as magnetic resonance imaging (MRI), and positron emission tomography (PET). Also, a number of pharmacological agents have been used to determine the neurochemical basis of tDCS. These pharmacological interventions can be used to study how tDCS affects specific neurotransmitter systems, ion channel function, or receptors. As it is beyond the scope of this thesis to discuss all of these methods, we will briefly discuss the methods used for motor and sensory cortices.

Historically, the majority of tDCS studies performed have been for the primary motor cortex (M1) via TMS/EMG. Anthony Barker and colleagues [61] developed an electronic device that sends out a powerful, short electrical impulse through a 10 cm coil. The changing current in the coil generates a rapidly fluctuating magnetic field which causes an induced electrical field. By placing the coil tangentially to the scalp, the magnetic field penetrated through the scalp and skull inducing electric fields in the brain. The fields induced in the brain are directed parallel and opposite to the currents in the coil. This induced field can depolarize neurons and evoke action potentials.

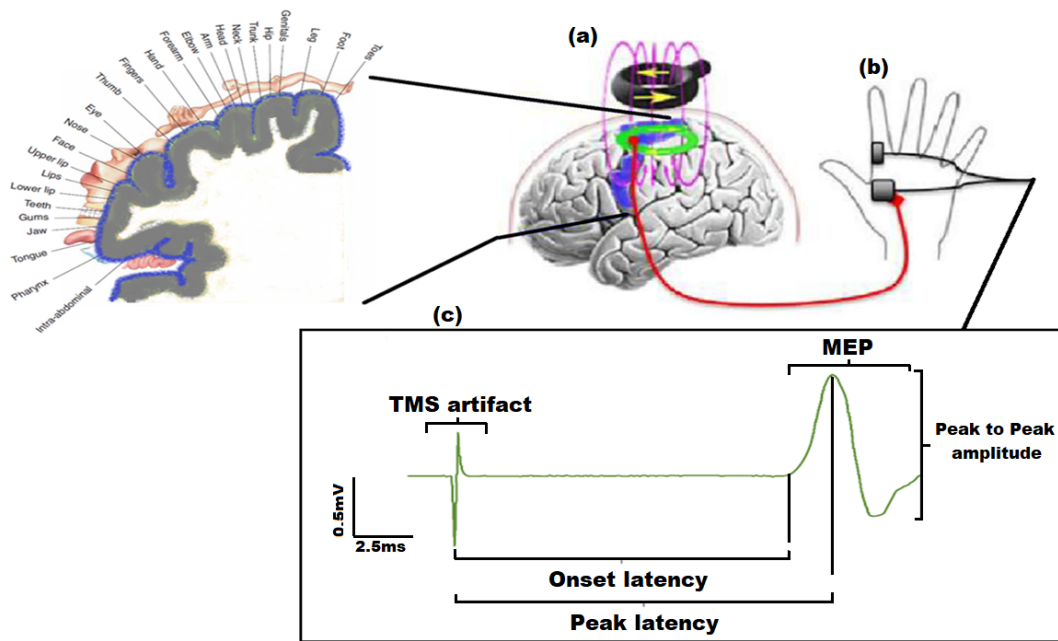


FIGURE 2.8: The measurement of MEPs with TMS and EMG. (a) shows the placement of the TMS coil on the cortex which induces a magnetic field (pink lines) and created electric fields (green) in the cortex. (b) The placement of EMG electrodes for recording MEPs at the first dorsal interosseous (FDI) muscle (c) The recorded MEP from the EMG electrodes.

The concept of transcranially inducing electric fields in the brain which produce action potentials from magnetic fields of a coil came to be known as TMS. When a TMS pulse is applied over the M1, the activated cortical neurons in close proximity generate a signal which travels through the corticospinal tract and activates a certain number of spinal motoneurons, which further convey the signal to the alpha motoneurons of the associated muscle. This muscle activity, contralateral to the stimulated M1, can be observed as a muscle twitch and can be recorded on the skin using EMG. The motor evoked potential (MEP), measured via electrodes on the skin over the muscle (Figure 2.8), provides a measure of the excitability of the cortical neurons that project to the muscle. [62] were the first to employ TMS to quantitatively study the effects of tDCS on M1. They were also the first to use two large electrodes for tDCS, one over the M1 and the other over the chin. In the study, anodal tDCS (positive current over M1) a consistent decrease in MEP size (evoked by TMS over M1) was seen compared to before tDCS anodal stimulation. The depression in MEP size was proportional to the stimulation current. Nitsche Paulus [1], [41] further expanded Priori's research and conducted experiments for the M1 using TMS/EMG and tDCS. Their tDCS montage consisted of one electrode over M1 and the other over the contralateral supraorbital area (SOA). In their experiments, anodal stimulation increased and cathodal stimulation decreased cortical excitability. These findings later became the basis for future tDCS studies. For the application of

tDCS to the sensory cortex, most studies were conducted on the somatosensory cortex. The effect of tDCS on the neurophysiological function of the somatosensory cortex can be studied by analyzing the changes in SEPs and SEFs, measured by EEG and MEG modalities respectively, changes in the brain's hemodynamic response, or at the behavioral level by effects on measures of somatosensory perception. [63]–[69]. SEP and SEF evaluations often include low-frequency components, such as N20, P20, P22, N30, P35, or P60 [63], [64], [70], [71] neuroanatomical studies suggest that generator sources for these components are located cortically, including area 1,2 (component P60) or 3b (N20) of the primary sensory cortex (S1) or in the motor cortex (e.g. component P35). Further details can be studied about these components and their applications in [72].

#### 2.4.4 Safety of tDCS

As far as safety is concerned, researchers and clinicians have generally agreed that tDCS is not associated with serious adverse events. This is further evidenced by the routine testing of tDCS on healthy volunteers (e.g. up to 6 weeks in college students;[73]). It is common for subjects to experience tingling, itching or burning sensations in the skin underneath the electrodes during tDCS. These sensations usually subside after a few minutes of tDCS but can be slightly painful. Only in [46], skin burns were reported due to incorrect application of tDCS resulting in extremely high impedance. Usually, with the correct application of tDCS, this occurrence is rare. As a precaution, all commercially available stimulation devices terminate stimulation when impedance reaches a certain high level. However, adverse side effects like mild headache or fatigue and rare cases of transient nausea and vertigo have been reported [46]. The sensations under the tDCS electrodes can be reduced by enlarging the electrode size resulting in lower current density in the skin. The sensations are felt strongest and even quite painful when the current is switched from 0 to 1 mA or 2 mA immediately. This sudden transition can also result in phosphenes (perceiving a flash of light due to excitation of the retina by sources other than light). In order to avoid these effects, it is common in most tDCS applications to ramp the current up and down linearly over a few seconds at the start and end of stimulation, respectively.

#### 2.4.5 Sham stimulation

As in any drug or other interventional protocols applied in clinical neuroscientific research, a form of placebo (fake) treatment is required for systematic studies of the effects through randomized controlled trials. Placebo interventions for tDCS are known as sham stimulation. The subjects are usually questioned after the stimulation about their own rating if sham or real tDCS has been applied. As the subjects feel sensations on the skin during tDCS, sham stimulation is based on mimicking these sensations. The feelings are strongest at the start of stimulation, so blinding can be realized by

encompassing ramping stimulation up and down like in real tDCS stimulation conditions, but stimulate with an intensity of e.g. 1 or 2 mA only for a few seconds. In this way, participants will feel the initial itching and tingling sensation but the stimulation duration is too short to induce after effects. A stimulation intensity of 1 mA and an electrode size of 25 cm<sup>2</sup> has been shown to reliably blind participants [74]. Stimulation intensities of 2 mA tend to make comfort lower at stimulation onset for young and older adults [75]. Higher stimulation intensities will induce stronger sensations, and thus compromise blinding, especially under repeated measures conditions [76], [77]. Stimulation intensities as high as 3 mA starts to become painful while smaller electrodes do not increase skin sensations [78]. An alternative approach would be the use of anesthetics to abolish skin sensations [79] or an active control condition (i.e. stimulation of brain region irrelevant to the experimental paradigm).

### 2.4.6 Clinical applications of tDCS

In addition to the effects of tDCS on neuromodulation, such as learning rate [80]–[82] and measuring excitability, tDCS has been tested as a treatment for several neuropsychiatric disorders and neuro-rehabilitation [83]. Firstly, since many psychiatric and neurological diseases pathologically alter plasticity and excitability, tDCS is most often used to re-balance the underlying system e.g. in epilepsy, pain and depression. A second argument for using tDCS is the relevance of plasticity and cortical excitability alteration, for learning and memory formation, and therefore the potential of tDCS in rehabilitation e.g. motor rehabilitation, visual restoration, dystonia [84] and Alzheimer's disease. Considering how complex the (individual) etiology of disease and the brain response is, testing tDCS's capability to affect excitability and plasticity is a good place to start in rationalizing clinical trials [85], [86].

For instance, tDCS has been used for behavioral performance enhancement with Alzheimer's patients [87], [88], for motor learning enhancement in stroke rehabilitation [89], for patients with chronic pain [90]–[94] and for modulation of emotional affective neural circuits in depression patients [87], [95], [96]. For tDCS pain therapy application, tDCS has been applied to cases of chronic pain refractory to pharmacologic interventions [97], [98] and for a number of different pain conditions such as fibromyalgia, pelvic pain, and neuropathic pain [91], [99], [100]. Numerous studies have also examined the effects of tDCS on learning in healthy subjects, suggesting improvement in implicit learning [101], motor memory [102], working memory [103], [104], and memory retrieval [105], [106].

## 2.5 The human somatosensory system

In this thesis, we will be investigating the effects of tDCS on the somatosensory network specifically the primary somatosensory cortex (S1). In order to

assess the effects that tDCS can produce on the somatosensory network, a basic understanding of the anatomy and physiology of the human somatosensory system is needed. The human somatosensory network is a thoroughly

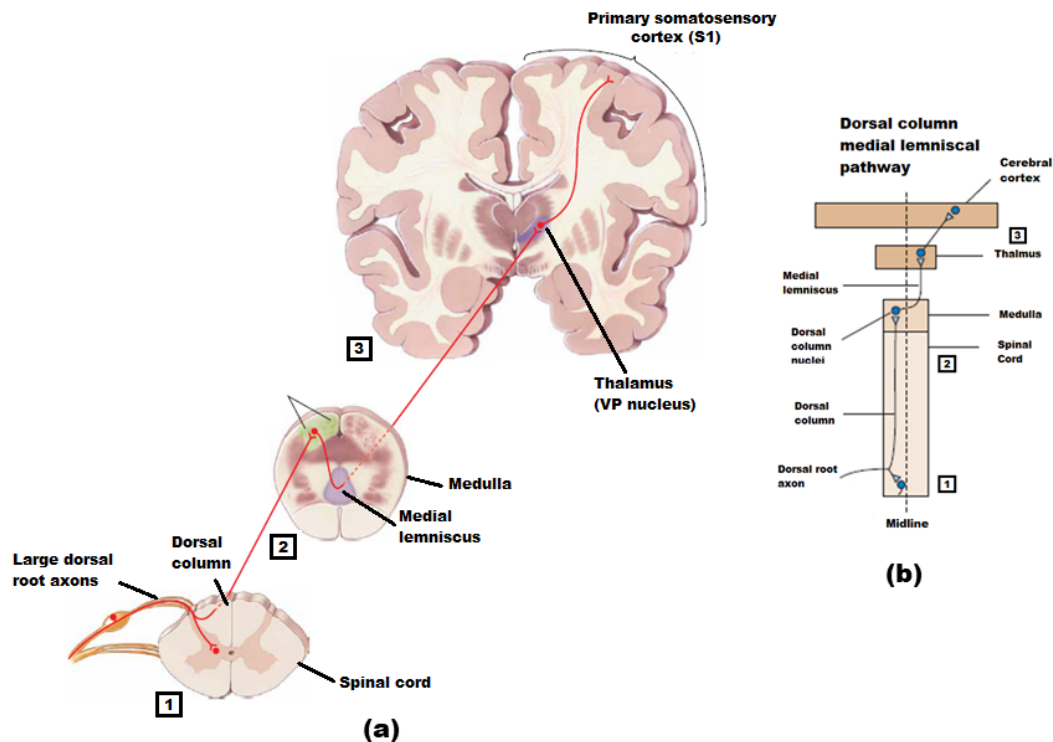


FIGURE 2.9: The signaling pathway for the human somatosensory system. (a) shows the dorsal column-lemniscal pathway (red) from the receptors (step 1) to the primary somatosensory cortex (S1) (step 3) via different fibers in steps 1, 2 and 3. (b) shows a complementary block diagram for the dorsal column-lemniscal pathway. The Figures were adapted from [107]

investigated system of pathways associated with the cerebrum stimulated by sensations such as touch, pressure, vibration, heat, cold, itch and electrical current [17]. These sensations are conveyed by the receptors on the skin, muscles or joints conveyed to different regions of the brain for processing. However, the information of touch, vibration or electrical stimulation from the skin (Fingers or arm) takes an entirely distinct path compared to pain or temperature. The structural pathways of these sensations are divided into two parallel subsystems the dorsal column-medial lemniscal pathway (mechanoreception and proprioception) and the spinothalamic pathway (thermoreception, nociception and visceroreception). A brief explanation of the dorsal column-medial lemniscal pathway is more relevant for this thesis as it is the underlying pathway undertaken by the sensations from the finger when stimulated with an electrical current. The endings for the dorsal column-lemniscal pathway are corpuscular nerves at the skin, joint capsule, and muscle. The dorsal column-medial lemniscal pathway as shown in Figure 2.9 can be explained by the following steps

- The large sensory axon enters the ipsilateral dorsal column of the spinal cord, the white matter tract medial to the dorsal horn. Sensory information (as well as positional information) is sent from the dorsal columns to the brain.
- At the junction between the spinal cord and the medulla lies the dorsal column nuclei, where the dorsal column axons terminate. These are some of the longest axons in the human body originating from the skin. It is a fast pathway bringing information directly from the skin to the brain without any interference from other synapses.
- The axons of the dorsal column nuclei then travel from the white matter tract known as the medial lemniscus. Axons from the medial lemniscus synapse upon neurons in the ventral posterior (VP) nucleus of the thalamus through the medulla, pons, and midbrain. It is important to note all sensory information goes through the thalamus before synapsing in the neocortex with exception of olfaction.
- Finally the information from thalamic neurons of the VP nucleus projects the specific regions of the primary somatosensory cortex or S1.

The cerebral cortex is the site of the most complex somatosensory processing. The cortical areas responsible for the somatic sensory system are located in the parietal lobe (Figure 2.10(a)). In humans, Brodmann's area 3b, now designated the primary somatosensory cortex (S1), can be easily identified because it lies behind the central sulcus (right behind the central sulcus) (Figure 2.10(a)). The Brodmann area 3b is called the primary region of the somatic sensory cortex because (1) it receives most of the information related to touch from the VP nucleus of the thalamus (2) the neurons in this region are very responsive to somatosensory stimuli (3) damage to this region can cause somatic sensation impairment and (4), most relevant to this thesis work, electrical stimulation evokes somatic sensory components. In addition to S1, other cortical areas process somatic sensory information. These cortical areas include areas 3a, 1 and 2 on the postcentral gyrus, areas 5 and 7 on the adjacent posterior parietal cortex (Figure 2.10(a)). Areas 3a also receive dense informational inputs but is rather related to position than touch. Areas 1 and 2 receive dense information from area 3b which are mainly of texture information for area 1 and size and shape for area 2. The somatic sensory cortex is a layered structure where the information from the thalamus synapse is mainly in layer IV of S1 (Figure 2.5(b)). Similarly, neurons in layer IV project to cells in other layers. S1 neurons with similar inputs and responses are stacked vertically into columns across the cortical layers, another important similarity with other regions of the cortex (Figure 2.5(b)).

## 2.6 Somatosensory evoked responses

Electrical stimulation of the median nerve or the fingers generates an action potential that takes the path of the dorsal column lemniscal pathway compared to the spinothalamic pathway due to its lower threshold for electrical

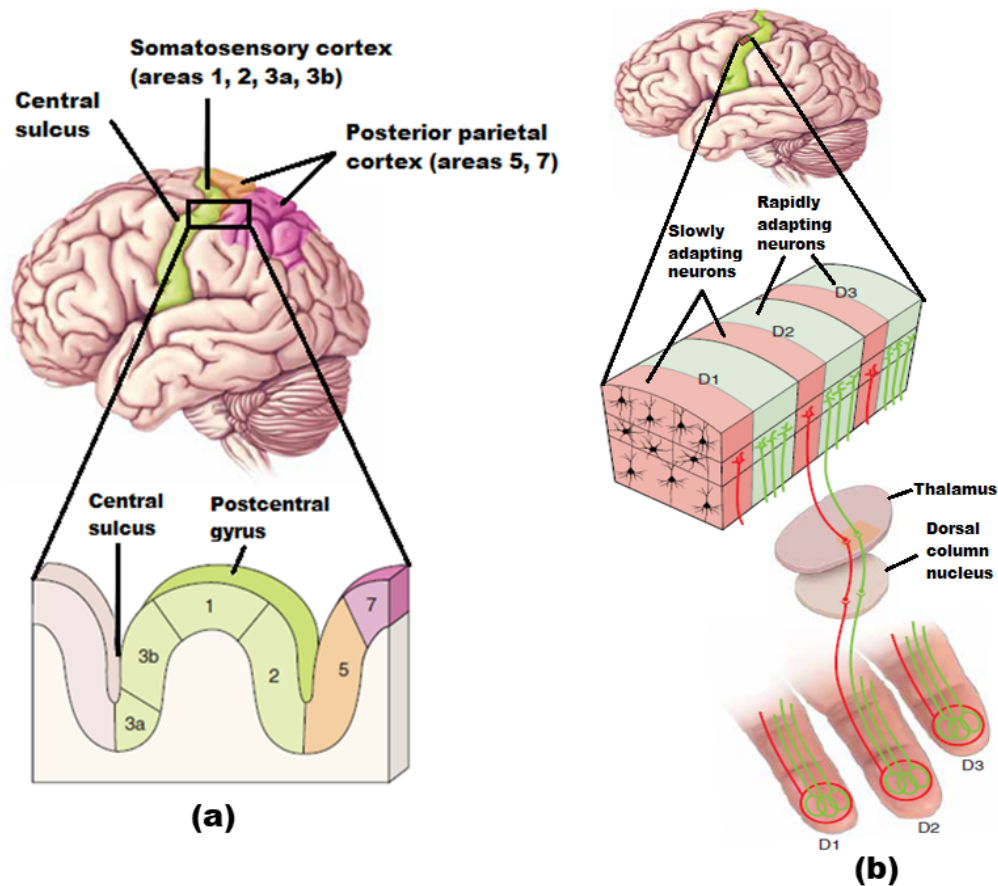


FIGURE 2.10: Somatic sensory areas of the cortex. (a) The illustrated areas lie in the parietal lobe. The lower Figure shows that the postcentral gyrus contains S1, area 3b. (b) Columnar organization of S1's area 3b. Each finger (D1–D3) is represented by an adjacent area of the cortex. Within the area of each finger, representation are alternating columns of cells with rapidly adapting (green) and slowly adapting (red) sensory responses. The Figures were adapted from [Bear2015].]

stimulation. The AP signal reaches the S1 area of the cortex by traversing the path from the dorsal column lemniscal and the VP nucleus. Non-invasive brain activity recording modalities such as EEG and MEG can record the signals generated in somatosensory area S1 which are termed as SEPs or SEFs respectively. Historically speaking, Dawson was the first to record human SEPs non-invasively by electrically stimulating the ulnar nerve at the wrist with 1Hz [108]. The first signal or component recorded at 14 ms after the stimulus onset represents the activity from the thalamus. The SEPs peaking at about 20 to 30ms (and later) representing S1 activity, since then, have been extensively used as clinical and experimental tools to study and interpret somatosensory pathways and early cortical processing [72]. More relevant for this thesis work, the early responsive component at 20ms, known as P20/N20 for SEPs, generally occurs as P20 (Positive polar component) posterior to the central sulcus and as N20 (Negative polar component) anterior to the central sulcus. It is now well established the generators for P20/N20 S1 component

can be modeled as a tangentially oriented dipole according to the sensory homunculus [109], [110]. Strong support for tangential area 3b source in S1 was also condoned when a comparison of 20 to 30 ms MEG and EEG responses showed dipolar patterns rotated by 90 degrees with respect to each other, as expected for MEG and EEG signals generated by the same tangential sources [111]. It is very advantageous to have prior knowledge of the location of the P20/N20 component at Brodmann area 3b when targeting with tDCS and modeling with source analysis. As it is very resilient to external factors, exogenous in nature and consistently reproducible. These reasons make it an ideal S1 component for MEG and EEG source reconstruction investigations and tDCS montage optimizations.

## 2.7 Measurement modalities

### 2.7.1 Overview

In this thesis, we will use three measurement modalities MRI, MEG and EEG. The combination of these modalities is used for source reconstruction of a particular brain region by solving the forward (realistic head modeling) and inverse problems, tDCS forward modeling simulations and analysing the effects of tDCS on the somatosensory network in an experimental paradigm. Here, in this section, we will briefly explain the underlying workings of these modalities and the parameters used for these modalities in this thesis.

### 2.7.2 MRI (magnetic resonance imaging)

As previously mentioned, we use MRI for realistic head modeling (solving the forward problem) to conduct source analysis. Realistic head modeling requires geometries of different tissue compartments inside the head as well as the brain conductivity anisotropy which is fulfilled by MRI. In this section, we will briefly explain the principles of MRI which will give a basic understanding of the imaging modality.

MRI uses the phenomenon of nuclear magnetic resonance imaging to construct images inside the human body [112]. According to Nuclear magnetic resonance (NMR) theory, certain materials inside a magnetic field causes it to either emit or absorb signals at specific frequencies. This phenomenon occurs when magnetizing the atomic nuclei of materials. Each proton and neutron in the nucleus has a spin (angular momentum) and normally these nuclei are randomly oriented. Protons that are normally randomly oriented within the material e.g. relevant for this thesis, water nuclei of the tissue being examined, are aligned by using a powerful, uniform, external magnetic field (by the main magnet in MRI). Unless its orientation is shifted by another external field that results in an angle with the main magnetic field, a proton aligned along the main magnetic field will be in equilibrium and will not emit any signal. Following this, the alignment (or magnetization) is disrupted through the use of external radio frequency (RF) energy. The disrupted nuclei later tend to align themselves and in so doing emit RF energy. This phenomenon

of self-realignment is known as relaxation and the time it takes to occur is called the relaxation time. Following the initial RF, the emitted signals by the nuclei are measured after a certain time period. Frequency information contained in the signals is converted to corresponding intensity levels by a technique called Fourier transformation, and is then displayed as a matrix of gray scaled pixels. Different types of images can be created by varying the application and collection of RF pulse sequences. The time interval between successive pulse sequences to image the same slice of data is known as repetition time (TR). The time interval between the delivery of the RF pulse and the reception of the echo signal is called time to echo (TE).

Human tissue can be differentiated according to different relaxation times. There are two kinds of relaxation times, longitudinal relaxation time (T1) and transverse relaxation time (T2). T1 is the time it takes for the excited protons to return to equilibrium i.e. realign themselves with the external magnetic field. T2 is a measure of how long it takes for protons to spin parallel to the main field to lose phase coherence. MRI scans using T1- and T2-weighted sequences are the most common. Short TE and TR times produce T1-weighted (T1w) images (Figure 2.11(a)) and longer TE and TR times produce T2-weighted (T2w) images (Figure 2.11(b)). T1 and T2 properties of tissue are largely responsible for the contrast and brightness of these images. These contrast in images essentially leads to segmenting tissues inside the head to build a realistic head model using image processing. In T1w, tissues inside the head can be contrasted from brighter to darker as WM (short T1 relaxation time), GM (longer T1) and CSF. In these images, the tissues from brighter to darker are CSF or skull spongiosa (long T2 relaxation time), GM (shorter T2) and WM (shortest T2).

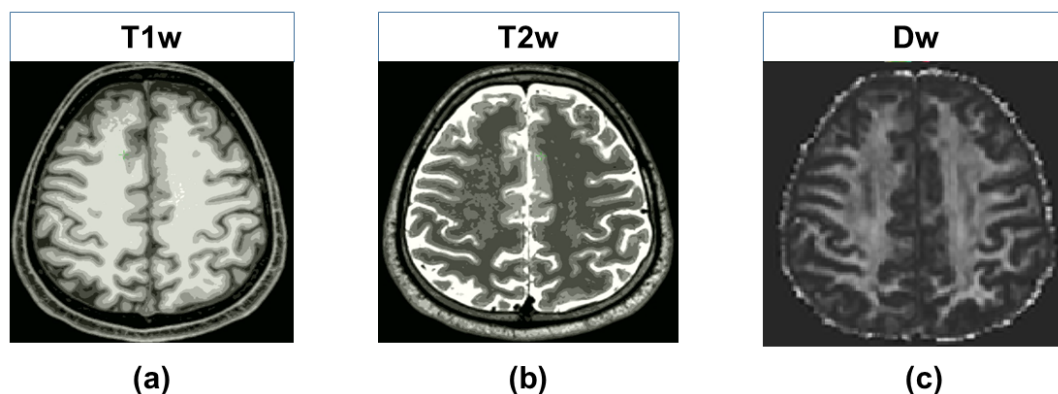


FIGURE 2.11: Three different MRI images are shown (a)T1W (b)T2w (c)Dw, based on different measurement parameters

In addition to T1w and T2w images, diffusion-weighted (Dw) MRI images are also taken. In Dw imaging, water molecules are measured by sending two consecutive, first and second, gradient pulses, which dephase and rephase the spins (protons) respectively. If no movement of spins occur between the two pulses the resultant received signals are almost without attenuation. If there is the movement of spins after the first dephasing pulse, lack



imaging (fMRI), which are based on indirect phenomena such as metabolic processes such as blood oxygenation, the main advantages of EEG and MEG are their high temporal resolution of milliseconds (ms) and their ability to directly measure electrical brain activity. It should be noted, however, that EEG and MEG have more limited spatial resolution compared to fMRI and their sensitivity decreases for sources distant from the sensors (e.g., sources in subcortical regions). Despite the fact MEG and EEG measure the same underlying brain activity, these two modalities differ in some important properties and features. MEG is more capable of detecting quasi-tangential sources compared to EEG which can measure both quasi-radial and quasi-tangential sources [114]–[116]. MEG signals, however, have a higher SNR for more superficial sources, since the quasi-radial biological noise attenuates the MEG signals less than EEG signals [117]. The high sensitivity of MEG to tangential currents means that MEG mainly measures activity occurring in the walls of cortical fissures.

Among the most frequently studied brain networks in source analysis for the study of EEG and MEG sensitivity differences, especially relevant for this thesis work, is the human somatosensory system [16], [118]. As in [119], SEP and SEF topographies and the reconstructed dipole source at Brodmann area 3b from the two modalities showed orthogonality to each other. Moreover, due to its mainly tangential orientation and superficial location, subsequent studies examined differences in EEG/MEG sensitivity profiles from the source reconstruction of the P20/N20 component [115], [120], [121]. In the studies [115], [120], it was shown through the source analysis of the P20/N20 SEP and SEF that a combined approach of the two modalities EEG and MEG outperforms a single modality-based approach.

## 2.8 Realistic volume conduction modeling

Realistic volume conduction modeling of the human head is essential to calculate the electric field or current density induced in the human head from tDCS and to locate the underlying source generators that produce signals of interest in an EEG or MEG measurement. A volume conductor is by definition a continuous passive conducting medium and modeling is to model its geometry and electromagnetic properties. It is very important to accurately estimate these properties to build a realistic enough model for source analysis (forward and inverse modeling) and tDCS stimulation. As the human head contains several different tissues with varying conductivities, inter- and intra-individually especially the skull, modeling becomes a very demanding task. Moreover, realistic geometric modeling is also limited by the resolution and contrast difference quality among the different tissues in the recorded image. As we use MRI, its limitations necessitate that volume conductor modeling for source analysis and tDCS simulations should be simplified and homogenized. More detail oriented and highly accurate head models require considerable work and time to first segment into several tissue compartments (more than 6) and second use advanced mathematical methods with very high computational time to solve them [122], [123]. This especially becomes

very problematic due to time constraints when running a source analysis and tDCS simulation pipeline before the application in an experimental tDCS paradigm.

Traditionally, a three-compartment isotropic head model with realistic geometric segmentation of scalp, skull and brain tissue from MRI data is used for source analysis [118], [120], [124]. More realistic head models include CSF, GM and WM by further realistically segmenting the brain and differentiating the skull into skull spongiosa and skull compacta tissue compartments. Instead of making the model isotropic, we can make the model realistically anisotropic for the brain by integrating DTI data [113], [125], [126] in the model. For this thesis work, we build a realistically shaped six compartment head model with anisotropy. In the following, we explain the major tissue compartments and their importance in head modeling in this thesis.

**The human skull:** EEG, combined EEG/MEG and tDCS forward modeling is significantly influenced by tissue compartment conductivities. In this regard, skull is one of the most sensitive tissue compartments. Due to its low conductivity, it attenuates electrical brain signals when recorded with EEG. It is also important to note that the skull probably consists of variable conductivity values throughout its whole structure [127]. The whole skull structure can be divided into three layer parts, where a relatively high conductive skull spongiosa tissue is situated between two layers of low conductive skull compacta. So in this regard, modeling the whole skull as a three-layered skull (compacta-spongiosa compacta) with possible skull holes and estimating individual conductivity is more important than geometrically accurate modeling of the skull tissue [128]. While segmentation of the skull from CT images results in better modeling compared to MRI, it is unjustified to use it only for this purpose due to high radiation risks. Progress in modern imaging techniques such as MRI has enabled researchers to model the skull's anatomy more precisely, including the use of T2w images with high resolution (1 mm) that can distinguish spongiosa from compacta [128]. Results from source analysis with EEG and tDCS showed that a three skull layered structure does have an influence [4], [128]–[133]. Skull conductivity is a very critical parameter in forward modeling and relative to scalp or brain tissues as its conductivity is one order of magnitude lesser [6]. The influence of skull conductivity irregularities on electric potential distributions has been studied in [113]. A narrow variation in skull conductivity can have a significant impact on modeled electric fields, causing localization errors of tens of centimeters and orientation errors of over 25 degrees. Regarding the EEG source analysis of the P20/N20 component of the somatosensory system, Vorwerk et al. ([6]) showed that natural variations in experimentally calculated conductivity values of the different head tissues lead to different results. In this regard, variations in skull conductivity led to the greatest effect on forward ([6], Table 2) and inverse source analysis [6]. For tDCS, these changes can also lead to four-fold higher amplitudes and unrealistic orientations of the model current density [5], [11]. For measuring skull conductivity, a variety of measurement techniques have been studied such as electrical impedance tomography (EIT)

[134], magnetic resonance EIT (MREIT) [135], magneto acoustics tomography (MAT) [136], and direct application of current (DAC) [4], [137]. Until now, their use in extensive research has been restricted by the need for additional and specialized equipment. Various studies have shown EEG being more sensitive to different skull conductivity values compared to MEG [113], [116], [138]–[144]. Several studies have already been conducted to measure skull conductivity using EMEG and MRI for three compartment head models [120], [124], [134] and initially with realistic head models [123]. In these studies, skull conductivity was estimated in a calibration procedure by conducting a source analysis of the P20/N20 somatosensory component. There have been studies in which skull conductivity was estimated using only SEP data [145], [146], however, additional SEF data stabilizes the estimation [147]. This is because EEG and MEG data complement each other [115], [116], and MEG localizations are insensitive to skull conductivity [118], [144], [146]. Based on these observations, this thesis utilizes the sensitivity differences of EEG and MEG, together with a combined EEG/MEG and MRI approach, to calibrate the conductivity of the skull noninvasively.

**Cerebrospinal fluid (CSF):** The majority of EEG/MEG source reconstruction studies use three-compartment head models that separately represent the inner skull, outer skull, and scalp surfaces as homogenized compartments. The CSF compartment in the skull is still excluded from these models, although it is highly conductive compared to scalp and brain tissue compartments. In a study of seven subjects varying in age from 4.5 months to 70 years, its conductivity was measured to be 1.79 S/m, on average [113]. Because the CSF compartment possesses stable conductivity, modeling it is only a matter of segmenting its complicated geometry. As a result of advances in structural imaging of the inner tissues of the brain, this segmentation is feasible because the cavities (i.e., sinus cavities) can easily be separated from the CSF compartment by highly contrasted grey-scale pixels in T2w MRI that appear white. Additionally, the CSF is included in volume conductor models because it has a high influence on all three methods (EEG, MEG, and EMEG) unlike the skull, which has a low influence on MEG [113], [127], [128], [138], [139], [148], [149].

**Gray and White matter (GM, WM):** It is also a simplification of three-compartment models to represent gray matter and white matter as a single homogeneous compartment along with CSF with an isotropic conductivity of 0.33 S/m. Studies investigating this phenomenon have shown that the difference in conductivity between white and gray matter (WM: 0.14 S/m and GM: 0.33 S/m) affects EEG, MEG, and EMEG source analysis [3], [6], [150]. Additionally, EEG and MEG measurements show that the main sources are located within the GM, but not in the WM, thus GM can be used to reduce the size of the model's source space [114], [122], [151]. Anisotropic conductivity is present in both gray and white matter. The anisotropy within the white matter can be particularly high, especially in pyramidal tracts. Grey matter anisotropy is significantly lower than white matter, and as a result, measuring it with 3T scanners may lead to errors due to partial volume effects in the CSF compartment. Earlier studies demonstrated a minor effect

of anisotropic conductivity modeling on EEG/MEG source localization. On the other hand, it might have a significant impact on the orientation and strength of the source [122], [152]. Moreover, it is generally considered that the source orientation component also contains important localization information [153], [154]. Researchers used a fixed ratio for fiber directions in earlier studies, but with the development of diffusion tensor imaging and the introduction of the correlation between diffusion and conductivity tensors [113], newer studies use the eigenvalues of diffusion tensors for this purpose [154]. In the present thesis, based on findings of [123], only white matter anisotropy is included for chapter 3 and 4.

**Skin(scalp):** The electrical properties of skin strongly depend on internal, physiologic or pathologic conditions and on external, environmental or experimental factors [155]. Since many bioelectrical measurement methods (e.g., ECG, EEG, EMG), track the electrical phenomena inside the body via the skin surface electrodes, the physical properties of the skin inevitably affect the obtained signal. Skin conductivity is highly variable with hydration level, corneum layer thickness, healthy or ill status, subject age, gender and the body part considered. Moreover, factors external to the body, such as environmental temperature and humidity or the presence of sponges and electrodes, can considerably modify skin conductivity [155]. Researchers may not consider an accurate skin model and include the head's outer tissues (skin, fat, muscle) in a single layer of scalp [156]–[159]. As reported in [160], skin consists of several layers (stratum corneum, cellular epidermis and dermis) with different thicknesses and conductivities, thus an homogenization procedure is often considered [161]. In the literature dealing with low frequency dosimetry (from DC to 10 kHz), skin conductivity, assumes several values (from 0.0002 S/m up to 0.465 S/m) spanning more than three orders of magnitude. The lowest value of skin conductivity, found in literature is 0.0002 S/m, it is reported in the generic IT'IS database [162] and refers to the dry skin as predicted by the dispersive model of [163] from 10 Hz to 10 kHz. The highest  $\nu$ , is 0.465 S/m. It was derived in [164] and typically refers to the scalp, a thick homogeneous tissue that incorporates the skin and the subcutaneous adipose tissue (SAT), as well as the fat and the muscle. Two noteworthy intermediate values for are 0.05 and 0.17 S/m. The latter is reported in the low- frequency IT'IS database [162] and was obtained by extrapolating experimental values in accordance with the dispersion characteristics of biological tissues [165]. The value 0.08 S/m is used in two models in which skin and fat are considered as a unique tissue [8], and corresponds to the conductivity of the fat as reported in [166].

## 2.9 Theoretical basis for source analysis

### 2.9.1 Overview

The EEG and MEG modalities are able to detect both electric and magnetic fields produced by neuronal current sources. There are two types of current fields, the primary and secondary current terms, which reflect microscopic

passive cellular currents and the macroscopic electric field, respectively [167]. The progress of the recording systems has made it possible to estimate the primary currents. A two-stage approach is needed to estimate such currents or sources. As a first step, it is essential to formulate a model of the recorded potentials at the sensors' potentials in relation to active neurons/sources in the brain [168]. This problem is commonly known as the Forward Problem. The second step consists of attempting to identify the primary source of the recorded brain signals. This is referred to as the Inverse Problem. To solve the Inverse Problem, it is essential to find a solution for the Forward Problem. In the following section, we will discuss the theoretical and mathematical background of forward and inverse modeling.

## 2.9.2 EEG and MEG forward modeling

### 2.9.2.1 Forward problem

With respect to EEG and MEG, the forward problem is solved by iterative simulations of electric potentials at the surface of the head and magnetic fields near the surface of the head for a given source of current in the brain. Based on a geometrical model of a human head [118], [169], these simulations are carried out. As a result, Maxwell's equations constitute the basis for electromagnetism and thus the forward problem in bioelectromagnetism.

$$\nabla \times \mathbf{E} = -\frac{\partial \mathbf{B}}{\partial t} \quad (2.1)$$

$$\nabla \times \mathbf{H} = \mathbf{J} + \frac{\partial \mathbf{D}}{\partial t} \quad (2.2)$$

$$\nabla \cdot \mathbf{B} = 0 \quad (2.3)$$

$$\nabla \cdot \mathbf{D} = \rho \quad (2.4)$$

with

**E**: Electric field (volt per meter ( $V/m$ ))

**H**: Magnetic field (ampere per meter ( $A/m$ ))

**B**: Magnetic flux density ( $T = kg / (s^2 A)$ )

**D**: Electric displacement field ( $C/m^2$ )

**J**: Current density ( $A/m^2$ )

$\rho$ : Volume charge density ( $C/m^3$ )

with units:

$V$  = volt,  $m$  = meter,  $A$  = ampere,  $T$  = tesla,  $kg$  = kilogram,  $s$  = second,  $C$  = coulomb.

The material equations listed below supplement Maxwell's equations:

$$\mathbf{D} = \epsilon \mathbf{E} \quad (2.5)$$

$$\mathbf{B} = \mu \mathbf{H} \quad (2.6)$$

$$\mathbf{J} = \sigma \mathbf{E} \quad (2.7)$$

where  $\epsilon$ (F/m) is the permittivity,  $\mu$ (H/m) is the permeability,  $\sigma$ (S/m) is the conductivity.

The properties at the interfaces of different media are given by the boundary conditions:

$$\mathbf{n} \times (\mathbf{E}_2 - \mathbf{E}_1) = 0 \quad (2.8)$$

$$\mathbf{n} \times (\mathbf{H}_2 - \mathbf{H}_1) = 0 \quad (2.9)$$

$$(\mathbf{D}_2 - \mathbf{D}_1) \cdot \mathbf{n} = \rho_s \quad (2.10)$$

$$(\mathbf{J}_2 - \mathbf{J}_1) \cdot \mathbf{n} = -\frac{\partial \rho_s}{\partial t} \quad (2.11)$$

with  $\rho_s$  representing the surface charge density at the interface and  $\mathbf{n}$  being the outward normal direction from material 1 to 2. The equations 2.8, 2.9 indicate the continuity in the tangential direction and 2.10, 2.11 represent the discontinuity in the medium. In the low-frequency regime of EEG and MEG forward problem (below 1000 Hz), the quasi-static approximation of Maxwell's equations can be used. This approximation refers to treating the electrical and magnetic fields as in steady-state for any time instant, which means that the secondary effects of the time variation are neglected [138]. Thus, Maxwell's equations reduce to:

$$\nabla \times \mathbf{E} = 0 \quad (2.12)$$

$$\nabla \times \mathbf{H} = \mathbf{J} \quad (2.13)$$

$$\nabla \cdot \mathbf{B} = 0 \quad (2.14)$$

$$\nabla \cdot \mathbf{D} = \rho \quad (2.15)$$

The electric field can thus be represented by a potential ( $\phi$ ):

$$\mathbf{E} = -\nabla \phi \quad (2.16)$$

In the case of the EEG/MEG forward problem, the total current density  $\mathbf{J}$  can be assumed to be composed of conduction current density  $\sigma \mathbf{E}$  and the so-called primary current  $\mathbf{J}_p$  (representing brain neural activity)

$$\mathbf{J} = \sigma \mathbf{E} + \mathbf{J}_p \quad (2.17)$$

and 2.17 2.17 becomes the Poisson equation for the electric potential on a head domain  $\Omega$ :

$$\nabla \cdot (\sigma \nabla \phi) = -\nabla \cdot \mathbf{J}_p \quad (2.18)$$

with homogeneous Neumann boundary condition on the head surface  $\Gamma = \partial\Omega$

$$\mathbf{n} \cdot (\sigma \cdot \nabla\phi) = 0 \quad (2.19)$$

The Poisson equation for the magnetic field can be obtained by substituting the magnetic flux density ( $\mathbf{B}$ ), which is equal to  $\mu\mathbf{H}$ , with the curl of the magnetic potential ( $\mathbf{A}$ ) in equation 2.13 2.13

$$\nabla^2 \mathbf{A} = -\mu\mathbf{J} \quad (2.20)$$

This leads to the representation:

$$\mathbf{A}(\mathbf{x}) = \frac{\mu}{4\pi} \int_{\Omega} \frac{\mathbf{J}_p(\mathbf{x}') - \sigma(\mathbf{x}') \nabla\phi(\mathbf{x}')}{|\mathbf{x} - \mathbf{x}'|} d\mathbf{x}' \quad (2.21)$$

A well-used assumption that is used in EEG/MEG forward problem is to represent the source with the mathematical point dipole. The mathematical point dipole can be represented as:

$$\mathbf{J}_p(\mathbf{x}) = \mathbf{m}_0 \delta(\mathbf{x} - \mathbf{x}_0) \quad (2.22)$$

$$\Psi = \int_S \mathbf{B} dS = \oint_l \mathbf{A}(\mathbf{x}) d\mathbf{x} \quad (2.23)$$

with  $\mathbf{m}_0$  is the dipole moment,  $\mathbf{x}_0$  is the dipole position and  $\delta$  is the Dirac delta function. Using Stokes theorem, the magnetic flux  $\Psi$  measured by using a magnetometer with surface area  $S$  and circumference  $l$  can be written as:

$$\Psi = \underbrace{\frac{\mu}{4\pi} \oint_l \int_{\Omega} \frac{\mathbf{J}_p(\mathbf{y})}{|\mathbf{x} - \mathbf{y}|} d\mathbf{y} \cdot d\mathbf{x}}_{\text{primary magnetic flux}} + \underbrace{\frac{\mu}{4\pi} \oint_l \int_{\Omega} \frac{-\sigma(\mathbf{y}) \nabla\phi(\mathbf{y})}{|\mathbf{x} - \mathbf{y}|} d\mathbf{y} \cdot d\mathbf{x}}_{\text{secondary magnetic flux}} \quad (2.24)$$

### 2.9.2.2 Forward solution

The forward problem for EEG and MEG can be solved analytically and numerically. In both the single and distributed dipole sources scenario, the EEG and MEG forward solution has proven to be unique [139], [170]. Solving the forward problem analytically is possible for some geometric head models like multi-sphere models [170]. Realistic head models, however, require a more numerical-based approach. Methods such as bounded element methods (BEM) [170], finite element methods (FEM) [139] or finite difference

methods (FDM) [125] are the most commonly used techniques for numerical based forward solutions. In this thesis, modeling of the electromagnetic fields in a geometrically demanding anisotropic and homogenous head volume conductor is carried out with FEM [122], [152]. In order to perform FEM with timing efficiency, it is important to choose the right method to deal with the singularity introduced by the mathematical dipole. To solve the singularity problem, methods such as the partial integration approach, full subtraction approach, venant approach and the H(div) approaches exist [171]. In this thesis work, for chapters 3 and 4, the Venant approach is used for its computational efficiency and high accuracy [15], [139]. As the complexity of the geometries of the modeled volume increases, FEM requires a larger number of elements to model it. However, the use of sparse matrices results in lower computing costs [172]. FEM is based on the principle of discretization. It is possible to divide the volume into many small subdomains if the governing equations are too complex to solve analytically. By combining all the equations for each element, the solution can be approximated. Tetrahedra and hexahedra are the most common geometric element shapes; however, other geometries are possible as well. As the element size decreases, the approximation becomes more accurate, but as the number of elements increases, the computational load increases as well. In areas where the solution does not change rapidly, larger elements can be used to increase computational efficiency. Vertices of finite elements are called nodes, and the combination of nodes and edges is called a mesh. When constructing hexahedral models, voxels are often converted into single elements directly from labeled MRI. As a result of hexagonal meshes, edges are less smooth and less realistic, leading to the staircase effect. The nodes are shifted to the material interfaces in order to counteract this effect [173]. Using this approach with multilayer sphere models, EEG source analysis was found to show significant error reductions compared to regular hexahedral methods [139].

### 2.9.3 Inverse modeling for EEG and MEG

#### 2.9.3.1 Inverse problem

In the past several decades, researchers have taken considerable effort to reconstruct the underlying electrical activity recorded with EEG and MEG. The inverse problem is defined as the problem of reconstruction of the primary electrical currents recorded at the scalp. Solving the inverse problem requires first solving the forward problem i.e creating simulated electromagnetic fields from a volume conductor head model for a distribution of sources. This phenomenon gives rise to a non-unique solution as there exists an infinite number of source configurations that are able to produce the same simulated EEG or MEG signals [174]. The nature of non-uniqueness for the inverse solution can be alleviated by constraining the problem to a fixed number of sources and defining the sources based on anatomical or neurophysiological constraints. The following linear equations provide the general formulation for the inverse solution of the EEG and MEG activity measurements:

$$\mathbf{Y}_{EEG} = \mathbf{L}_{EEG} \mathbf{j} \quad (2.25)$$

$$\mathbf{Y}_{MEG} = \mathbf{L}_{MEG} \mathbf{j} \quad (2.26)$$

Considering a time instant, a set of  $N_{EEG}$  ( $M_{MEG}$ ) number of EEG (MEG) sensors and  $N_{sp}$  source space points that represent the mathematical point dipoles,  $\mathbf{Y}_{EEG}$  ( $\mathbf{Y}_{MEG}$ ) is the  $N_{EEG} \times 1$  ( $M_{MEG} \times 1$ ) measurement vector,  $\mathbf{j}$  is the  $3N_{sp} \times 1$  source vector and  $\mathbf{L}_{EEG}$  ( $\mathbf{L}_{MEG}$ ) is the  $I_{EEG} \times 3N_{sp}$  ( $I_{MEG} \times 3N_{sp}$ ) the leadfield matrix (forward solution).

### 2.9.3.2 Inverse algorithm

Over the last decades, a variety of inverse reconstruction algorithms containing different a priori assumptions have been developed. The EEG/MEG inverse algorithms can be categorized into equivalent dipole approaches, current density approaches beamforming approaches and hierarchical Bayesian modeling [174], [175]. For this thesis work, the equivalent dipole approaches are briefly explained below as it is beyond the scope of this thesis to explain other approaches.

An equivalent dipole approach represents reconstructed activity inside the brain using a set of dipole sources. Thus, investigations that involve equivalent dipole approaches should meet the assumption of focality. Calculation of a dipole source involves the estimation of six dipole parameters, i.e. three location parameters and three dipole moment parameters. When using a moving dipole approach, these six parameters can be calculated for each time point. There is also the option of keeping the location (rotating dipole) and orientation constant (fixed dipole) for certain time points as well. Using a classic dipole fit algorithm, the three location parameters are computed using nonlinear optimization techniques, whereas the dipole moments are calculated using simple linear fitting [141], [142]. A common drawback of the dipole fit approach is that the optimization procedure might get trapped in local minima [143]. In this thesis (Chapter 3 and 4), for the analysis of somatosensory evoked responses and the estimation of its underlying sources, the preferred inverse method of choice was single dipole scans (SDS) [120], [169]. This method is classified as a linear equivalent dipole approach. The somatosensory EEG or MEG signals generated inside the brain are believed to be focal sources in nature [16], [119]. The disadvantage of SDS is the considerable increase in computational complexity when two dipole assumption is considered for the underlying sources. In the SDS algorithm, the goal is to find the source space location with the least residual variance (RV). The RV is defined as the squared deviation of the best fitting dipole to the measured data. As it is calculated for all source locations, we avoid the trap of a local minimum that would occur when using dipole fits. The RV is defined as follows

$$RV = \left\| \left( \mathbf{1} - \mathbf{L} (\mathbf{L}^T \mathbf{L} + \lambda^2)^{-1} \mathbf{L}^T \right) \mathbf{Y} \right\|^2$$

in which  $L$  represents the corresponding lead field matrix,  $Y$  is the measurement matrix depending on the measurement modality (EEG, MEG or EMEG) while  $\lambda$  is the regularization parameter. Alternative of RV metric is the goodness of fit (GOF) and it is calculated as  $GOF = 1 - RV$

As a technique to limit the unknown parameters in SDS, one can restrict the source space to only gray matter [as conducted in Chapter 3 and Chapter 4] or reduce the dipole orientations to only those perpendicular to the gray matter surface. This restriction is justified by the fact that EEG and MEG signals are produced by pyramidal cells, as pyramidal cells are perpendicular to cortex surfaces [114]. There should be consideration of gray matter modeling errors before imposing these kinds of constraints, which is why normal constraints were not applied in this thesis. The kinds of dipole models all have the issue that the number of dipoles must be determined a priori to avoid spurious results. A recent inverse approach proposed that this number parameter could be estimated from the measured data [174].

#### 2.9.4 Combined EEG and MEG source analysis

In the presence of continuously distributed neuronal currents, EEG and MEG are complementary and it has been demonstrated that information missing from EEG can be found in MEG, and vice versa. These observations encouraged researchers to continue their pursuit of simultaneous measurements and analysis of electrophysiological activity with EEG and MEG [115], [120], [176]. The EEG and MEG measurements are, however, based on different amounts of information, so their respective units of measurement are also different. In this regard, it becomes necessary to combine both modalities in one space in order to perform a combined source analysis of EEG and MEG. One approach to make this combination successful is the normalization of leadfield matrices using their norms [118]. For this thesis work, an SNR-based transformation is conducted in which EEG and MEG measurements are converted to a unitless quantity by pre-whitening of data for each channel according to the noise level. After this step, the leadfield matrices and measurements for EEG and MEG are stacked in a row-wise form after normalization with SNR to make them unit-free [120]. Finally, the equations 2.25 and 2.26 representing the leadfields from the final step are combined to produce the EMEG formulation.

# 3 A novel mc-tDCS optimization method with integrated EEG/MEG source analysis

## 3.1 Introduction

As previously explained in Chapter 2, tDCS is a non-invasive method of modulating neural activity in the brain by applying direct current to the brain in a non-invasive manner [46], [177]–[179]. In tDCS, a pair of two large sponge electrodes ( $25\text{--}35\text{ cm}^2$ ) are used to apply electric currents (mostly  $\leq 2\text{ mA}$ ) to the scalp. In general, for somatomotor applications [1], [40], [70], an anodal patch electrode is placed over the primary motor or somatosensory cortex and a cathodal patch electrode over the supraorbital area, contra- and ipsi-lateral to the side of stimulation, respectively. Due to the broadly distributed electric fields in the brain produced by this so-called anodal stimulation by the 2-Patch montage, tDCS results might suffer from inconsistencies [180], intra- [7], [181], and inter-subject variability [8], [44]. The cause of the variability might also be attributed to the lack of consideration of an individual targeting and to different conductive profiles of head tissues and anatomical and functional differences among subjects [77], [115], [150], [182], [183]. For example, Laakso [184] found a correlation between the modeled electric field intensity and the efficacy of tDCS in a motor evoked potential experiment, which means that inter-subject variability might be explained by differences in individual electric fields and thus that individual targeting and optimization might improve individual TES efficacy. For an individual targeting, not only target location is relevant, but especially also target orientation. Creutzfeldt and coworkers [22], who studied the effect of transcortical DC currents in the motor and visual cortex of the cat, showed that neurons are activated by radially-inwards and inhibited by radially-outwards (with regard to the cortical surface) oriented currents. Therefore, anodal stimulation might in fact excite underlying cortical regions, if at least parts of the target area are at radially-oriented gyral crowns or sulcal valleys, while this stimulation might be suboptimal for the mainly tangentially oriented targets on sulcal walls [57], [185]–[187]. Target areas are also often thought of including excitatory or inhibitory networks, which will thus be parameterized in the terminology of this work by a target orientation that differs by 180 degrees. An appropriate targeting thus means that (1) the injected current should not only be maximal in the target region-of-interest (ROI) in the brain (intensity) and (2) minimal in other areas (focality) but also (3) predominantly

oriented parallel (excitation) or anti-parallel (inhibition) to the target orientation (directionality) [22], [185]–[188]. Because of the complexity of such a targeting, mc-tDCS hardware combined with optimization methods has recently gained considerable interest to achieve an efficient trade-off between intensity, focality, and directionality [9], [11], [12], [14], [188], [189]. The mc-tDCS optimization (the tDCS inverse problem) includes the simulation of electric fields in the individual brain resulting from stimulation at the head surface using a quasi-static approximation of Maxwell’s equations (the tDCS forward problem) [9], [183], [190]–[192]. In this regard, for efficient targeting, the goal is first to determine the target individually and then utilize an appropriate inverse optimization method based on accurate forward simulations, to adapt the mc-tDCS montage individually for each subject, with the goal to achieve an improved neurophysiological stimulation effect in a subsequent tDCS experiment [10], [184]. In this way, differences in target location and orientation among subjects are taken into account. The individualized tDCS inverse approach also needs personalized head volume conductor forward modeling, not only concerning tissue geometries but also to individual tissue conductivities, and the most important conductivity parameter is for the skull as found in recent sensitivity investigations [5], [193].

In this chapter, in a group study of 10 healthy subjects, combined EEG and MEG is used for source analysis to reconstruct the main underlying source of the SEP and field SEF component at 20 ms post-stimulus, the P20/N20 component. This main source of P20/N20 activity is located in the primary somatosensory cortex (SI) in Brodmann area 3b [110], [150], [182], [194], [195]. Source analysis will be based on realistic finite element method (FEM) head modeling. Head modeling is personalized not only with respect to the head tissue geometries but skull conductivity is also estimated individually using an SEF/SEP calibration procedure [123], [150], [182]. This multi-modal approach to reconstruct the P20/N20 component is used to take full advantage of the measured EEG and MEG modalities as they provide complementary information for the same underlying sources. Previous studies have shown in theory [116] and practice [120], [123], [124], [196], [197] that source reconstructions from combined MEG/EEG can outperform single modality one’s. A detailed investigation in [150], [182] has furthermore shown that (1) a combined MEG/EEG approach for the P20/N20 component enables stable and accurate modeling of not only the source location in Brodmann area 3b, but especially also its orientation, which is not possible when only using a single modality, as well as (2) taking into account individual skull conductivity variability.

We introduce in this chapter a new mc-tDCS optimization method, the distributed constrained maximum intensity (D-CMI) approach, to compute individual stimulation montages for the reconstructed targets. D-CMI includes the concepts of maximum intensity (MI) [9] and constrained MI optimization (CMI) [189], but it has the additional goal of further distributing the optimization currents and thereby producing less tingling in the skin level. For specific choices of parameters, D-CMI can be identical to MI or CMI, so that D-CMI unifies and extends the class of intensity-optimization schemes.

The proposed new D-CMI mc-tDCS optimization pipeline does not only consider individual targeting (with regard to location and orientation) and head modeling, it also takes into account different experimental parameters such as safety limits, availability of a limited number of stimulation electrodes, limiting the current per electrode, and limiting the skin sensations. Based on MI and CMI, the new D-CMI method is presented and compared to the alternating direction method of multipliers (ADMM), a mc-tDCS approach for focality-optimization [188], and to the standard bipolar 2-Patch method. On the focality-intensity scale [9], [14], the ADMM method [188] used in this study is selected as an approach that represents focality instead of intensity-based tDCS montage optimization. Thus, in contrast to maximum intensity approaches, in ADMM induced currents aim for a focal stimulation of the target area, while minimizing currents in non-target regions. ADMM has already been used in an auditory experiment, where it could be shown that individualized transcranial electric stimulation increases gap detection performance [198].

All figures in this chapter were produced with custom MATLAB codes, SCIRun and CURRY 8. Statistical analysis was conducted with SPSS.

## 3.2 Methods and materials

### 3.2.1 Subjects

Ten right-handed healthy subjects ( $28 \pm 9$  years, 8 males and 2 females) participated in this study. The subjects had no history of psychiatric or neurological disorders and had given written informed consent before the experiment.

### 3.2.2 EEG and MEG parameters

A combined measurement approach for EEG/MEG is used in this thesis. EEG/MEG were used to acquire somatosensory data in a magnetically shielded room with the following parameters

#### EEG

- Using 80 AgCl sintered ring electrodes (EASYCAP GmbH, Hersching, Germany, 74 EEG electrodes plus additional six electrodes to detect eye movements)
- Digitization of the EEG electrode positions on the cap using Polhemus device (FASTRAK, Polhemus Incorporated, Colchester, VT).
- Additionally measuring electrocardiography (ECG) for the detection of cardiac activity,

#### MEG

- An MEG head system with 275 axial gradiometers and 29 reference sensors (OMEGA2005, VSM MedTech Ltd., Canada).

- The MEG reference coils were used to calculate first-order synthetic gradiometers to reduce the interference of magnetic fields originating from distant locations. Reduction of interfering magnetic field originating from distant locations by the calculation of first-order synthetic gradiometers using MEG reference coil.
- Tracking of head position inside the MEG in relation to the helmet with three magnetic localization coils, placed on nasion, left and right preauricular points.
- Reduction of head movements and prevention of CSF effects due to brain shift when combining EEG/MEG and MRI by taking measurements in supine position [199].

### 3.2.3 SEP and SEF measurement and pre-processing

For this thesis, recording is conducted simultaneously for SEPs and SEFs from right handed subjects by electrically stimulating the right hand index finger in a combined EEG/MEG setup. The electrical stimuli had a rectangular pulse width of 0.2 ms and was randomized with an inter-stimulus interval of 350 ms and 450 ms for habituation avoidance. The measurement was conducted for 40 minutes in blocks of 4 runs with each 10 minutes long. The recorded data was at a sampling rate of 1200 Hz and online lowpass filtering of 300 Hz. We pre-processed the combined SEF/SEP raw data using CURRY 8 by following the steps proposed in [119]. These steps are explained as follows

- A bandpass filtering of 20 Hz to 250 Hz to extract the relevant early components somatosensory data for analysis.
- A notch filtering of 50 Hz to eliminate the inherent power line noise in most EEG/MEG recordings.
- Deselection of data from bad EEG electrodes from visual inspection to reduce noise.
- Selecting stimulus trials of 200 ms duration (50 ms pre-stimulation and 150 ms post-stimulation) recorded from EEG/MEG and rejecting bad trials by first using a threshold-based semi-automatic procedure in CURRY 8 and followed by visual inspection deselection of bad trails.
- Averaging approximately 4000 trials from the 40 minutes of EEG/MEG finger stimulated somatosensory data to generate the SEF/SEP responses for analysis.
- Calculation of signal-to-noise ratio (SNR) following the method in [120] by whitening the data from each channel's individual noise level (calculated from the pre-stimulus interval) and resulting in a unit less measure (common unit for combined EEG/MEG) for both MEG and EEG.

### 3.2.4 MRI measurements and parameters

The technical and measurement parameters used for acquiring 3D-T1-weighted (T1w), 3D-T2-weighted (T2w), and diffusion-weighted (Dw) MRI datasets from MAGNETOM Prisma 3.0 T (Release D13, Siemens Medical Solutions, Erlangen, Germany) in this thesis are as follows:

- T1w scans were conducted with fast gradient-echo pulse sequence (TFE) using water selective excitation to avoid fat shift (TR/TE/FW = 2300/3.51 ms/8°, inversion pre-pulse with TI = 1.1 s, cubic voxels of 1 mm edge length).
- T2w scans with a turbo spin echo pulse sequence (TR/TE/FA = 3200/408 ms/90°, cubic voxels, 1 mm edge length).
- Dw scans with an echo planar imaging sequence (TR/TE/FA = 9500/79 ms/90°, cubic voxels, 1.89mm edge length).
- A one volume with diffusion sensitivity  $b = 0 \text{ s/mm}^2$  (i.e., flat diffusion gradient) and 20 volumes with  $b = 1,000 \text{ s/mm}^2$  in different directions, equally distributed on a sphere
- An additional volume with a flat diffusion gradient, but with reversed spatial encoding gradients was scanned and utilized for susceptibility artifact correction [126].
- During T1w measurement, gadolinium markers were placed at the same nasion, left and right preauricular points for landmark-based registration of MEG/EEG to MRI.
- All measurements were acquired in a supine position to reduce head movements and to prevent distorting CSF-brain volume conduction effects due to the brain shift [199] that would result from measuring MEG/EEG in a sitting position and MRI in a lying position.

### 3.2.5 Source reconstruction pipeline

In this thesis, in order to stimulate a target in the brain with tDCS, first, accurate reconstruction is performed of the underlying target source whose brain activity is recorded from EEG/MEG measurements. Reconstruction of the underlying source of the somatosensory P20/N20 component at Brodmann area 3b with a combined skull conductivity-calibrated EEG/MEG source analysis pipeline for the interest of this study. Source reconstruction, as mentioned in Chapter 2, requires forward modeling and inverse modeling. For forward modeling, an individualized skull conductivity-calibrated realistic forward model was built for each subject. The forward modeling steps are explained as follows.

### 3.2.5.1 Realistic head segmentation

In the first step of forward modeling, a six tissue compartment head model was created by segmenting T1w and T2w MRI images. The segmented realistic head model contains the scalp, skull compacta (SC), skull spongiosa (SS), cerebrospinal fluid (CSF), gray matter (GM), and white matter (WM) segmented tissue compartments. Segmentation was carried out by the following steps:

- Segmentation of tissues scalp, GM and WM from T1w MRI.
- Registration of T2w MRI to the T1w scan using an affine registration approach implemented in FSL [200], resulting in the T2w/T1w image.
- Segmentation of tissues SC, SS, CSF, and brain using T2w/T1w image following the steps in [150], [182].
- Combining the six segmented tissues resulting from T1w and the registered T2w/T1w to create a head model with six compartments containing scalp, SC, SS, CSF, GM, WM and labeled as 1 to 6. Each compartment has a resolution of 1 mm.
- Cutting off a sufficient distance (40 mm on average) below the skull to reduce computational complexity as suggested in [201].

### 3.2.5.2 Mesh creation

After the creation of the labeled six compartment head model, a geometry adapted hexahedral FEM meshes of 1 mm mesh size were constructed, as shown in Figure ) for each subject using the freely available software SimBio-VGRID

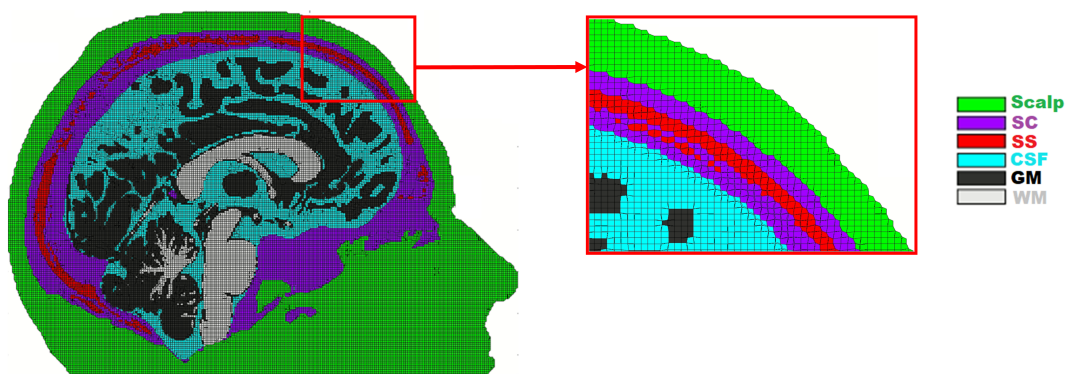


FIGURE 3.1: A hexahedral FEM mesh of 1mm resolution is shown with a node-shift of 0.33 to mitigate staircase effects

Using the voxels from the segmented model as elements for the hexahedral meshing, a node shift method was applied to smooth compartment

interfaces resulted in a final hexahedral FEM mesh that conforms to the actual geometry and eliminates the stair-case effects of a regular hexahedral voxel grid. If there were nodes on a two-material surface, they were moved towards the centroid of the voxel set with the least number of incident voxels (i.e., the material occurring 3 or fewer times than 8 surrounding voxels). In the FEM computations, a node-shift of 0.33 made sure that the angle of vertices at element vertices were convex as well as that the Jacobian determinant was positive. This meshing strategy improves numerical accuracy without increasing computation time and memory usage [139] and thus should be used in head volume conductor modeling. In Figure 3.1 6 compartment head modeling meshing is shown.

### 3.2.5.3 Tissue compartment conductivities

For the next step, in realistic forward modeling, the six tissue compartment head model has to be assigned conductivity values. For the scalp, CSF and GM conductivity values as 430 mS/m [202], 1790 mS/m [203] and 330 mS/m [123] were set. For the WM tissue compartment, anisotropic conductivity was assigned with DTI-constructed tensors. The DTI tensors were created with the following steps:

- Correcting Dw MRI images for eddy current and susceptibility artifacts using a reversed gradient approach [126].
- The corrected images were then registered to the T2w image and 3D diffusion tensors were derived following [200].
- In the final step, the WM conductivity anisotropy tensors were calculated using an effective medium approach [113] and integrated into the geometry adapted hexahedral FEM model following [154].

### 3.2.5.4 Source space creation

In order to perform the inverse solution part of source analysis by dipole scanning, source space was created within the GM compartment that has a resolution of 2 mm and without restrictions on alignments (no normal constraints).

Unlike the forward problem, which has a unique solution and high resolution (1 mm, see Section 3.2.5.2), the inverse problem is limited to a 2 mm source space resolution. To fulfill the so-called Venant condition, all sources were located in GM and sufficiently remote from neighboring tissue compartments, i.e., for each source node, the closest FE node should only belong to GM elements. For the chosen Venant dipole modeling approach, it must be met to prevent numerical problems and unrealistic source modeling [122], [139], [204]. It may occur on the other hand that monopoles will be induced in the adjacent compartments, such as the CSF and white matter, which is unrealistic for source modeling [122]. Figure 3.2(a) shows the source space for the GM in the whole cortex and how source space is contained in GM on the MRI T1 image.

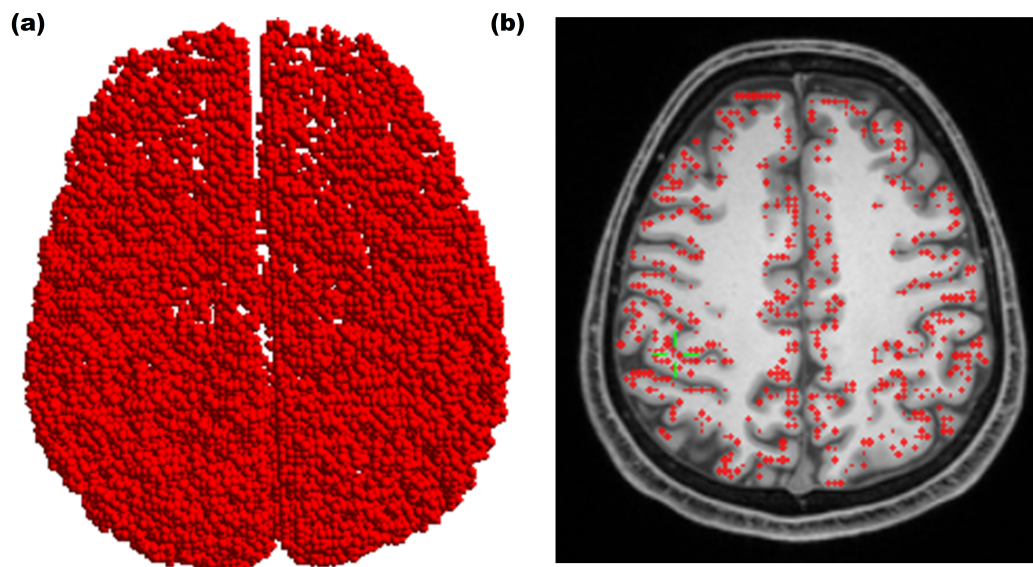


FIGURE 3.2: Source space of 2mm resolution (a) showing the source space (red dots) for the brain and (b) showing source space overlapped in T1 MRI image where it is shown that source space is confined to the grey matter only.

### 3.2.5.5 EEG and MEG leadfields creation

In order to create the final forward models, SimBio to compute leadfields for MEG and EEG is used with an isoparametric Lagrangian FEM approach with trilinear basis functions. For sufficient computational speed, MEG and EEG leadfield bases [172] and an algebraic multigrid preconditioned conjugate gradient (AMG-CG) solver was used, which has proven to be stable for the considered tissue conductivity inhomogeneities and anisotropies [205], [206].

### 3.2.5.6 Individualized skull conductivity calculation

The relationship between the estimation of individualized skull conductivity and combined EEG/MEG reconstruction of the target source (i.e. in this thesis work, the P20/N20 somatosensory component) is inter-connected. The skull conductivity is an individually varying phenomenon that significantly effects the EEG and tDCS forward modeling but almost has no influence on the MEG forward modeling [123], [182]. Moreover, EEG signal topographies might still be influenced by overlaid thalamic activity at the P20/N20 peak but disregards MEG topographies and, as a consequence, the combined EEG/MEG source reconstruction process of the Brodmann area 3b target is effected as a whole [110], [120], [182], [194], [195], [207]–[210]. Making use of the complementary information provided by the modalities, the location of P20/N20 target at the primary somatosensory cortex (S1) was determined by using the MEG 20 ms peak as suggested by [110], [120], [182], [195], [208], [210]. When the location of the target (Brodmann area 3b) is individually localized, information from the EEG measurement about the P20/N20 somatosensory component is used in the estimation of the skull conductivity

for each subject [182]. This information is related to P20/N20 targets strength and orientation [182] at the Bordamann area 3b which plays a vital role when using mc-tDCS optimization to stimulate the Brodmann area 3b target. The algorithm for the skull conductivity calibration procedure can be explained as follows algorithmically, the calibration procedure can be summarized as follows:

1. Define a discrete set of skull conductivities, e.g.  $C = [C_1, C_2, \dots, C_n]$
2. For each head model with skull conductivity  $C_i$ , for  $i = 1 \dots n$ 
  - (a) Use a deviation scan at the 20 ms SEF peak to determine the location, a first orientation and first magnitude of the dipole source.
  - (b) Keep the location of (2(a)) fixed and calculate a second orientation and second magnitude using the least square fit of the 20 ms SEP topography to the fixed source location.
  - (c) Keep the location of (2(a)) and the orientation of (2(b)) fixed and calculate a third magnitude using a least squares fit of the 20 ms SEF topography to the fixed source location and orientation.
  - (d) For the calculated dipole of (2(c)), calculate the residual variance (RV) to the 20 ms SEP topography.
3. Select the conductivity that gives the lowest RV from step (2(c)).

In summary, the algorithm uses the complementary information provided by the measured P20/N20 MEG and EEG topographies. In the calibration and targeting procedure, while individually estimating the SC conductivity, to avoid overfitting, for SS conductivity, a fixed conductivity ratio of 1:3.6 for SC:SS is used, following the measurements of [4].

### 3.2.5.7 Somatosensory source reconstruction

For source reconstruction (inverse modeling) of the somatosensory P20/N20 target, CURRY 8 software was used. This analysis was performed by first loading the source space (see Section 3.2.5.4) and the MEG and EEG lead-fields (see Section 3.2.5.5) and then used by single dipole deviation scan (SDDS) inverse approach. The SDDS method was chosen based on the prior knowledge that the underlying source of P20/N20 somatosensory EEG/MEG component is focal and single dipolar in nature [110], [120], [194]. SDDS calculates the residual variance (RV) (or  $GOF=1-RV$ ) for each source space node resulting in SDDS map function. In this study, when only MEG SDDS scans (as in Section 3.2.5.6 for location calculation with MEG) were conducted, regularization was applied to subdue the effect of spatially high frequent data noise that might contribute in high radial dipole orientation components [120], [169]. Regularization was avoided for EEG and in combined EEG/MEG source reconstruction. SNR based transformation, as suggested by [120], was used to whiten the data (pre-stimulus interval noise calculation) that could result in the common unit less measures for EEG/MEG in a combined analysis.

### 3.3 tDCS forward modeling

tDCS forward modeling can be facilitated through the quasi-static approximation of Maxwell's equations for computing the electric potential. This results in the Laplace equation  $\nabla \cdot (\sigma \nabla \phi) = 0$  with  $\sigma$  being the conductivity tensor,  $\phi$  the electric potential, and inhomogeneous Neumann boundary conditions at two stimulating electrodes (i.e., -1 mA at a fixed cathode, +1 mA at an anode), and homogeneous one at the remaining model surface [183], [188], [191], [211].

For practical brain stimulation applications, especially with the small electrodes that is used here (PISTIM Ag/AgCl electrodes with a 1 cm radius), point electrode model (PEM) are used, which provides adequate accuracy for the tDCS forward problem [212]. To approximate the Laplace equation numerically, the same FEM head modeling method as in 3.2.5 is used, with the exception of the source and boundary conditions. From the numerically approximated potential at the nodes, computations of the electric field  $E = -\nabla \phi$  and the current density  $J = \sigma E$  for each geometry-adapted hexahedral mesh element can be conducted.

### 3.4 Multi-channel tDCS formulation and optimization methods

#### 3.4.1 Overview

In order to target effectively with tDCS and make optimal use of the recently developed mc-tDCS hardware, several personalized mc-tDCS optimization protocols have been developed over the years in order to provide the best targeting and optimal use based on either optimal intensity or focality, depending on the specific desired outcome after tDCS stimulation [9], [11], [12], [188], [189].

In this chapter, the development of the mc-tDCS optimization protocol is conducted as a preparatory simulations based step to guide the follow-up somatosensory SEF/mc-tDCS/SEF experiment (Chapter 4). The following parameters and limitations were considered when developing the optimization protocol :

- Total number of 39 possible fixed positions on the scalp for tDCS electrodes provided by Startstim Neoprene Headcap.
- Total number of 8 maximum stimulation electrodes allowed for stimulation from the 39 possible positions.
- Accurate and realistic head volume conductor models and accurate numerical field modeling to solve the tDCS forward problem.
- A total injection current of 2 mA, and limiting the current per electrode for safety reasons.

- Potential facilitation of sham condition by reducing skin sensations via limiting the current per electrode

The resulting individualized mc-tDCS montages are used in a somatosensory experiment (see chapter 4) with the Starstim-8 (Neuroelectronics, Barcelona, Spain) mc-tDCS system with a maximum of eight out of 39 possible stimulation electrodes (i.e., 39 holes in the rubber cap into which stimulation electrodes can be inserted). Therefore, a digital recording of the  $m = 1, \dots, M$  with  $M = 39$  possible sensor positions was conducted, corresponding to the international 10/20 EEG system, for all subjects with a Polhemus measurement device. The  $M^{\text{th}}$  electrode was fixed as the reference electrode in all of the tDCS forward simulations. As a result, it must carry both positive and negative currents across all electrodes, such that the sum of the currents across all electrodes is zero current [9], [189].

The mc-tDCS optimization approaches requires a dipole target (with location and orientation information), the individual dipole target for each subject was calculated as a P20/N20 somatosensory source in Brodmann area 3b, reconstructed from combined EEG/MEG data as explained in Section 3.2.5.7. So, the general goal is to find an optimally targeting electrode montage for the individual P20/N20 SI target that is additionally fulfilling the above-described side-constraints, parameters and limitations. For this purpose, first of all, the superposition principle for a linear combination of all possible current injection patterns from the tDCS can be stated as [9]

$$\mathbf{e} = \mathbf{A}\mathbf{s} \quad (3.1)$$

$$\text{with } \mathbf{e} = \begin{bmatrix} e(\mathbf{r}_1) \\ e(\mathbf{r}_2) \\ \vdots \\ e(\mathbf{r}_N) \end{bmatrix}$$

$$\mathbf{A} = \begin{bmatrix} a_1(\mathbf{r}_1) & a_2(\mathbf{r}_1) & \dots & a_{M-1}(\mathbf{r}_1) \\ a_1(\mathbf{r}_2) & a_2(\mathbf{r}_2) & \dots & a_{M-1}(\mathbf{r}_2) \\ \vdots & \vdots & & \vdots \\ a_1(\mathbf{r}_N) & a_2(\mathbf{r}_N) & \dots & a_{M-1}(\mathbf{r}_N) \end{bmatrix}$$

$$\text{and } \mathbf{s} = \begin{bmatrix} s_1 \\ s_2 \\ \vdots \\ s_{M-1} \end{bmatrix}$$

As a general rule for notation, uppercase bold letters represent matrices, lowercase bold letters represent vectors and non-bold letters, either upper or lower case, represent scalars.

In eq. 3.1,  $\mathbf{A} \in R^{3N \times (M-1)}$  is the tDCS FEM influence matrix with entries  $\mathbf{a}_i(\mathbf{r}_j) \in R^{3 \times 1}$  i.e., the FEM simulated current vector in the  $j$ 's finite element due to stimulation of the  $i^{th}$  electrode pair (i.e., a positive unit current of +1 mA at the  $i^{th}$  electrode and a negative unit current of -1 mA at the reference electrode M) and  $N$  is the number of hexahedral volume elements in the FE discretization.  $\mathbf{s} \in R^{M-1}$  is the applied current vector from the (M-1) non-reference electrodes and  $\mathbf{e} \in R^{3N}$  is the resulting simulated forward modeling solution for the current density, i.e., a vector-valued quantity  $\mathbf{e}(\mathbf{r}_i) \in R^{3 \times 1}$  in each finite element. The influence matrix  $\mathbf{A}$  only has to be computed once by solving (M-1) FEM equation systems, as described in Section 3.3 and implemented in SimBio [183]. It can then be used to find the optimal mc-tDCS montage that best fits the stimulation goal, i.e., targeting the individual P20/N20 Brodmann area 3b, as well as fulfilling the additional optimization side-constraints.

In this chapter, an analysis and comparison of three mc-tDCS optimization methods is presented. These methods are, alternating direction method of multipliers (ADMM) from [188], maximum intensity (MI) from [9], the constrained MI (CMI) [189] and the novel mc-tDCS optimization approach presented for the first time in [213], the distributed CMI (D-CMI) which incorporates both MI and CMI optimizations. The D-CMI approach is an integration of both the MI and CMI methods. Throughout this chapter, importance is given to (a) summarize the important attributes of ADMM, MI and CMI methods (b) formulate the D-CMI method, which is an integration of both MI and CMI methods, (c) compare the mc-tDCS optimization methods to each other and (d) compare the three mc-tDCS optimization methods to the standard bi-polar 2-Patch to determine the additional advantage of individualized and optimized mc-tDCS for somatosensory stimulation.

The common argument for the selection of an intensity or a focality-based tDCS approach, when applying in an experiment, is addressed by analysing ADMM as a focality optimization approach [188] and MI, CMI and D-CMI as intensity-based optimization approaches. These optimization approaches lie on the focality-intensity scale as shown in [14]. The main focus in this chapter is on the intensity-based optimization approaches (MI, CMI and D-CMI). As stimulation will be conducted in the follow-up somatosensory experiment in Chapter 4 for the S1 area with short (10 min) mc-tDCS sessions, so, having a considerable stimulation effect on the somatosensory system requires using intensity optimization approaches.

### 3.4.2 Alternating direction method of multipliers (ADMM)

The ADDM method as proposed by [188], on the focality-intensity scale [14], [214] is more on the focality than on the intensity side of the scale. It is an optimal control problem for a Laplace equation with Neumann boundary

conditions with control and point-wise gradient state constraints. It maximizes the current in the target area and target direction while keeping the current in non-target regions under a given bound. The formulation is given as follows

$$\mathbf{s}_{\max} = \arg \max_{\mathbf{s}} \langle \mathbf{A}_{\text{target}} \mathbf{s}, \mathbf{o}_{\text{target}} \rangle \quad (3.2)$$

subject to  $w |\mathbf{A}_{\text{target}} \mathbf{s}| \leq \varepsilon$

where  $\mathbf{A}_{\text{target}} \in R^{3 \times (M-1)}$  is the submatrix of  $\mathbf{A}$  that corresponds to the target area, i.e., if the P20/N20 source was found in element  $j$ ,  $\mathbf{A}_{\text{target}} = [\mathbf{a}_1(\mathbf{r}_j), \dots, \mathbf{a}_{M-1}(\mathbf{r}_j)]$  and  $\mathbf{o}_{\text{target}} \in R^3$  is the orientation of the target source.  $\langle \cdot, \cdot \rangle$  indicates the inner product of the three-dimensional vectors.  $w$  is a weight allowing high currents in the target region while keeping currents in non-target regions below a threshold  $\varepsilon$ . To ensure convexity of the problem and uniqueness of a minimizer and control the applied currents, an L2 regularization term is introduced to penalize the energy of the applied current and an additional L1 term minimizes the number of active electrodes in the minimization procedure

$$\mathbf{s}_{\max} = \arg \max_{\mathbf{s}} \langle \mathbf{A}_{\text{target}} \mathbf{s}, \mathbf{o}_{\text{target}} \rangle - \alpha \|\mathbf{s}\|_2 - \beta \|\mathbf{s}\|_1 \quad (3.3)$$

subject to  $w |\mathbf{A}_{\text{target}} \mathbf{s}| \leq \varepsilon$

with  $\alpha$  and  $\beta$  the corresponding regularization parameters. Here the same ADMM parameterization was chosen as suggested in [188]. Rescaling is done, as also proposed by [188], so that the safety constraint with regard to the total injected current (2 mA) is fulfilled. The resulting electric fields are then taken for comparison and analysis. For the goal in this work, ADMM as the representative of the class of focal optimization approaches seems sufficient, but it should be mentioned that first comparisons of ADMM with other focality optimization approaches such as LCMV-beamforming [9] and least-squares or weighted least-squares approaches point to the superiority of ADMM with regard to its focality ([214], see Tables 3.2 and 6.3), surely depending also on the choice of parameters.

### 3.4.3 Maximum intensity (MI)

Due to different side constraints, on the focality-intensity scale [14], the MI method proposed by [9] is clearly more on the intensity than on the focality side of the scale. The MI formulation is stated as follows

$$\mathbf{s}_{\max} = \arg \max_{\mathbf{s}} \langle \mathbf{A}_{\text{target}} \mathbf{s}, \mathbf{o}_{\text{target}} \rangle \quad (3.4)$$

subject to  $\|\tilde{\mathbf{s}}\|_1 \leq 2S_{\text{Total}}$

with  $\tilde{\mathbf{s}} = \left[ s_1, s_2, \dots, s_{M-1}, -\sum_{m=1}^{M-1} s_m \right]$

$\tilde{\mathbf{s}}$  is the current injection pattern with a reference electrode current of  $\left(-\sum_{m=1}^{M-1} s_m\right)$  that makes sure that the overall injected current always sums up to zero and  $S_{\text{Total}}$  is the total injected current (2 mA in this case). The maximization of intensity in the desired direction at the target is a linear programming problem that can be solved by using the CVX toolbox [215].

### 3.4.4 Distributed constrained maximum intensity (D-CMI)

The D-CMI method is an extension of the constrained maximum intensity (CMI) optimization method which was presented by [189]. The CMI optimization problem can be stated as follows

$$\mathbf{s}_{\max} = \arg \max_{\mathbf{s}} \langle \mathbf{A}_{\text{target}} \mathbf{s}, \mathbf{o}_{\text{target}} \rangle \quad (3.5)$$

subject to  $\|\tilde{\mathbf{s}}\|_1 \leq 2S_{\text{Total}}$   
with  $\|\tilde{\mathbf{s}}\|_{\infty} \leq S_{\text{maxelec}}$

where  $S_{\text{maxelec}}$  is the maximum current limit per electrode. Since with 2 mA,  $S_{\text{Total}}$  is kept identical throughout this work, the CMI optimization approach is referred as CMI ( $S_{\text{maxelec}}$ ) and as CMI in general. D-CMI, presented here for the first time, aims at achieving high intensity in the target area, similar to MI and CMI, but the optimization function and the side-constraints are chosen in a way that the injected currents are further distributed over multiple electrodes, thus also reducing the sensations at the skin level. In D-CMI, an additional L2 regularization term for the optimization function and the side-constraints are chosen so that both the safety constraint for the total current is fulfilled and, as also proposed for CMI, an upper limit for the current at each electrode is realized by the optimization. The D-CMI optimization problem can then be stated as follows:

$$\mathbf{s}_{\max} = \arg \max_{\mathbf{s}} \langle \mathbf{A}_{\text{target}} \mathbf{s}, \mathbf{o}_{\text{target}} \rangle - \lambda \|\tilde{\mathbf{s}}\|_2 \quad (3.6)$$

where  $\lambda$  is an L2 norm regularization parameter that adds strict convexity to the problem with regard to the existence and uniqueness of a solution [188] and that can be used to further distribute the current over multiple electrodes. The D-CMI approach is also referred as D-CMI( $S_{\text{maxelec}}, \lambda$ ) to clarify the dependence on its two parameters (as  $S_{\text{Total}}$  is kept constant at 2 mA throughout this chapter). Because D-CMI( $S_{\text{maxelec}}, \lambda = 0$ ) is identical to CMI( $S_{\text{maxelec}}$ ) and D-CMI( $S_{\text{maxelec}} = S_{\text{Total}}, \lambda = 0$ ) is identical to MI, the D-CMI approach unifies and extends the class of intensity-optimization approaches. In the results Section 3.7, a parameter identification study for both  $S_{\text{maxelec}}$  and  $\lambda$  will be performed.

### 3.5 Standard 2 – Patch

Additionally, also comparison of the mc-tDCS optimization methods with the traditional standard 2-Patch stimulation setup is performed. For this purpose, for each subject two 5 cm x 5 cm sponge-like tDCS patches was simulated with a thickness of 4 mm and saline-fluid-like conductivity of 1.4 S/m [183]. Following the standard 2-Patch montage as used in ([70], [177]), for the stimulation of the somatosensory network, the patches were centered at the C3 (anode) and FP2 (cathode) electrode locations which were taken from the digitized Polhemus tDCS cap measurement as explained in Section 3.4. The patches were applied with a total injected current of 2 mA.

### 3.6 Quantification metrics

Selection of the most appropriate tDCS method for application in a somatosensory SEF/tDCS/SEF experiment (Chapter 4) depends significantly on considerably high enough injected currents reaching the target area in the direction of the target's orientation to have a maximum effect on the neuronal firing rates [22], [185], [186], [188].

Despite the fact that in the experiment, achieving high target intensity is of primary importance, other experimental conditions can easily be envisioned in which focality is paramount in order to avoid side effects arising from stimulation of unwanted regions, for example, prolonged stimulation of epilepsy patients with the goal of reducing seizure frequency and severity [216].

Further, the parameters of the selected tDCS method should allow for flexibility and adaptability to best match the available hardware and the desired results of a tDCS study. Quantification metrics can assist in this selection process by analysing the specific advantages and disadvantages of the different tDCS methods used in this study. The quantification metrics in [188], [214] were used, namely the average current intensity in the target region (IT), average current intensity in non-target regions (INT), directionality (DIR), parallelity (PAR), focality (FOC). These quantification metrics are defined and formulated as follows

- $$IT = \frac{\int_{\Omega_t} |\mathbf{A}\mathbf{s}| dx}{|\Omega_t|}$$

where

$\Omega_t$ : Target grey matter region

$|\Omega_t|$ : Grey matter Volume

x: Integration variable

The formulation used above is for general extended targets as in [188], [214]. The target area in this study is only the hexahedral mesh element that contains the reconstructed P20/N20 dipole. For constant  $\mathbf{A}_{\text{target}} \mathbf{s}$

over  $\Omega_t$ , it can be evaluated as  $IT = |\mathbf{A}_{\text{target}} \mathbf{s}|$ .

- $INT = \frac{\int_{\Omega_{nt}} |\mathbf{A}\mathbf{s}| dx}{|\Omega_{nt}|}$

where

$\Omega_{nt}$ : Non-target region (brain mesh elements excluding the target mesh element)

$|\Omega_{nt}|$ : Non-target region volume

- $DIR = \langle \mathbf{A}_{\text{target}} \mathbf{s}, \mathbf{o}_{\text{target}} \rangle$

The directionality (DIR) is defined as the inner product of the simulated current intensity  $\mathbf{A}_{\text{target}} \mathbf{s}$  with the target orientation vector  $\mathbf{o}_{\text{target}}$ .

- $PAR(\%) = \frac{DIR * 100}{IT}$

Parallelity (PAR) is defined as the percentage of current intensity that is oriented parallel to the target vector.

- $FOC = \frac{IT}{INT}$

Focality (FOC) is defined as the difference between the IT and INT of the averaged current density in the target.

## 3.7 Results

### 3.7.1 Individualized head modeling

The averaging over trials was used to generate the SEF/SEP responses, resulting in an average SNR of  $10 \pm 2.93$  and  $8.07 \pm 3.1$  for SEF and SEP, respectively, over all subjects. Exemplarily for subject S1, the P20/N20 SEF and SEP topographies together with the MEG and EEG sensors are shown in Figure 3.3(a) and (b), respectively. Figure 3.3(c) presents the six compartment head model segmentation, labeled as scalp, skull compacta (SC), skull spongiosa (SS), cerebrospinal fluid (CSF), grey matter (GM), and white matter (WM). The conductivity anisotropy of WM (Section 3.2.5.3) and the conductivity of the skull compartment (Section 3.2.5.6) were modeled individually. For the latter, the individual P20/N20 SEF and SEP topographies were used, together with the corresponding six compartment anisotropic head model as input to the skull conductivity calibration procedure (Section 3.2.5.6), which resulted in individual skull conductivities with a mean and a standard deviation for SC and SS of  $7.5 \pm 5.4$  mS/m and  $27 \pm 19$  mS/m, respectively. Finally, in

Figure 3.3(d), the 39 Polhemus-measured possible stimulation electrode positions of the Starstim-8 neoprene cap, registered on the surface of the head model, are shown together with their labels and the head model.

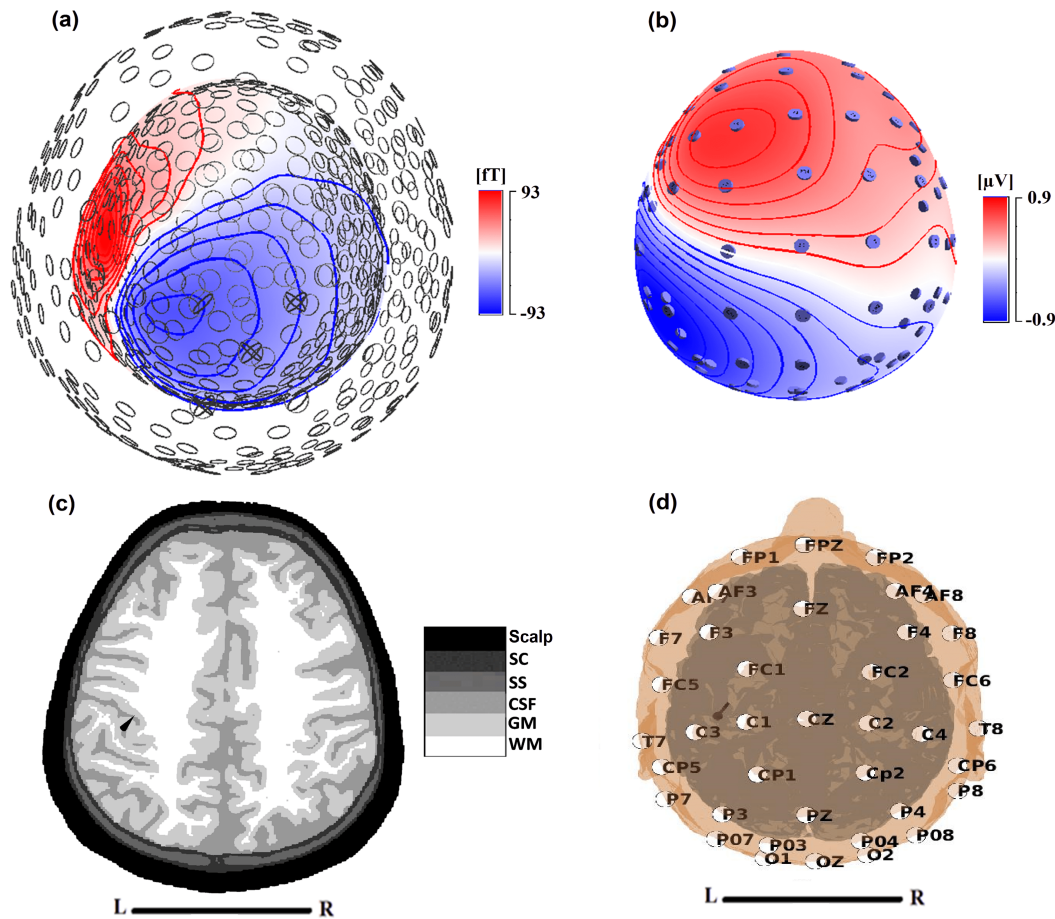


FIGURE 3.3: [MEG and EEG sensors with topographies 20 ms post-stimulation (P20/N20) and realistic head model with somatosensory dipole target from combined MEG/EEG (black cone) for subject S1: (a) MEG sensors and 20 ms SEF topography (b) EEG sensors and 20 ms SEP topography (P20/N20) (c) Six compartment segmented head model with compartments scalp, skull compacta (SC), skull spongiosa (SS), cerebrospinal fluid (CSF), grey matter (GM) and white matter (WM), as also indicated in the legend of the grayscale color scheme, and somatosensory dipole target from combined MEG/EEG (black cone) for subject S1 (d) Segmented head model showing skin surface (light brown), cortical surface (dark and light grey), mc-tDCS cap electrode positions with labels and somatosensory dipole target from combined MEG/EEG (black cone) for subject S1.

### 3.7.2 Somatosensory targeting

As described in Section 3.2.5.6, reconstruction of the P20/N20 targets for each subject is carried out using combined EEG/MEG single dipole scans in the

individually calibrated realistic head volume conductor models. This procedure resulted in an individual dipole target for each subject, localized in Brodmann area 3b in the primary somatosensory cortex SI with predominantly tangential orientation. The P20/N20 somatosensory dipole targets are reconstructed from combined MEG/EEG shown exemplarily (in black) for subject S1 in Figure 3.3(c) and (d) and Figure 3.4(c) and (d).

### 3.7.3 Individual parameter identification study for D-CMI

As this study is the first to present D-CMI optimization, an individual parameter identification study was performed for both the regularization parameter  $\lambda$  and  $S_{\text{maxelec}}$  to test their sensitivity to the overall result and identify their best individual choice for later comparison with the competing methods.

#### 3.7.3.1 Parameter investigation for a single subject

D-CMI( $S_{\text{maxelec}} = 1.5 \text{ mA}, \lambda$ ): First  $S_{\text{maxelec}}$  is fixed to 1.5 mA, as this value was found to be overall the most tolerant limit for the subjects without feeling discomfort when using the Starstim-8 system. It should be noted that skin sensations increased in the preliminary experiments when two close-by electrodes both carried a 1 mA current e.g. when  $S_{\text{maxelec}}$  was set to 1 mA, which should thus be avoided. It, therefore, doesn't seem sufficient to only control the maximum current per electrode when trying to minimize skin sensations, even if this parameter is one of the most important, but a better distribution over more electrodes also seems valuable. A range between 0 and 2000 for the energy penalization parameter  $\lambda$  is examined. As the goal was the utilization of 8 tDCS electrodes, the  $\lambda$  is selected for which the D-CMI( $S_{\text{maxelec}} = 1.5 \text{ mA}, \lambda$ ) mainly results in 8 active electrodes already in the first optimization step, as shown in Figure 3.4(a), (b), and (d) exemplary for subject S1. The  $\lambda$  that produces an 8 electrode montage for each subject is named as individualized  $\lambda_{\text{ind}}$ . Figure 3.4(a) shows that, when increasing  $\lambda$  (x-axis), the directionality metric DIR (y-axis) for the optimized currents in the P20/N20 target area is quite robust and that, as shown in Figure 3.4(b), with increasing  $\lambda$  (x-axis), the currents are distributed over more and more electrodes (y-axis). For  $\lambda = 0$  (no regularization, resulting in 4 active electrodes), the resulting directionality DIR is only 6.04 % higher than for  $\lambda = 860$  (the regularization value that results in 8 active electrodes for subject S1), see Figure 3.4(a), while the number of active tDCS electrodes increases from 4 to 8 (Figure 3.4(b)). The two optimized montages for  $\lambda = 0$  and  $\lambda = 860$  are visualized together with the head model and the target in Figure 3.4(c) and (d), respectively.

For D-CMI( $S_{\text{maxelec}} = 1.5 \text{ mA}, \lambda_{\text{ind}} = 860$ ) (8 electrodes), the 2 mA total current is spread over three anodes with a maximum current of 0.9 mA injected at electrode CP5 (Figure 3.4(d)), while only two anodes are used for D-CMI( $S_{\text{maxelec}} = 1.5 \text{ mA}, \lambda = 0$ ) = CMI( $S_{\text{maxelec}} = 1.5 \text{ mA}$ ) (4 electrodes), with a maximum of 1.5 mA at electrode CP5, which together leads to a considerable reduction in related sensations at the skin level such as tingling

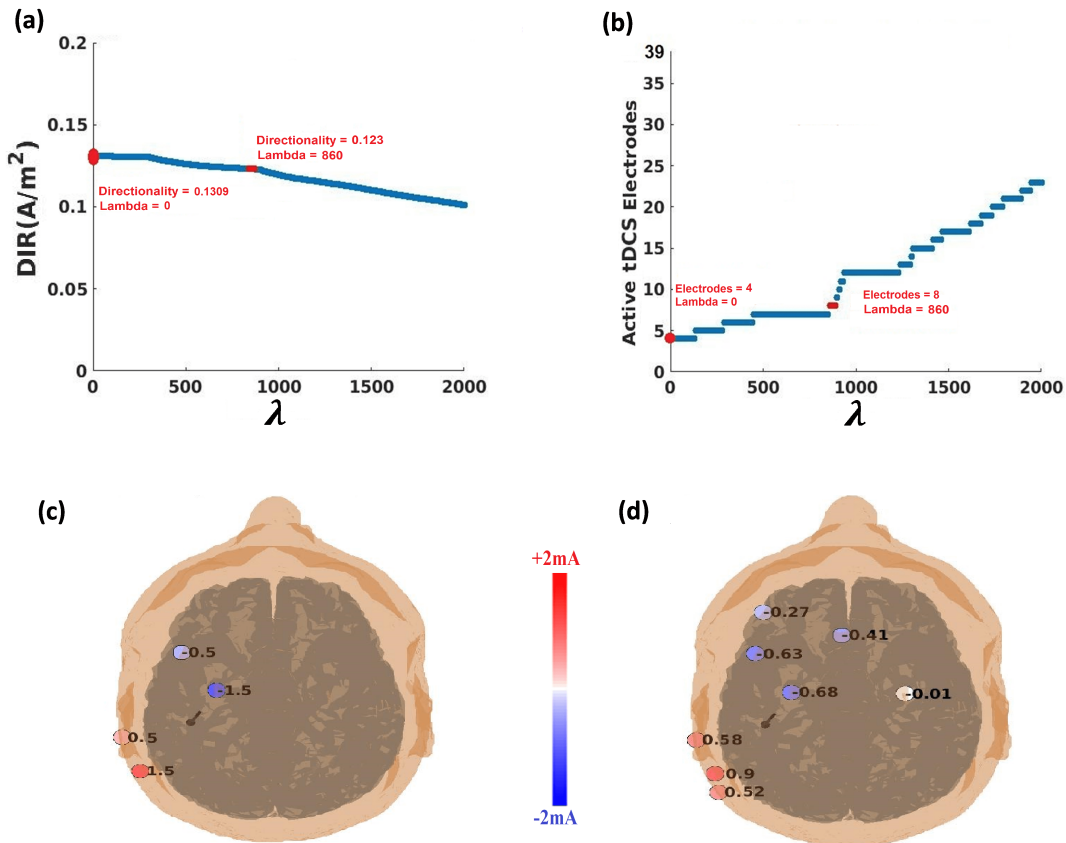


FIGURE 3.4: Distributed constrained maximum intensity (D-CMI( $S_{\text{maxelec}} = 1.5 \text{ mA}, \lambda$ )) approach for subject S1. (a) Directionality (DIR) over  $\lambda$  (b) Number of active electrodes over  $\lambda$  (c) D-CMI( $S_{\text{maxelec}} = 1.5 \text{ mA}, \lambda = 0$ ) montage (d) D-CMI( $S_{\text{maxelec}} = 1.5 \text{ mA}, \lambda_{\text{ind}} = 860$ ) montage.

or pain. This is especially also the case for the cathodes, which are even spreaded over 5 electrodes in D-CMI( $S_{\text{maxelec}} = 1.5 \text{ mA}$ ,  $\lambda_{\text{ind}} = 860$ ), three of them more distant, when compared to the only 2 cathodes in CMI( $S_{\text{maxelec}} = 1.5 \text{ mA}$ ).

### 3.7.3.2 Parameter investigation for a group of subjects

Figure 3.5 shows the  $\lambda$  investigation for all subjects using descriptive statistics with boxplots in (a), (b), and (d) [217]. Figure 3.5(a) shows relationship between active tDCS electrodes (x-axis) and the necessary  $\lambda$  to achieve it (y-axis) and in Figure 3.5(b) the relationship between active tDCS electrodes (x-axis) and the resulting DIR (y-axis) for the 10 subjects. While a higher number of active tDCS electrodes requires a higher  $\lambda$  (Figure 3.5(a)), the DIR measure decreases only minimally as the number of electrodes increases (Figure 3.5(b)). This observation can also be complemented by Figure 3.5(c), where the minimal decrease for DIR is shown for an increasing  $\lambda$ . Figure 3.5(d) shows the two boxplots for the DIR of D-CMI( $S_{\text{maxelec}} = 1.5 \text{ mA}$ ,  $\lambda = 0$ ) = CMI( $S_{\text{maxelec}} = 1.5 \text{ mA}$ ), resulting in 4 active electrodes, and D-CMI( $S_{\text{maxelec}} = 1.5 \text{ mA}$ ,  $\lambda_{\text{ind}}$ ), where  $\lambda_{\text{ind}}$  individually varies for each subject, resulting in 8 active electrodes. The boxplot shows that the average difference is only 3 percent, with a maximum of less than 6 percent.

D-CMI( $S_{\text{maxelec}}$ ,  $\lambda = 0$ ) = CMI( $S_{\text{maxelec}}$ ): In the second investigation,  $\lambda = 0$  fixed and investigated  $S_{\text{maxelec}}$ , i.e., the maximum current per electrode, a parameter, which gives us another possibility to increase the number of non-zero stimulation electrodes with decreasing value of  $S_{\text{maxelec}}$ . The most interesting is to compute CMI( $S_{\text{maxelec}} = 0.5$ ), resulting in 8 active stimulation electrodes, and compare it with the 8 electrode that resulted from D-CMI( $S_{\text{maxelec}} = 1.5 \text{ mA}$ ,  $\lambda_{\text{ind}}$ ) for each subject.

As Figure 3.6 shows, the 8 electrode D-CMI( $S_{\text{maxelec}} = 1.5 \text{ mA}$ ,  $\lambda_{\text{ind}}$ ), achieves on average a 10 percent higher DIR (mean) than the corresponding CMI( $S_{\text{maxelec}} = 0.5 \text{ mA}$ ) approach. Importantly, because CMI( $S_{\text{maxelec}} = 0.5 \text{ mA}$ ) often leads to multiple closeby electrodes of the maximal 0.5 mA strength, the overall skin level sensations in the experimental tests was quite similar to the competing D-CMI approach, even if the maximal current per electrode for D-CMI( $S_{\text{maxelec}} = 1.5 \text{ mA}$ ,  $\lambda_{\text{ind}}$ ) was often slightly higher. It should be noted that skin level sensation differences are individual and for the subjects difficult to grasp and that the described differences between D-CMI and CMI with regard to both DIR and skin level sensations are relatively small. In summary, individual parameter identification in combination with the preliminary experiments on skin level sensations showed that three arguments are slightly in favor of the D-CMI approach when compared to CMI, namely the slightly higher DIR metric for comparable skin level sensations, the stronger distribution of more distant (with regard to the target) electrodes as well as the additional convexity that is added to the optimization functional by the additional energy penalization term (see also the discussion about the elastic net for ADMM in [15]). Therefore, the D-CMI approach with

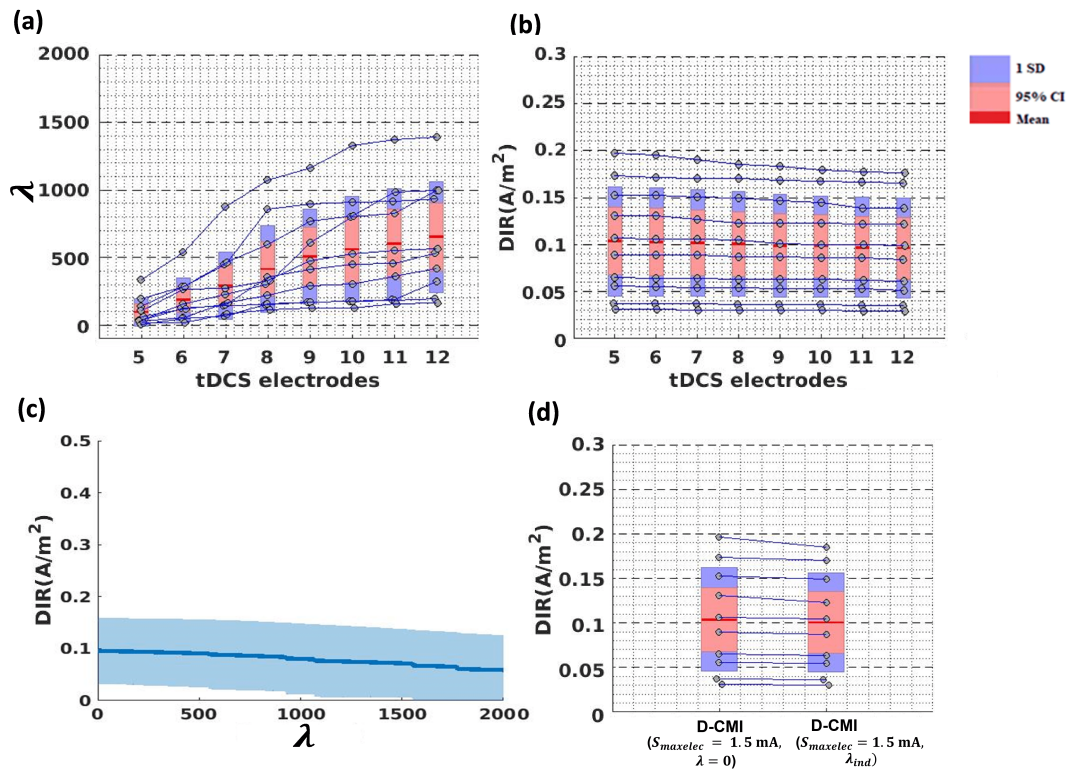


FIGURE 3.5: Relationship between  $\lambda$  (0–2000), number of tDCS electrodes and directionality (DIR) for distributed constrained maximum intensity (D-CMI ( $S_{maxelec} = 1.5 \text{ mA}, \lambda_{ind}$ )) with the legend showing the characteristics of boxplots (10 subjects, grey dots) as mean (red line), 95% confidence interval (95% CI) (pink) and 1 standard deviation (1 SD) (blue). (a) Relation between the number of active tDCS electrodes and the required  $k$  to have current over them. (b) DIR over the number of active electrodes. (c) Effect of  $\lambda$  (0–2000) on DIR with mean (blue line) and standard deviation (light blue shaded area) (d) Comparison of DIR boxplots (10 subjects) between D-CMI( $S_{maxelec}, \lambda = 0$ ) (4 active electrodes) and D-CMI( $S_{maxelec} = 1.5 \text{ mA}, \lambda_{ind}$ ) (8 active electrodes)

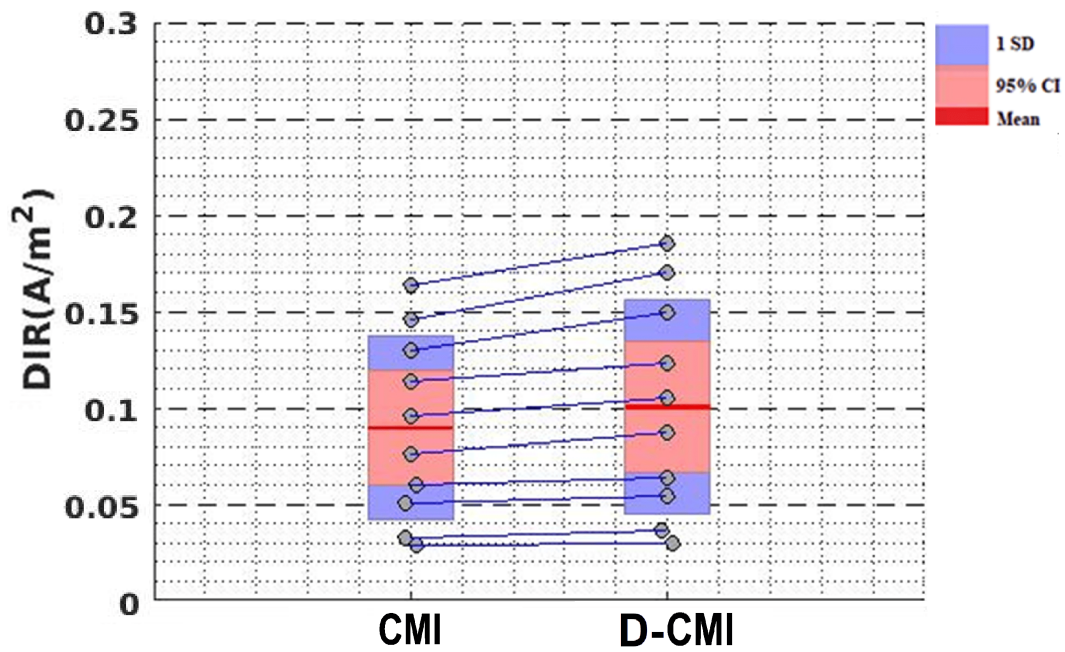


FIGURE 3.6: Directionality (DIR) boxplots (10 subjects) for the two approaches constrained maximum intensity (CMI( $S_{\text{maxelec}} = 1.5 \text{ mA}$ ) with 8 active electrodes and for Distribute constrained maximum intensity (D-CMI( $S_{\text{maxelec}} = 1.5 \text{ mA}, \lambda_{\text{ind}}$ )) with 8 active electrodes. The legend shows the characteristics of boxplots (10 subjects, grey dots) as mean (red line), 95% confidence interval (95% CI) (pink) and 1 standard deviation (1 SD) (blue).

$S_{\text{maxelec}} = 1.5$  mA and a subject-wise individualized  $\lambda := \lambda_{\text{ind}}$  value to distribute the total current over the available 8 stimulation electrodes out of the 39 possible ones in the neoprene cap is used in the following and in the follow-up SEF/mc-tDCS/SEF experiment.

### 3.7.4 Comparison of the tDCS methods

In the subsequent investigations, a comparison is made for the different proposed optimization methods, first of all between each other, and then also in comparison to the standard 2-Patch approach.

#### 3.7.4.1 Visual analysis

In Figure 3.7, a comparison is shown for the optimized and individualized montages of ADMM (upper row), MI (middle row), and D-CMI (lower row) for three (S1, S2, S3) of the ten subjects, targeted to the individually reconstructed somatosensory P20/N20 SI source (in black). The strength of each anodic and cathodic current is indicated, and additionally color-coded in red and blue, respectively. ADMM (first row) leads to a rather irregular distribution of anodic and cathodic stimulation electrodes. The main anodic electrodes are over the left posterior (CP5 or C3) and the main cathodes over the left fronto-central regions (FC1, C1). Main electrodes are often surrounded by electrodes with opposite polarity to improve focality and reduce the intensity in non-target regions. The differences between the subjects are considerable and the maximum current for ADMM in Figure 3.7 is 1.54 mA (S3) and, over all subjects, 1.76 mA (not shown here). Due to the L1 norm side-constraint, the MI approach (second row), results in an optimized bipolar montage with only one anode that carries the total injection current of 2 mA, and one corresponding cathode (-2 mA). The distances between the anode and cathode are larger than in the ADMM result (obviously for S2 and S3, but also for S1 when considering that the main cathodes in ADMM are between FC1 and C1, while MI only uses FZ). The chosen electrode positions are considerably different between the subjects.

The individualized D-CMI ( $S_{\text{maxelec}} = 1.5$  mA,  $\lambda_{\text{ind}}$ ), now also abbreviated as D-CMI, is comparable to the MI result, using mostly the same main electrodes, with the exception of the main cathode for subject S3. An important difference is that D-CMI currents are distributed over multiple neighboring electrodes so that the maximum used current is below  $S_{\text{maxelec}} = 1.5$  mA, which is in Figure 3.7 even only reached for the main anode for subject S3, while the absolute values of all other electrodes are even far below this limit. Especially interesting is that D-CMI in subject S3 distributes over five more distant (with regard to the target) cathodes and reduces the stimulation current from -2 mA in MI to -0.66 mA in D-CMI. ADMM and D-CMI thus use all 8 available Starstim-8 stimulation electrodes and currents with lower amplitude than MI, which only uses 2 of them combined with higher injection currents, resulting in higher sensations at the skin level in the preliminary experiments.

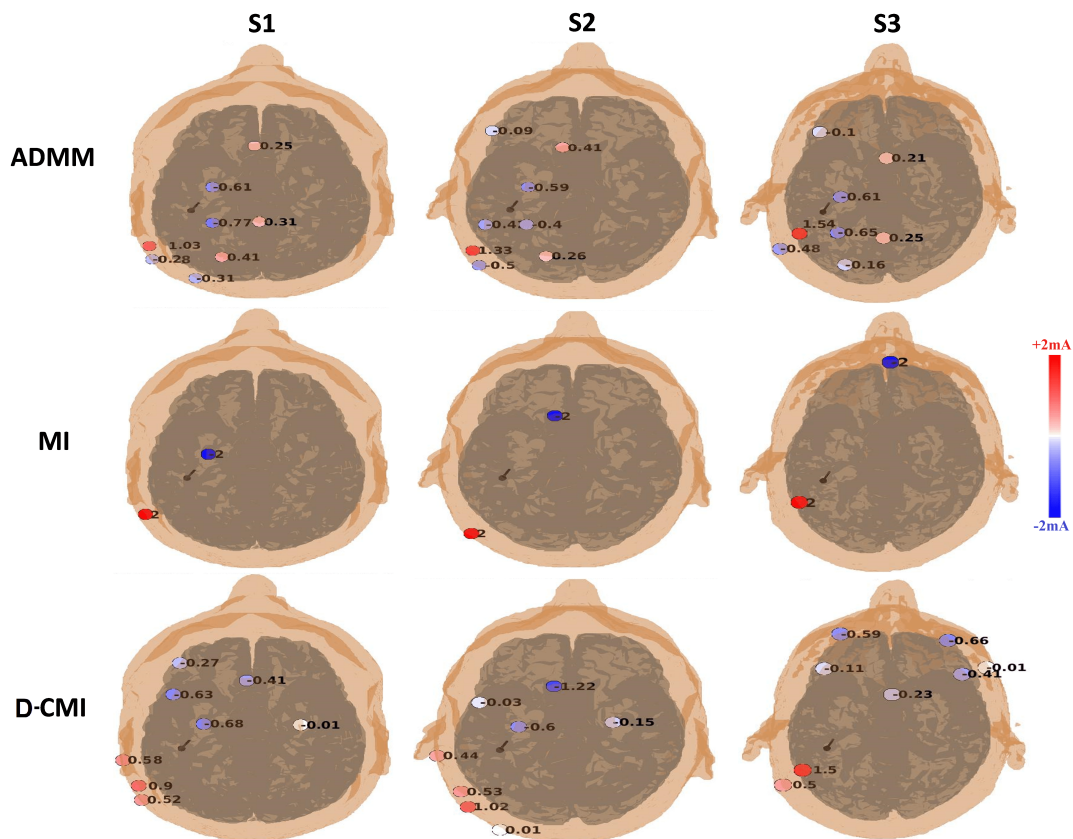


FIGURE 3.7: Optimized montages the alternating direction method of multipliers (ADMM), maximum intensity (MI) and distributed constrained maximum intensity (D-CMI) as  $D-CMI(S_{\maxelec} = 1.5 \text{ mA}, \lambda_{ind})$  for three different subjects (S1, S2 and S3). The montages have been optimized according to the individual location and orientation of the reconstructed P20/N20 target (black dipole).

In the next investigation, the individualized and optimized montages with the non-individualized standard 2-Patch approach will be compared. Visual analysis of the resulting current vector fields in the brain will also be conducted.

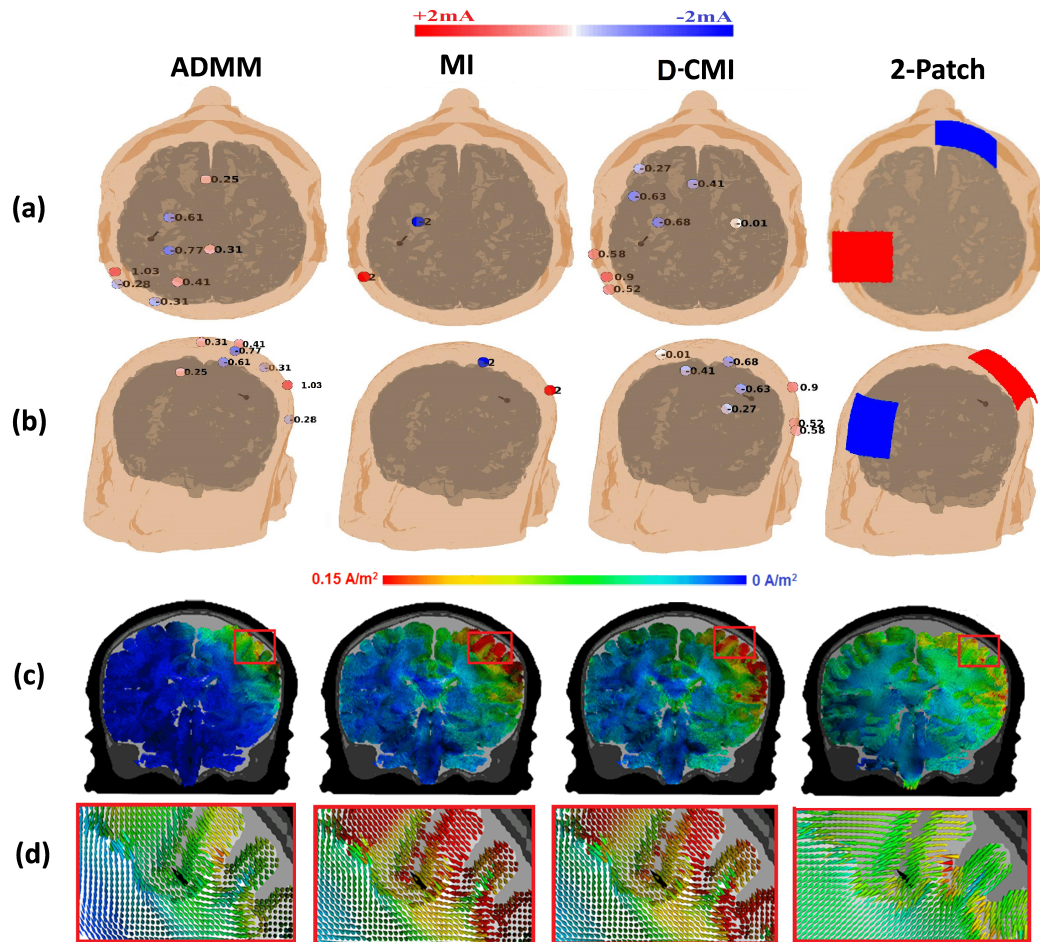


FIGURE 3.8: Current density distributions and montages for the different stimulation approaches for subject S1. From right to left column the approaches are alternating direction method of multipliers (ADMM), maximum intensity (MI), distributed constrained maximum intensity (D-CMI) as  $D-CMI(S_{\maxelec} = 1.5 \text{ mA}, \lambda_{\text{ind}})$  and 2-Patch. Simulated montages with stimulation currents on tDCS electrodes (ADMM, D-CMI and MI) and patches (2-Patch) in (a) top and (b) frontal view for the four tDCS methods are shown. Current distributions for the four methods in the whole brain in (c) and in (d) a zoomed view of the red box (in (c)) showing current density vectors orientation to the SI target (black dipole).

In Figure 3.8, exemplarily for subject S1, the results of the ADMM (first column), MI (second column),  $D-CMI := D-CMI(S_{\maxelec} = 1.5 \text{ mA}, \lambda_{\text{ind}})$  (third column) and 2-Patch standard approach (fourth column), together with the individualized target (in black) were shown. The stimulation montages of all approaches are presented in top (Figure 3.8(a)) and frontal view (Figure 3.8(b)). Figure 3.8(c) and (d) shows the resulting current vector fields in the brain in a full view over the coronal slice through the target (c) and in a

zoomed view at the target side (d). Most importantly, Figure 3.8(c) clearly shows that MI and D-CMI reach much higher target intensities than ADMM and 2-Patch, while ADMM outperforms all other approaches with regard to focality, as the intensity in non-target areas is overall much lower. As shown in Figure 3.8(d), the individually optimized montages reach high directionality of the injected current vector fields to the target area, while this is not the case for the non-individualized 2-Patch approach. All methods do not produce maximal current vector field amplitudes at the (deeper sulcal) target side, but at more lateral gyral crown areas that are closer to the stimulation electrodes (Figure 3.8(c) and (d)).

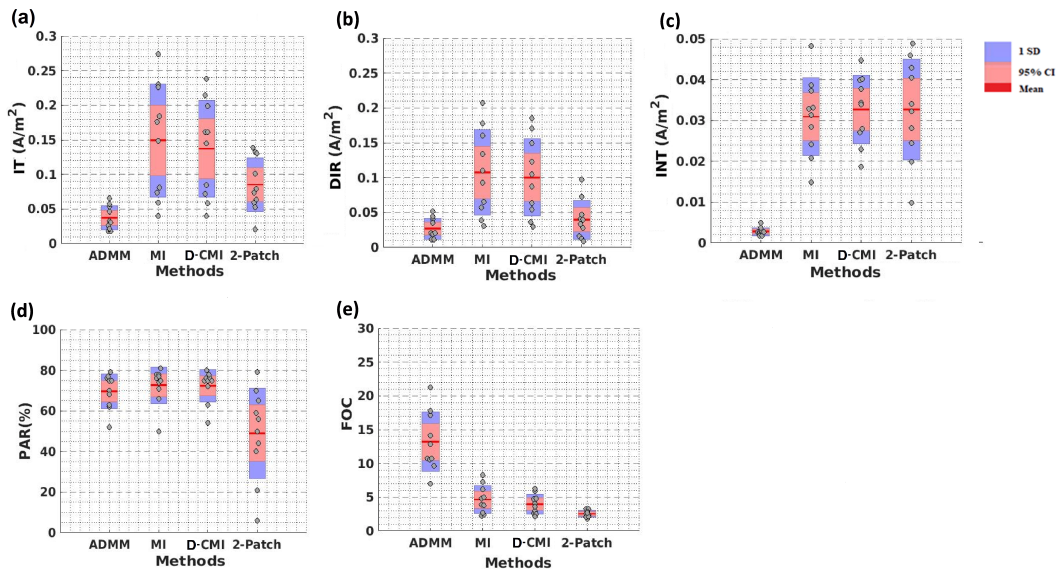


FIGURE 3.9: Performance of alternating direction method of multipliers (ADMM), maximum intensity (MI), distributed constrained maximum intensity (D-CMI) as D-CMI ( $S_{\maxelec} = 1.5 \text{ mA}$ ,  $\lambda_{ind}$ ) and 2-Patch approach (x-axes) with regard to the following metrics (y-axes). (a) IT (average current intensity in target region) (b) DIR (directionality) (c) INT (average current intensity in non-target region) (d) PAR (Parallellity) (e) FOC (Focality). The legend showing the characteristics of boxplots (10 subjects, grey dots) as mean (red line), 95% confidence interval (95% CI) (pink) and 1 standard deviation (1 SD) (blue).

### 3.7.4.2 Statistical analysis

Finally, Figure 3.9 complements Figure 3.8 by showing on the x-axes the four different methods and on the y-axes the boxplots from the results of all ten subjects for the metrics IT (a), DIR (b), INT (c), PAR (d) and FOC (e).

The boxplots in Figure 3.9 together with Table 3.1 and Table 3.2, showing mean and standard deviation and statistical analysis results for the examined tDCS methods and quantification metrics, have the goal to strengthen the last statements that could already visually be perceived from the current vector fields for subject S1 in Figure 3.8(c) and (d), but now using the defined

metrics and in a statistic over all subjects. The effect of the induced electric fields on the dipole target region from the four tDCS methods (ADMM, MI, D-CMI and 2-Patch) was evaluated by employing a one way repeated measures ANOVA (analysis of variance) on the quantification metrics (IT, DIR, INT, PAR and FOC) separately as shown in Table 3.1 column 6. When necessary the Greenhouse-Geisser correction was used to correct for non-sphericity. Post-hoc paired sample t-tests were then performed to compare for multiple comparisons between the tDCS methods for each quantification metric separately as showed in Table 3.2. A P-value of less than 0.05 was considered significant for all statistical analyses.

A highly statistical significant effect resulted from ANOVA among the methods ADMM, MI, D-CMI and 2-Patch for the quantification metrics IT ( $F(3,27) = 18.968$ ,  $p < .001$ ), DIR ( $F(3, 27) = 19.028$ ,  $p < .001$ ), INT ( $F(3, 27) = 39.072$ ,  $p < .001$ ), and FOC ( $F(3, 27) = 60.153$ ,  $p < .001$ ). For the quantification metric PAR ( $F(3,16) = 6.676$ ,  $p = .021$ ) only a moderate statistically significant effect resulted. Figure 3.9(a) and Table 3.1 clearly show that the highest target intensity IT is achieved with the MI and D-CMI:= D-CMI( $S_{\max\text{elec}} = 1.5 \text{ mA}$ ,  $\lambda_{\text{ind}}$ ) approaches, with only a small advantage for MI (mean of  $0.15 \text{ A/m}^2$  for MI versus  $0.14 \text{ A/m}^2$  for D-CMI), while 2-Patch and ADMM only achieve means of  $0.09 \text{ A/m}^2$  and  $0.04 \text{ A/m}^2$ , respectively.

TABLE 3.1: Results of a one-way repeated measures ANOVA (analysis of variance) showing mean and standard deviation (mean  $\pm$  SD) for the four methods, ADMM (Alternating direction method of multipliers), MI (Maximum intensity), D-CMI (Distributed constrained maximum intensity) and 2-Patch and their quantification metrics, IT (Intensity in target), DIR (Directionality), INT (Intensity in non-target), PAR (Parallelity) and FOC (Focality). Column 6 shows the statistical results with degrees of freedom (df), f values (F) and P-values (P) (\* $P < 0.05$ , \*\* $P < 0.001$ ).

Metrics	ADMM (mean $\pm$ SD)	MI (mean $\pm$ SD)	D-CMI (mean $\pm$ SD)	2-Patch (mean $\pm$ SD)	Statistical effect (df, F, P)
IT ( $\text{A/m}^2$ )	$0.04 \pm 0.02$	$0.15 \pm 0.08$	$0.14 \pm 0.07$	$0.09 \pm 0.04$	3, 18.968, $<.001^{**}$
DIR ( $\text{A/m}^2$ )	$0.03 \pm 0.01$	$0.107 \pm 0.061$	$0.10 \pm 0.06$	$0.04 \pm 0.028$	3, 19.028, $<.001^{**}$
INT ( $\text{A/m}^2$ )	$0.003 \pm 1\text{E-}03$	$0.031 \pm 0.01$	$0.033 \pm 0.008$	$0.033 \pm 0.012$	3, 39.072, $<.001^{**}$
PAR (%)	$69.7 \pm 8.54$	$73 \pm 9$	$72.4 \pm 7.9$	$49 \pm 22$	3, 6.676, $.021^*$
FOC	$13.2 \pm 4.379$	$4.66 \pm 2.06$	$3.96 \pm 1.43$	$2.56 \pm 0.48$	3, 60.153, $<.001^{**}$

From the post-hoc t-test for multiple comparisons between the group means as shown in Table 3.2 column 2, it is also evident that for metric IT all comparisons showed statistically significant differences between the tDCS methods accept  $IT_{\text{D-CMI,MI}}$  ( $P = .375$ ). This also indicates that D-CMI and CMI are similarly performing with regard to the IT metric.

Similarly, the highest directionalities DIR are achieved with the MI and D-CMI approaches (mean of  $0.107 \text{ A/m}^2$  for MI and  $0.10 \text{ A/m}^2$  for D-CMI), while 2-Patch and ADMM are at means of only  $0.04 \text{ A/m}^2$  and  $0.03 \text{ A/m}^2$ ,

respectively (Figure 3.9(b) and Table 3.1). Post-hoc t-tests for the methods in DIR, as shown in Table 3.2 column 3, show statistically significant differences for  $DIR_{D-CMI,ADMM}$  ( $P = .001$ )  $DIR_{D-CMI,2-Patch}$  ( $P = .002$ ),  $DIR_{MI,ADMM}$  ( $P = .001$ ),  $DIR_{MI,2-Patch}$  ( $P = .003$ ) and non-significant differences for  $DIR_{D-CMI,MI}$  ( $P = .476$ ) and  $DIR_{ADMM,2-Patch}$  ( $P = .161$ ). The non-significant difference between ADMM and 2-Patch indicate that there is directional similarity between ADMM and 2-Patch.

TABLE 3.2: Results are shown for post-hoc paired-samples t-test statistical comparison between the methods (ADMM, MI, D-CMI and 2-Patch) for their corresponding quantification metrics (IT, DIR, PAR and FOC). (\* $P < 0.05$ , \*\* $P < 0.001$ )

Comparisons	IT(P)	DIR(P)	INT(P)	PAR(P)	FOC(P)
D-CMI,ADMM	<.001**	.001*	<.001**	.182	<.001**
D-CMI,MI	.375	.476	.481	.917	.001*
D-CMI,2-Patch	.010*	.002*	.985	.019*	.373
MI,ADMM	.001*	.001*	<.001**	.388	<.001**
MI,2-Patch	.010*	.003*	.697	.023*	.011*
ADMM,2-Patch	<.001**	.161	<.001**	.038*	<.001**

On the other side, the ADMM results in the lowest intensity in non-target regions, INT, with a mean of only 0.003 A/m<sup>2</sup>, strongly outperforming all other approaches (mean of 0.031 A/m<sup>2</sup>, 0.033 A/m<sup>2</sup> and 0.033 A/m<sup>2</sup> for MI, D-CMI, and 2-Patch, respectively) (Figure 3.9(c) and Table 3.1). It is also shown from the post-hoc t-tests for the INT metric, Table 3.2 column 4, that there are statistically significant differences for  $INT_{D-CMI,ADMM}$  ( $P < .001$ ),  $INT_{MI,ADMM}$  ( $P = .001$ ),  $INT_{ADMM,2-Patch}$  ( $P = .001$ ), indicating that ADMM is a stimulation method optimized for focality compared to the intensity-optimization methods MI and D-CMI and the standard 2-Patch approach.

ADMM therefore also results in the highest focality, FOC, with a mean of 13.2, leaving far behind all other approaches (mean of only 4.66, 3.96, and 2.56 for MI, D-CMI, and 2-Patch, respectively) (Figure 3.9(e) and Table 3.1). Also evident from the post-hoc t-tests for FOC, Table 3.2 column 6, are  $FOC_{D-CMI,ADMM}$  ( $P < .001$ ),  $FOC_{MI,ADMM}$  ( $P < .001$ ),  $FOC_{ADMM,2-Patch}$  ( $P < .001$ ). With regard to parallelity (PAR), while the non-individualized 2-Patch approach is only at about 50 percent with a much larger variability, all individually optimized approaches (ADMM, MI, D-CMI) achieve a mean of about 70 percent, (Figure 3.9(d) and Table 3.1), i.e., their alignment with the P20/N20 SI target orientations is much better. The post-hoc t-tests for PAR, Table 3.2 column 5, also show with  $PAR_{ADMM,2-Patch}$  ( $P = .038$ ),  $PAR_{D-CMI,2-Patch}$  ( $P = .019$ ) and  $PAR_{MI,2-Patch}$  ( $P = .023$ ) statistically significant differences between the standard 2-Patch and the three optimization methods.

Table 3.3 shows the highest injected current on an electrode (anode) for

each subject for the methods D-CMI and ADMM. The highest injected current for MI and 2-Patch are always 2 mA, the reason why they are not presented in the table. As it can be seen the highest injected current among the subjects for D-CMI is 1.5 mA for subjects S3 and S7 and for ADMM it is 1.76 mA for subject S7. Because of the constraint  $S_{\text{maxelec}} = 1.5$  mA for the D-CMI approach, the highest possible injected current cannot exceed 1.5 mA, which is not the case for the ADMM.

TABLE 3.3: Maximum injected currents at anodes for D-CMI (distributed constrained maximum intensity) and ADMM (alternating direction method of multipliers) are shown for each subject.

Subjects	D-CMI (mA)	ADMM (mA)
S1	0.9	1.03
S2	1.02	1.33
S3	1.5	1.54
S4	1.43	1.242
S5	0.94	0.994
S6	1.47	1.074
S7	1.5	1.764
S8	0.95	1.346
S9	0.83	1.211
S10	1.19	0.892

## 3.8 Discussion

### 3.8.1 Targeted mc-tDCS using MEG/EEG source analysis

In this preparation study for a future somatosensory SEF/mc-tDCS/SEF experiment, reconstruction of the underlying SI sources of the somatosensory P20/N20 components was conducted in a group of 10 healthy subjects. A simulation pipeline was performed with individualized target locations and orientations using combined somatosensory evoked field (SEF) and potential (SEP) MEG/EEG data and skull conductivity calibrated realistic six-compartment head modeling with integrated WM conductivity anisotropy. While the SEP P20/N20 component might at least in some subjects have an overlaid thalamic potential additionally to the main Brodmann area 3b contribution, the MEG signal at 20 ms post-stimulus is not affected by such too deep and too radial thalamic sources [110], [120], [182], [194], [195], [207]–[210]. The P20/N20 reconstruction and skull conductivity calibration using combined EEG/MEG, therefore, uses the MEG for the localization of the individual Brodmann area 3b. At the same time, the EEG is then exploited for the estimation of individual source orientation and for skull conductivity calibration. The experimental goal is thus the stimulation of just a single node of the somatosensory network, which might facilitate the effect evaluations. This is

an important difference when comparing the goal of the targeting and optimization procedure with the reciprocity-based optimization of [218]. Furthermore, in most stimulation studies, targets are usually considered only as location-based targets, i.e., no additional orientation information is used for efficient targeting [70]. The use of the complementary information from EEG and MEG data in combined EEG/MEG source analysis together with the individually calibrated skull conductivity [150], [182] offers the advantage of highlighting the individual differences of the somatosensory P20/N20 SI sources among the subjects. These differences are not only in the target location but also in the target orientation since especially the latter might play an important role and should be taken into account for individual targeting [22], [57], [185]–[187]. It should also be mentioned that single modality MEG or EEG reconstructions can lead to considerable differences when compared to combined MEG/EEG for the reconstruction of the 20 ms SEP or SEF component, as shown by [150]. This study is motivated by Laakso [184], who found a correlation between the modeled field intensity and the tDCS efficacy in a motor evoked potential experiment so that individual optimization might also help to better control and especially improve the individual stimulation outcome [198].

It was then shown to what extent individually optimized mc-tDCS montages improved targeting with regard to important metrics when compared to the non-individualized standard 2-Patch approach. The metrics intensity in the target region (IT), directionality (DIR), intensity in non-target regions (INT), parallelity (PAR) and focality (FOC) were used when compared to the non-individualized standard 2-Patch approach. An improved expected performance with regard to these metrics can give us better control in the future somatosensory stimulation experiment. The maximum intensity (MI) mc-tDCS optimization method [9] was also modified with control over current per electrode [189] by an additional energy penalization term, which was called the distributed constrained maximum intensity (D-CMI) approach, according to the experiment's requirements (reduced discomfort such as tingling, pain, itching, and burning sensations [219], [220] and safe stimulation [177], [221], while keeping nearly highest targeting quality) and hardware-limitations (8 active stimulation electrodes out of 39 possible one's in the neoprene cap). Therefore, the study also provides a guideline for the preparation of a controlled mc-tDCS stimulation before its application in an experiment, taking into account the practically most relevant stimulation parameters.

### **3.8.2 Comparison of stimulation methods and contribution of D-CMI compared to MI and CMI**

While maximum intensity (MI), constrained maximum intensity (CMI) and distributed CMI (D-CMI) are, when considering the intensity-focality scale [9], [13], [14], clearly on the intensity side of the scale with their high IT and DIR metrics, the alternating direction method of multipliers (ADMM) [188] is on the focality side with its high FOC and low INT metrics (Figure 3.8 and 3.9). When compared to the standard 2-Patch approach, since all target

optimization approaches ADMM, MI, CMI and D-CMI take both individual target location and orientation into account, they align their injected current vector field much better to the target orientation, resulting in a considerably higher PAR metric (Figure 3.8 and 3.9). The 2-Patch approach is also largely outperformed by MI and D-CMI with regard to the IT, DIR, and even FOC metric, and by ADMM with regard to FOC and INT (Figure 3.8 and 3.9).

For all approaches, the individualization of the targeting and optimization seems important, as shown in Figure 3.7 by the large differences in the targets and stimulation montages between subjects and in Figure 3.8 and 3.9 by the much better performance of the individualized optimization approaches. Our future somatosensory experiment will consist of a pre-stimulation SEF experiment, followed by an individualized and optimized stimulation of the P20/N20 target in Brodmann area 3b, which is again followed by a post-stimulation SEF experiment. Since it was expected that the intensity optimization approaches MI, CMI and D-CMI should be able to generate the largest difference when comparing pre- and post-stimulation SEF, due to their considerably larger DIR metric (Figure 3.9(b)), the focus was only on the contribution of D-CMI when compared to MI and CMI.

D-CMI is an extension of MI [9] and CMI [189] that controls the current per electrode as also proposed by CMI, but with an additional energy penalization term to further distribute the current over multiple electrodes, i.e., with the goal to minimize skin level sensations and high field amplitudes in distant brain areas from the target side. While keeping the important attributes of MI, most importantly a high DIR (mean DIR of D-CMI is only 6.5 percent smaller than for MI, see Table 3.1), the D-CMI offers maximal flexibility in controlling and reducing the maximal current per electrode (here, with  $S_{\max\text{elec}} = 1.5$  mA, it was reduced by 25 percent when compared to the MI with 2 mA), complemented by the L2-regularization to further distribute the injected currents over the available stimulation electrodes at especially distant sides (in the case: 8 active electrodes of the Starstim-8 system). While the L2 regularization hardly reduces the DIR (Figures 3.4 and 3.5), it reduced tDCS-induced discomforts such as tingling, pain, itching, and burning sensations [219], [220] in the preliminary experiments. It also adds convexity to the optimization function, which can be an important aspect with regard to the uniqueness of the solution, especially in more complicated targeting situations (see Theorem 3.5 in [188]).

It is shown in Figures 3.7 that the D-CMI regularization parameter  $\lambda$  takes care that the distribution further away from the target is automatically larger than the distribution in the proximity of the target. This is especially visible in the D-CMI result for subject S3 in Fig.5, where the remaining radial orientation component of the target vector automatically leads to much less distribution at the proximate anodal electrodes side (only 2 anodes) than at the distant cathodes side (6 cathodes). In the extreme case of a fully radial and lateral target, an increase in lambda thus cannot lead to much distribution directly over the target (the proximate closed end of the “current banana”), while the distribution on the distant side in the contralateral hemisphere will be much bigger (the distant “pealed end of the current banana”). Due to the

regularized and weakened cathodal currents, sensations at the skin level and electric field strength at the brain level in the frontal area will be considerably reduced when compared to MI. In MI, the single -2 mA cathode will lead to significant sensations at the skin level and electric field strength at the brain level also in the frontal area beneath the cathode. In summary, this example shows the power of the new D-CMI approach where only a single additional parameter, the regularization parameter, is used by D-CMI to reduce sensations while keeping nearly the same high target directionality.

Therefore, it was decided to choose the D-CMI( $S_{\text{maxelec}} = 1.5 \text{ mA}, \lambda_{\text{ind}}$ )(8 electrodes) for the future somatosensory SEF/mc-tDCS/SEF experiment. However, it should be noted that the differences are rather small, and skin sensations are furthermore difficult to grasp. Therefore, further experiments with a larger group of subjects are needed, for example, a statistical evaluation if it is easier for the subjects to distinguish D-CMI ( $S_{\text{maxelec}}, \lambda$ ) or D-CMI ( $S_{\text{maxelec}}, \lambda = 0$ ) from sham, where D-CMI ( $S_{\text{maxelec}}, \lambda = 0$ ) is identical to CMI( $S_{\text{maxelec}}$ ). The implementation is flexible; it also allows a parameter adaptation, for example, when anesthetizing the area under the stimulation electrodes to further reduce tDCS-induced discomforts such as tingling, pain, itching, and burning sensations [219], [220]

### 3.8.3 Potential of D-CMI

We believe that the D-CMI method has the potential to improve the effects of transcranial electric stimulation (TES) [177] in general, including, besides tDCS, also transcranial alternating current stimulation (tACS) [198], [222], transcranial random noise stimulation (tRNS) [223], [224] and transcutaneous spinal direct current stimulation (tDCS) [225]. D-CMI could help to better control important experimental parameters and thereby also contribute to better reproducibility of TES results. The high DIR values in the target areas with the D-CMI method should also result in much better focality when only considering normal-to-cortex components instead of the modulus, as presented in Figures 3.7 (c) and (d).

From the results, it was concluded that individually-targeted multi-channel optimized montages together with individualized head modeling should be incorporated in brain stimulation research in order to increase the chance of achieving clearer and more consistent neurophysiological effects, in agreement with recent literature on that topic [10], [184], [226]. As shown for example in [226], stimulation with a multi-channel montage increased the M1 excitability compared to a classical tDCS montage when targeting a single brain ROI. Interestingly, inter-subject variability still persisted in all the mc-tDCS optimization approaches also including D-CMI, even if at least the variation (standard deviation) in parallelity was considerably reduced by ADMM, MI and D-CMI when compared to the standard 2-Patch approach (Figure 3.9(d)). CMI also showed the same inter-subject variability in Figure 3.6. It is expected that part of this variability might be alleviated by the use of a denser electrode array [189], especially an increase in the number of possible electrode positions within the optimization process, whereas this

study was limited to only 39 openings of the neoprene cap. Another part of the variability might be “real”, due to for example a deeper target, a lower skull conductivity, or a thicker CSF compartment of a particular subject. In this case, the pipeline has the potential to predict and thus interpret the inter-subject variability of stimulation effects in the later brain stimulation experiment, as also recently proposed in [222].

An important additional advantage of the D-CMI is to ease the use of an experimental sham condition. By limiting the maximal current per electrode and further distributing injected currents over multiple electrodes, the D-CMI will reduce the number of uncomfortable sensations that can occur beneath the electrodes during stimulation such as tingling, pain, itching, and burning sensations, and thereby reduces the sensation difference to the sham condition. Therefore, the use of D-CMI, or MI or CMI combined with a local anesthetic under the electrodes [219], [220], will facilitate the setup of experiments that involve a sham condition. In this way, possibly complemented by an “Active-Sham” condition as proposed in [227], a controlled and consistent sensation throughout the experiment could be achieved.

# 4 Targeted and individually optimized mc-tDCS experimental stimulation of the somatosensory cortex

## 4.1 Introduction

The sources for the early (20 – 40 ms) SEPs in EEG and SEFs in MEG, the cortical responses to median nerve or finger stimulation, are generally accepted to have strong contributions from the primary sensorimotor cortex S1 contralateral to the side of stimulation [16], [119], [194]. The effect of tDCS on these early and late components were studied in [63], [64], [70], [228] showing inhibitory or excitatory effects depending on stimulation parameters. For example, [70], reported a significant increase (excitatory effect) in amplitudes for the P25/N33, N33/P40 (parietal) and P22/N30 (frontal) SEP components after anodal tDCS was applied over the left motor cortex (M1), while no effect was observed for the P14/N20, N20/P25 (parietal) and N18/P22 (frontal) SEP components. Cathodal tDCS showed no effect on the SEP waveforms in their study. In [63], anodal tDCS over the S1 showed no effect on N20 and N30 component while a significant decrease (inhibitory effect) with cathodal tDCS was observed for the N20 SEP component. In [228] early N20 and P25 SEP components were significantly increased after anodal tDCS was applied over motor association cortex while opposite effects were observed after cathodal tDCS. In an MEG recorded SEF tDCS study [64], anodal tDCS was applied over M1 and S1 separately resulting in an increased effect for P35m and P60m SEF components for M1 and for the P60m SEF component for S1. It is summarized that the effect of tDCS on the SEP and SEF components in the above studies showed inconsistencies. Differences in anodal electrode positions (M1, S1 and motor association cortex) and sizes (1.5cm<sup>2</sup>, 9cm<sup>2</sup>, 18 cm<sup>2</sup>) might be a contributing factor to these inconsistent effects. More importantly when targeting a particular area, e.g. the generator for the P20/N20 SEF and SEP component in Brodmann area 3b, the stimulation with only a standard bipolar montage as studied by [1], [40], [41] might thus be a too unspecific or even an inefficient approach [222]. The traditional bipolar tDCS approach broadly distributes electric fields in the brain which might lead to stimulation of non-target regions rather than

in the target area [9]. It has been shown that the use of the traditional bipolar tDCS approach, in most brain stimulation experiments, leads to inconsistencies [180], intra- [7], and inter-subject variability [8], [44] in stimulation results. The cause of the variability might also be attributed to the lack of consideration of an individualized (subject wise) targeting and to different conductive profiles of head tissues and anatomical and functional differences among subjects [77], [115], [150], [182], [183]. For efficient tDCS targeting, injected currents should not only be maximal in the targeted brain region of interest (ROI), but minimal in non-target regions and oriented parallel to the target for the desired effects [22], [185]–[188], [213]. To address these issues, recently a novel multi-channel tDCS (mc-tDCS) approach was proposed, the distributed constrained maximum intensity (D-CMI) method [213] and also presented in Chapter 3. It was shown by computer simulations that, in comparison to standard bipolar tDCS, D-CMI optimized mc-tDCS achieves significantly higher directionality, i.e., higher electric field strength parallel to the target orientation and a higher mean focality. In experimental work, the former might mean higher effect sizes and the latter reduced side effects. Finally, the larger distribution of surface currents by the D-CMI was assumed to reduce skin sensations and thereby ease the use of sham conditioning. With regard to the importance of high target directionality, first simulation and experimental work already showed that a higher parallelity of the injected electric field with the target orientation can increase effect sizes [22], [57], [185]–[187], [229].

In this chapter, the D-CMI approach, for the first time, is tested in an experimental somatosensory paradigm. Focus on anodal stimulation is given to keep the number of measurement sessions to a reasonable limit for the subjects (here: 4 measurement sessions per subject, the first EEG/MEG/MRI for targeting, followed by three MEG/tDCS/MEG stimulation sessions). The D-CMI mc-tDCS approach [213] is compared with a standard bipolar anodal tDCS (SB) and sham tDCS (Sham) approaches. The experimental study is conducted using a single blind experimental tDCS paradigm with three sessions. The experimental study is divided into two parts, targeting and stimulation. In the targeting part, the underlying source of the P20/N20 component in Brodmann area 3b by combined EEG/MEG/MRI is reconstructed through source analysis. After reconstructing this target source individually for each subject, an individualized mc-tDCS montage using D-CMI approach is created for each subject. In the stimulation part of the experiment, three stimulation sessions with the individually optimized anodal D-CMI mc-tDCS (D-CMI), standard bipolar anodal tDCS (SB) and sham stimulation (Sham) are carried out in an SEF/tDCS/SEF paradigm. SEF elicited by electrical index finger stimulation are recorded before and after tDCS interventions in the three randomized tDCS sessions. The after effects for each tDCS condition are statistically analysed and compared. The 20 ms somatosensory component is referred as P20/N20 when recorded with combined EEG/MEG (SEP/SEF) or EEG (SEP) and as an M20 component when recorded with MEG alone (SEF) before and after the application of the three tDCS conditions.

The main focus in this study is on the analysis of the 20 ms S1 component because of its exogenous nature [16], [119], good signal-to-noise ratio (SNR) in both EEG and MEG, its overall robustness [230], [231] and in even the extreme case of anesthesia [232]. The goal is to answer the questions if (1) individually optimized mc-tDCS targeting with D-CMI can provide better controlled stimulation effects compared to SB and if (2) D-CMI montage based sham stimulation eases sham conditioning due to its low skin sensations. Throughout this study, the three tDCS stimulation conditions are referred as only D-CMI, SB and Sham for simplicity.

All figures in this chapter were produced with custom MATLAB codes, SCIRun and CURRY 8. Statistical analysis was conducted with SPSS and processing of EEG and MEG data with FieldTrip [233].

## 4.2 Materials and methods

### 4.2.1 Subjects

Thirteen healthy subjects ( $28 \pm 6$  years, 4 Females) participated in this study. The subjects had no history of psychiatric or neurological disorders and had given written informed consent before the experiment. The institution's ethical review board (Ethik Kommission der Ärztekammer Westfalen-Lippe und der WWU) approved all experimental procedures on 2.02.2018 (Ref. No. 2014-156-f-S).

### 4.2.2 Data acquisition for source reconstruction and tDCS targeting

#### 4.2.2.1 MRI data acquisition and registration

MRI datasets for all 13 subjects were acquired as T1w, T2w and DTI data using the same MRI system and scanning parameters as described in Section 3.2.4.

#### 4.2.2.2 SEP and SEF measurement and pre-processing

SEPs and SEFs were simultaneously acquired for all 13 subjects. The EEG/MEG recording system is the same as described in Section 3.2.2. SEP/SEF data were produced by averaging the trails data acquired from the right hand index finger stimulation as described in 3.2.3 for the purposes of this study.

### 4.2.3 Source analysis and tDCS montage simulations

In order to compute individually optimized mc-tDCS montages for the somatosensory experiment, it is important to accurately reconstruct the underlying target source of the P20/N20 S1 component for each subject. This is done here by means of combined EEG/MEG source analysis using the complementary information from the simultaneously measured SEP and SEF

data. Due to the large inter- and intra-subject variability in skull conductivity [3], [182] and the high sensitivity of EEG source analysis to the skull tissue parameter [6], not only realistic subject-specific head volume conductor models are built for each subject, but also each head model is calibrated for individual skull conductivity. This pipeline is the same as used in Chapter 2.

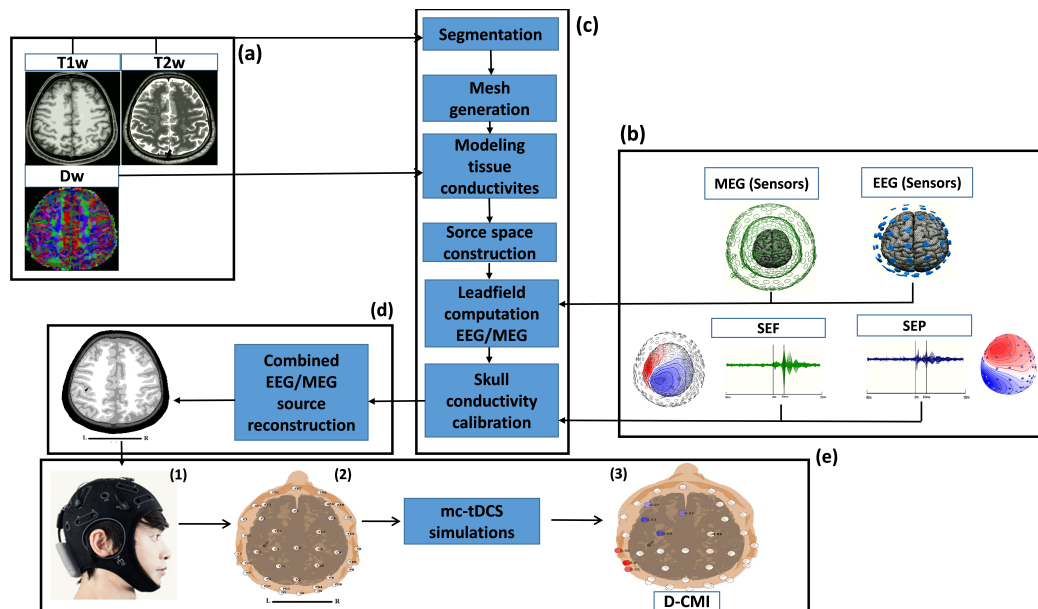


FIGURE 4.1: Schematic diagram of the simulation pipeline for targeting, i.e., reconstructing the P20/N20 activity by means of combined SEP/SEF source analysis, and the following generation of tDCS stimulation montages. (a) MRI data with T1w, T2w and Dw images acquired for modeling (b) MEG and EEG registered sensor locations and SEP and SEF data sets and P20/N20 topographies (c) Forward modeling steps of segmentation, mesh generation, tissue conductivity modeling, source space construction, lead field computations for MEG and EEG and skull conductivity calibration. (d) Targeting by means of a P20/N20 dipole scan (black cone) visualized in the corresponding 6 compartment head model (e) tDCS montage generation steps where (e.1) shows a subject with the Starstim-8 system cap (e.2) the registered and projected electrodes of the Starstim-8 cap on the head model (e.3) the individually targeted and distributed constrained maximum intensity (D-CMI) optimized mc-tDCS montage.

The simulation pipeline in Figure 4.1 shows a schematic diagram that leads to the creation of D-CMI tDCS montages for a P20/N20 S1 target in one of the subjects. Figure 4.1(a) (upper left) the acquired T1w-, T2w- and Dw-MRI data are shown which together with the measured SEP and SEF P20/N20 topographies (Figure 4.1(b)) enable the generation (Figure 4.1(c)) of an individual six-compartment head model (Figure 4.1(d)) with calibrated skull conductivity and anisotropic white matter compartment. This head model serves the EEG/MEG forward computations and enables combined EEG/MEG inverse dipole scanning of the individual P20/N20 target (black cone in Figure 4.1(d)). In the last step, the targeted (to this black cone) and

individually optimized mc-tDCS montage is computed using the D-CMI approach [213] (Figure 4.1(e.3)).

#### 4.2.4 Source reconstruction in calibrated head models

Following the pipeline in Chapter 3 Section 3.2.5 and in Figure 4.1, the source reconstruction procedure for SEP/SEF P20/N20 component at the Brodmann area 3b is described briefly as follows

**Segmentation and meshing:** Segmented realistic head models were created for all 13 subjects. T1w and T2w images were used to segment six tissue compartments with the scalp, skull compacta (SC), skull spongiosa (SS), cerebrospinal fluid (CSF), gray matter (GM), and white matter (WM) to create six tissue compartment models for the subjects. The segmentation process for this study was conducted with the same procedure as described in Section 3.2.5.1

**Mesh model creation:** Meshing of the six compartment segmented head models were carried out using SimBio-VGRID. As already described in 3.2.5.2, hexahedral finite element method (FEM) mesh were created with a node shift of 0.33.

**Modelling tissue conductivities:** Following Section 3.2.5.3, isotropic conductivity of 0.43 S/m for scalp, 1.79 S/m for CSF and 0.33 S/m for GM were set and GM was modeled as anisotropic using Dw images.

**Source space and leadfields creation:** Source spaces confined to GM only and leadfields for EEG/MEG were created using the parameters as previously described in Section 3.2.5.4 and 3.2.5.5 respectively.

**Individualized skull conductivity calibration:** Following the calibration steps in Section 3.2.5.6 the skull conductivity calibration procedure resulted in individual skull conductivities for all 13 subjects with a mean and a standard deviation for SC and SS of  $6.7 \pm 5.12$  mS/m and  $24 \pm 15$  mS/m, respectively.

**Combined EEG/MEG source reconstruction:** Finally, dipole targets with individualized location and orientation were reconstructed for the 13 subjects using the calibrated head models and combined SEP/SEF somatosensory data.

#### 4.2.5 Generation of tDCS montages

For the somatosensory tDCS experiment, two kinds of montages were created, namely the D-CMI [213] and SB [70], [177] montages. The D-CMI resulted in individualized montages for the 13 subjects while the SB was a fixed montage for the subjects. The following steps were conducted, as shown in Figure 4.1(e.1)-(e.3), for the creation of the D-CMI montages:

**Electrode positions projection:** For the creation of the tDCS montages having conformance with the real experimental conditions, first the 39 possible stimulation electrodes (NG Pistim  $\text{cm}^2$  circular contact area) of the Starstim tDCS system (Neuroelectronics, Barcelona, Spain) with a Polhemus device (FASTRAK, Polhemus Incorporated, Colchester, VT) are digitized for

all subjects. For each subject, the locations of the digitized sensors were registered on the head model using landmark-based rigid registration based on the three fiducials nasion, left and right preauricular points, where Gadolinium markers had also been placed for MRI tDCS skull conductivity calibrated FEM forward models were then computed for each subject using SimBio as described in detail in [183].

**tDCS montages creation:** The individualized tDCS forward models were then used by the D-CMI optimization method to find the optimal mc-tDCS montage that best fits the stimulation goal, i.e., targeting the reconstructed individual Brodmann area 3b with the highest directionality (DIR), i.e., highest electric field strength parallel to the reconstructed target source, as well as reduced side effects and skin sensations [213]. The D-CMI method makes use of three parameters,  $S_{\text{Total}}$ ,  $S_{\text{maxelec}}$  and  $\lambda$  [213].  $S_{\text{Total}}$  is the total injected current, which was chosen here as 2 mA.  $S_{\text{maxelec}}$  is the maximum current allowed per electrode, chosen here as 1.5 mA, which was found to be overall the most tolerant limit for the subjects without feeling discomfort when using the Starstim-8 system. The  $\lambda$  parameter distributes the currents over multiple electrodes to reduce skin sensations, which was chosen here in a way that 8 non-zero electrodes resulted due to the availability of electrodes in the Starstim-8 system. In summary, these three parameters are used to create individually optimized montages for each subject while taking into account the dipole target location and orientation. Thus, for each subject an 8-electrode montage was created using the D-CMI method, as illustrated in Figure 4.1(e.3) for one of the subjects. For the SB montage modeling, two 5 cm  $\times$  5 cm quadratic sponge-like tDCS patches with thickness 4 mm [183], [213] and saline-fluid-like conductivity of 1.4 S/m [183] were used. Following the standard montage as used in [70], [177] the patches were centered at the C3 (anode) and FP2 (cathode) electrode locations that were digitized on each subject's head model using the Polhemus device as a fixed montage for induced electric fields simulations [213].

### 4.3 Experimental design

A single blind, randomized, sham-controlled crossover group study with the 13 subjects is conducted to determine the effects of individually targeted and optimized D-CMI mc-tDCS approach, compared to the SB as well as Sham mc-tDCS.

In Figure 4.2, the experimental paradigm with the three stimulation conditions D-CMI (Figure 4.2(a)), SB (Figure 4.2(b)) and Sham (Figure 4.2(c)) as well as the stimulation waveforms for D-CMI (Figure 4.2(e)), SB (Figure 4.2(f)) and Sham (Figure 4.2(g)), exemplarily for one of the subjects are shown. In the tDCS experimental procedure, each subject's SEFs were recorded following right index finger stimulation (green fields in Figure 4.2). The index finger of each subject was stimulated with 2 or 3 times the sensitivity threshold, depending on the subject's sensitivity tolerance. The SEFs were recorded in a run of 10 minutes before tDCS (Pre) and three runs of 10 minutes after tDCS (Post 1, Post 2 and Post 3). After tDCS, participants' heads

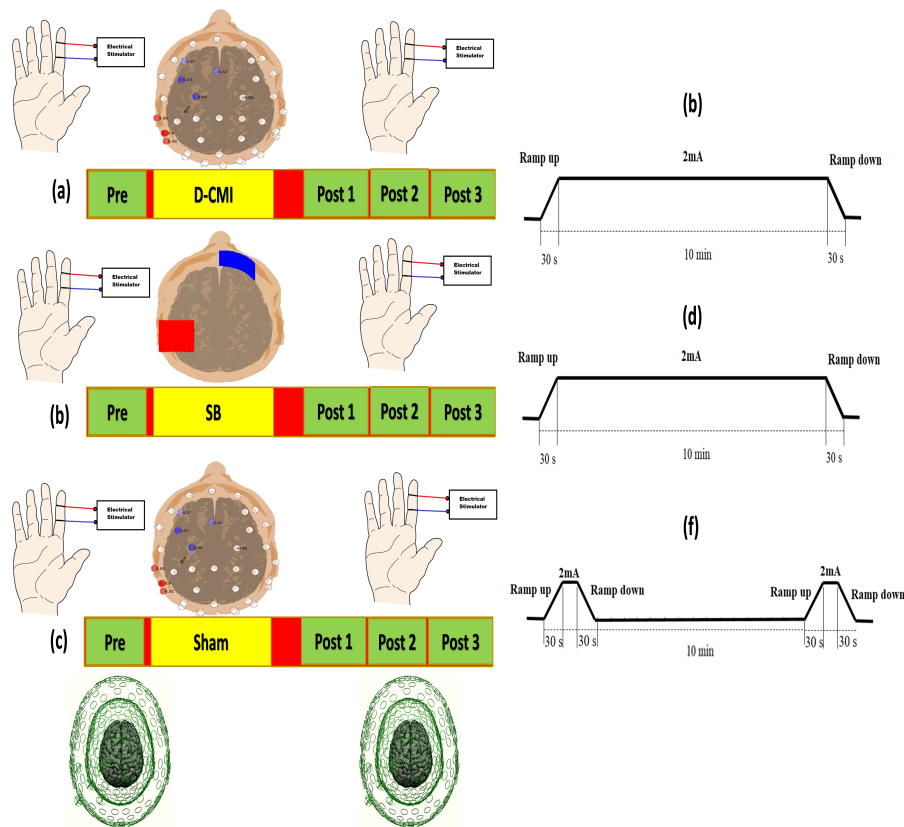


FIGURE 4.2: Experimental design to stimulate the somatosensory S1 with transcranial direct current stimulation (tDCS). Recording of somatosensory evoked fields (SEFs, green fields) before tDCS as Pre (10 min baseline) and after tDCS, with 5 min preparation time (red field), as Post 1 (5-15min), Post 2 (16-26 min), Post 3 (27-37 min). The three different stimulation conditions are (a) distributed constrained maximum intensity tDCS (D-CMI) (b) with 30 s ramp up period, 10 minutes of 2 mA stimulation and ending with 30 s ramp down period (c) standard bipolar tDCS (SB) (d) with 30 s ramp up period, 10 minutes of 2 mA stimulation and ending with 30 s ramp down period (e) D-CMI sham tDCS (sham) (f) with a 30 s ramp up to 2 mA and immediately after a 30 s ramp down period at the beginning and end of stimulation, and with 10 minutes with no stimulation in between.

were briefly cleaned of electrode gel with a towel before re-entering the MEG shielded room (larger red fields in Figure 4.2). Then it was made sure that the right index finger electrical stimulation intensity was the same as in the Pre-tDCS SEF, before then measuring the three runs Post 1, Post 2 and Post 3. All SEFs were recorded in supine positioning due to the arguments given in Section 3.2.3 [199]. The parameters for the recording of SEFs with the MEG system and post-processing were chosen identically to those of Section 3.2.3. Each subject participated in three tDCS conditions of 10 min each, namely D-CMI (upper row in Figure 4.2), standard bipolar (SB, middle row in Figure 4.2) and Sham (lower row in Figure 4.2). Each stimulation condition was embedded in a 10 min SEF recording before (Pre: 10 min baseline) and the three 10 minutes SEF runs after tDCS, i.e., Post 1 (5 -15 min), Post 2 (16 -26

min) and Post 3 (27 -37 min). The sessions were randomized and there was a break of minimally 6 days between the sessions to avoid any interference or carry over effect. In D-CMI and SB conditions, tDCS was applied for 10 min at 2 mA, preceded by a 30 s ramp up period and followed by a 30 s ramp down period at the end of stimulation (Figure 4.2((b) and (d))). In the sham condition, tDCS was realized by delivering the current for 30s ramp up and immediately 30 s ramp down both at the beginning and the end of the 10 minutes of no stimulation (Figure 4.2(f)). The sham protocol was conducted in this way to induce the short-lasting tingling perceived during the transient period of current turn-on and off like in the real stimulations of D-CMI and SB. All tDCS stimulation conditions were carried out with a Starstim-8 tDCS system (Neuroelectronics, Barcelona, Spain), using 3.14 cm<sup>2</sup> Ag/AgCl gelled electrodes placed into holes of a neoprene cap corresponding to the international 10/10 EEG system.

**Questionnaires data:** After each stimulation session, subjects completed a self-reported questionnaire to explore perceptions of adverse or side effects. The questionnaire contained rating scales for the presence and severity of side effects such as itching, pain, burning and warmth/heat sensation [177] on the scalp elicited by the three tDCS conditions (D-CMI, SB and Sham). Numerical analogue scales were used to rate the unpleasantness of sensations on the scalp (e.g. 0 = none, 1 = mild, 2 = moderate and 3 = strong). For each condition, it was also part of the questionnaire, that subjects were asked to speculate whether they were receiving real or sham stimulation to assess the integrity of the subjects' blinding using a numerical analogue rating scale (1 = real, 2 = placebo, 3 = I don't know) [177].

## 4.4 Data analysis

**Source space:** For the analysis of SEFs before and after tDCS conditions, the following steps were first conducted

- Computation of MEG lead fields (forward models), for each subject before and after each tDCS condition (D-CMI, SB and Sham) due to the possibly slightly different subject positioning in the MEG dewar.
- Computation of source waveforms for the M20 component was carried out as described in Chapter 3. Due to the higher signal-to-noise and the complementarity of EEG and MEG, target source of the combined SEP/SEF reconstruction was fixed and projected on the SEF data of the three stimulation conditions under the additional assumption that the expected change in excitability of S1 would not lead to a shift in the source location. The source waveforms for the M20 are then stored for later analysis.
- In the last step, amplitude of the 20ms sample of the M20 source waveforms pre and post (Post 1, Post 2 and Post 3) tDCS conditions (D-CMI, SB and Sham) for each subject are taken for analysis.

After these three steps, a statistical analysis of the M20 sample amplitudes for time courses before (Pre) and after (Post 1, Post 2, Post 3) tDCS conditions (D-CMI, SB and Sham) is performed within subjects (N=9) two way repeated measures analysis of variance (RM-ANOVA).

The analysis was conducted for 9 subjects only as all the 13 subjects did not show consistent quality data throughout the conditions and sessions. Outliers with noisy data were rejected for analysis resulting in 9 subjects for D-CMI (N=9), SB (N=9) and Sham (N=9). Greenhouse-Geisser correction was used for non-sphericity wherever necessary. Post-hoc paired sample t-tests with bootstrapping (1000 permutations) were then performed for multiple comparisons between control values (Pre) and those after tDCS (Post 1, Post 2 and Post 3) for the three conditions (D-CMI, SB and Sham) separately. A P-value of less than 0.05 was considered significant for all statistical analyses.

**Sensor space:** To complement the source space analysis in sensor space, an analysis in the time range of 19 to 21 ms with a non-parametric cluster based permutation test [233] for Pre vs Post (Post 1, Post 2 and Post 3) time course differences for all conditions (D-CMI, SB and Sham) separately is performed. From a dependent paired t-test, for time course comparisons, all samples showing a t-value greater than a threshold corresponding to  $P = 0.05$  (uncorrected) were selected and spatially clustered. The level of the statistics of the cluster was defined as the sum of t-values within the cluster. The cluster with the maximum value was used to construct the statistics. A reference distribution of maximum cluster t-values was obtained by randomization of data across the time courses for each condition separately for 1000 times and was used to evaluate the statistic of the actual data. Questionnaire data: Questionnaire data was analysed for perceived sensations (Itching, Pain, Burning and Warmth/heat), scaling each sensation as 1 = none, 2 = mild, 3 = moderate and 4 = strong, with a non-parametric Friedman ANOVA test for each sensation among the tDCS conditions (DMCI, SB and Sham) separately. A P-value of less than 0.05 was taken as significant. Wilcoxon test was carried out if significant differences were found between conditions (D-CMI, SB and Sham) for each sensation with the Friedman test. Sham perception questionnaire data was also analysed with Friedman ANOVA test with scaling as 1 = real, 2 = placebo, 3 = I don't know among the conditions.

## 4.5 Results

While the bipolar montages are thus only standardized, the D-CMI mc-tDCS montages are largely personalized with regard to head modeling, determination of the target as well as optimization for maximal directionality with reduced side effects and skin sensations. Figure 4.3(a) shows how different the D-CMI montages can be depending on especially individual target orientation differences. Exemplary for three subjects D-CMI montages (Figure 4.3(a), left column) and EEG topographies presented together with the D-CMI montages (Figure 4.3(a), right column) are shown to emphasize the importance of individualized montage calculation.

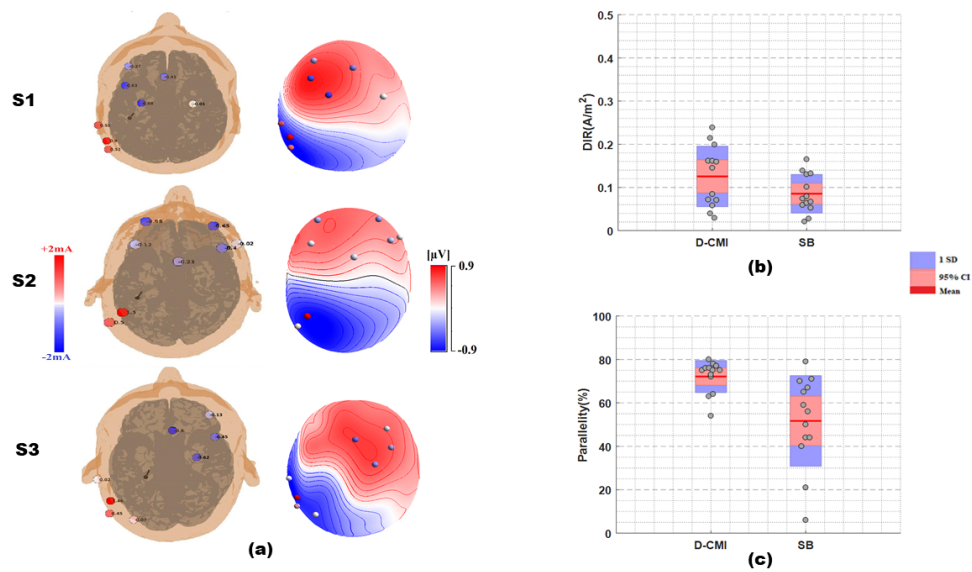


FIGURE 4.3: The results for the D-CMI mc-tDCS method are shown as (a) D-CMI mc-tDCS montages (columns 1) and D-CMI montages projected over the EEG P20/N20 topography (columns 2) exemplary for the three subjects (S1, S2 and S3) (b) directionality (DIR) (N=13) and (c) parallelity (N=13) comparison of D-CMI and SB as boxplots with mean (red line), 95% confidence interval (95% CI) (pink) and 1 standard deviation (1 SD) (blue).

Figure 4.3(b) presents the resulting directionality (DIR) values for the group of 10 subjects with boxplots showing mean (red line), 95% confidence interval (95% CI) (pink) and 1 standard deviation (1 SD) (blue).

The mean  $\pm$  SD DIR for D-CMI ( $0.13 \pm 0.07$  A/m<sup>2</sup>) and SB ( $0.085 \pm 0.04$  A/m<sup>2</sup>) shows that individually targeted mc-tDCS increases the chance for individual stimulation effects when compared to SB. Furthermore, in Figure 4.3(c) also shown is (PAR), i.e. the percentage of current intensity that is oriented parallel to the target vector. This parameter complements DIR and clearly shows that PAR (mean  $\pm$  SD) for D-CMI ( $72 \pm 7\%$ ) is much higher than for SB ( $52 \pm 21\%$ ). It can thus be hypothesized from simulation results that individually targeted and optimized mc-tDCS with D-CMI might reduce individual differences in effects when compared to SB, i.e., it might lead to more controlled tDCS effects.

**Source space results:** Figure 4.4(a) - (c) shows the grand averaged source waveforms (0 to 22 ms) of the M20 SEF component for all subjects with time courses, Pre (Blue), Post 1 (Red dotted), Post 2 (Green dotted) and Post 3 (Black dotted), for the three conditions in Figure 4.4(a) (D-CMI), Figure 4.4(b) (SB) and Figure 4.4(c) (Sham).

Figure 4.5 shows error bar plots with mean (colored boxes) and standard deviation (vertical line) for the grouped peak amplitudes of M20 source waveforms for each time course as Pre (blue box) Post 1 (red box), Post 2 (green box) and Post 3 (black box). Grouped amplitudes for M20 source waveforms after tDCS time courses, Post 1, Post 2 and Post 3 are normalized

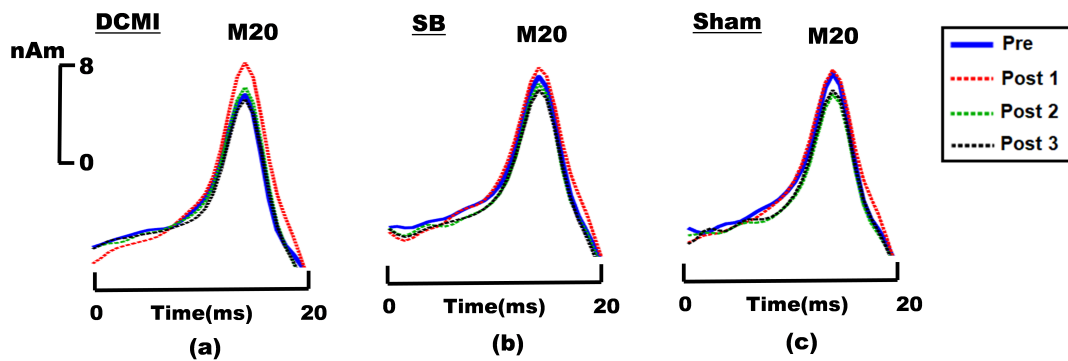


FIGURE 4.4: Grand averaged source waveforms of M20 are shown for before tDCS as Pre (Blue) and after tDCS as Post 1 (Red dotted), Post 2 (Green dotted) and Post 3 (Black dotted). (a) Grand averaged source waveforms for 9 subjects (N=9) when stimulated with distributed constrained maximum intensity (D-CMI) (N=9). (b) Grand averaged source waveforms for 10 subjects (N = 10) when stimulated with standard bipolar tDCS (SB). (c) Grand averaged source waveforms for 12 subjects (N=12) when stimulated with D-CMI sham tDCS (Sham).

to pre tDCS amplitudes (Pre) as baseline normalization. The time courses as coloured boxes for each condition are shown in Figure 4.4(a) (D-CMI), Figure 4.4(b) (standard bipolar (SB)) and Figure 4.4(c) (sham) separately.

Table 4.1 shows mean and standard deviation (Mean(SD)) for each condition's time courses, Table 4.2 shows the interaction effects among the tDCS conditions and Table 4.3 shows the post-hoc paired sample t-test results for Table 4.2. Table 4.3 also shows the Cohen's d effect size for the time course compared to Pre baseline. For the two way RM-ANOVA, significant interaction effects were observed when comparisons were conducted for D-CMI vs SB ( $F(3, 24) = 10.63, P < 0.001$ ) and D-CMI vs Sham ( $F(3, 24) = 3.63, P = 0.027$ ). No significant interaction effects were observed for SB vs Sham ( $F(3, 24) = 0.624, P = 0.606$ ) comparison. A significant interaction effect was observed for all three conditions comparisons also, D-CMI vs SB vs Sham ( $F(2.8, 48) = 3.5, P = .034$ ) Post-hoc paired sample t-test in Table 4.3 for D-CMI revealed a significant main effect for Pre vs Post 1 ( $P = 0.013$ ), non-significant effects for Pre vs Post 2 ( $P = 0.367$ ) and Pre vs Post 3 ( $P = 0.77$ ). A very large to huge effect size ( $d=1.44$ ) was observed for the Pre vs Post 1 in the D-CMI condition while negligible medium and small effects very observed for Pre vs Post 2 and Post 3 D-CMI conditions, respectively. The M20 amplitude for the D-CMI increased on average 33% in the first 5 to 15 minutes (Post 1) (Figure 4.4(a)) after tDCS while it non-significantly increased only 8% in Pre vs Post 2 (Figure 4.4(a)) and decreased by -1% Pre vs Post 3 (Figure 4.4(a)) time course comparison.

Post-hoc paired sample t-test in Table 4.3 for SB revealed non-significant effects for Pre vs Post 1 ( $P = 0.367$ ) and Pre vs Post 2 ( $P = 0.160$ ) and Pre vs Post 3 ( $P = 0.091$ ). Only small to medium decreased effect sizes were observed in all the time courses. The M20 amplitude for SB increased on average 2% non-significantly for Pre vs Post 1 time course and reduced significantly with

TABLE 4.1: The table shows mean and standard deviation (Mean(SD)) of the M20 source waveform amplitude among subjects through the time course including Pre, Post 1, Post 2 and Post 3 in the tDCS conditions of distributed constrained maximum intensity (D-CMI), standard bipolar (SB) and D-CMI sham (Sham) sessions.

Conditions	Mean(SD) in nAm			
	Pre	Post 1	Post 2	Post 3
<b>D-CMI (N=9)</b>	4.63(2.79)	6.01(3.54)	4.95(3.09)	4.53(2.76)
<b>SB (N=9)</b>	4.45(2.75)	4.67(3.26)	4.16(3.05)	4.06(3.03)
<b>Sham (N=9)</b>	4.67(3.33)	4.76(3.93)	4.76(3.93)	4.20(3.76)

TABLE 4.2: Results of a two way repeated measures ANOVA (RM-ANOVA) showing the interaction effect between the tDCS conditions. Column 1 and column 2 shows the statistical results correspondingly, when conditions are compared, with degrees of freedom (df), F values (F) and P-values (P) (\*P < 0.05, \*\*P < 0.01, \*\*\*P < 0.001)

Conditions comparison	Interaction effect (Condition x Time) df, F, P
<b>D-CMI vs SB</b>	3, 10.628, <.001***
<b>D-CMI vs Sham</b>	3, 3.629, 0.027*
<b>SB vs Sham</b>	3, 0.624, 0.606
<b>D-CMI vs SB vs Sham</b>	2.8, 3.5, .034*

TABLE 4.3: M20 source waveform amplitude results are shown for post-hoc paired-samples t-test and Cohen's d effect size for the t-test statistical comparisons separately for the conditions D-CMI, SB and Sham between time courses before tDCS (Pre), as control values, and after tDCS (Post), as Pre vs Post 1, Pre vs Post 2 and Pre vs Post 3. (\*P < 0.05, \*\*P < 0.01, \*\*\*P < 0.001)(d = 0.2(Small effect), 0.5(Medium effect), 0.8 (Large effect))

Paired t-test Comparison	D-CMI (N=9) P, Cohen's d	SB (N=9) P, Cohen's d	Sham (N=9) P, Cohen's d
<b>Pre vs Post 1</b>	0.013*, 1.44	0.367, 0.32	0.77, 0.11
<b>Pre vs Post 2</b>	0.27, 0.45	0.160, 0.52	0.02*, 0.99
<b>Pre vs Post 3</b>	0.73, 0.12	0.091, 0.64	0.24, 0.54

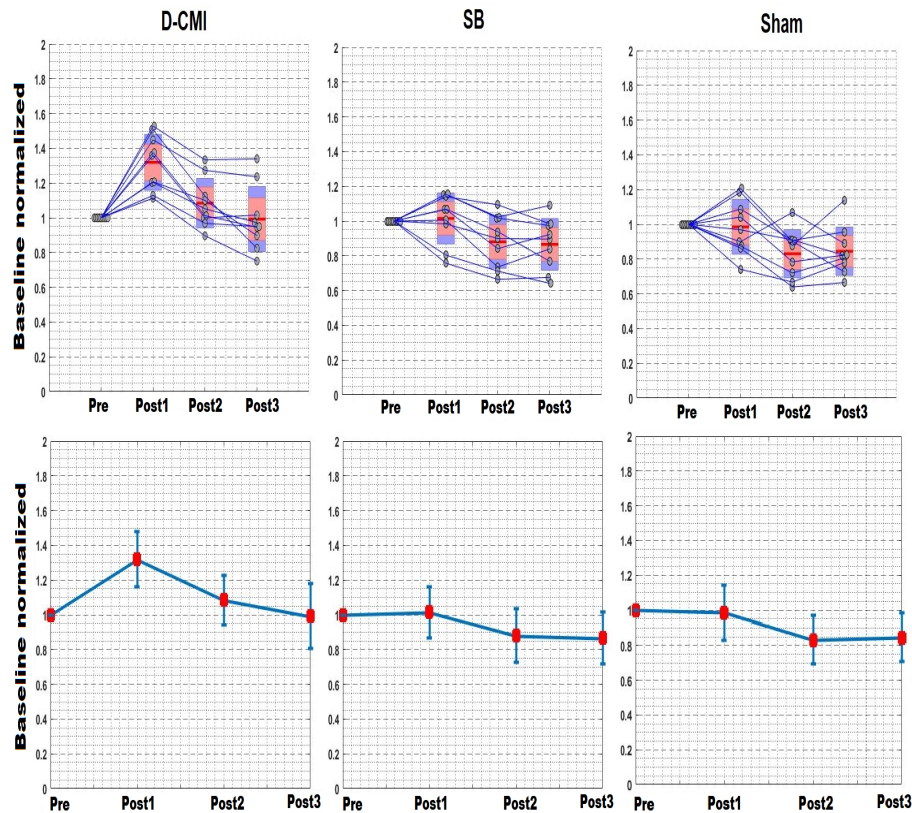


FIGURE 4.5: After effects of the three tDCS stimulation conditions (a) distributed constrained maximum intensity (D-CMI) (b) standard bipolar (SB) and (c) Sham, on the M20 amplitudes of source waveforms though time courses as Post 1, Post 2, Post 3 normalized to before tDCS M20 source waveform amplitudes in Pre. The boxes with error bars represent the standard error of means.

a reduction on average of -12% for Pre vs Post 2 and -11% for Pre vs Post 3.

Post-hoc paired sample t-test in Table 4.3 for Sham showed a non-significant effect for Pre vs Post 1 ( $P = 0.77$ ), a significant effect for Pre vs Post 2 ( $P = 0.02$ ) and a non-significant effect for Pre vs Post 3 ( $P = 0.24$ ). For the Sham condition only the Pre vs Post 2 comparison showed a larger effect size ( $d = 0.9$ ). The M20 amplitude change for Sham was decreased for Pre versus Post 1 with only -1% on average, while it was significantly reduced on average to -17% and -16% for Post 2 and Post 3 time courses, respectively.

**Sensor space results:** Figure 4.6, shows the resultant t-value topographies for non-parametric cluster based permutation tests. Conditions are shown in rows as Figure 4.6(a) for D-CMI, Figure 4.6(b) for standard bipolar (SB) and Figure 4.6(c) for Sham and time course comparison to pre tDCS as columns for Pre vs Post 1 (1), Pre vs Post 2 (2) and Pre vs Post 3 (3).

In the sensor space analysis (Figure 4.6), the non-parametric cluster based permutation test showed similar results to the source space results. For the D-CMI condition, significant clusters were observed for the Pre vs Post 1 time course comparison with negative and positive clusters (Figure 4.6(a.1)). No significant clusters were formed for Pre vs Post 2 (Figure 4.6(a.2)) and Post

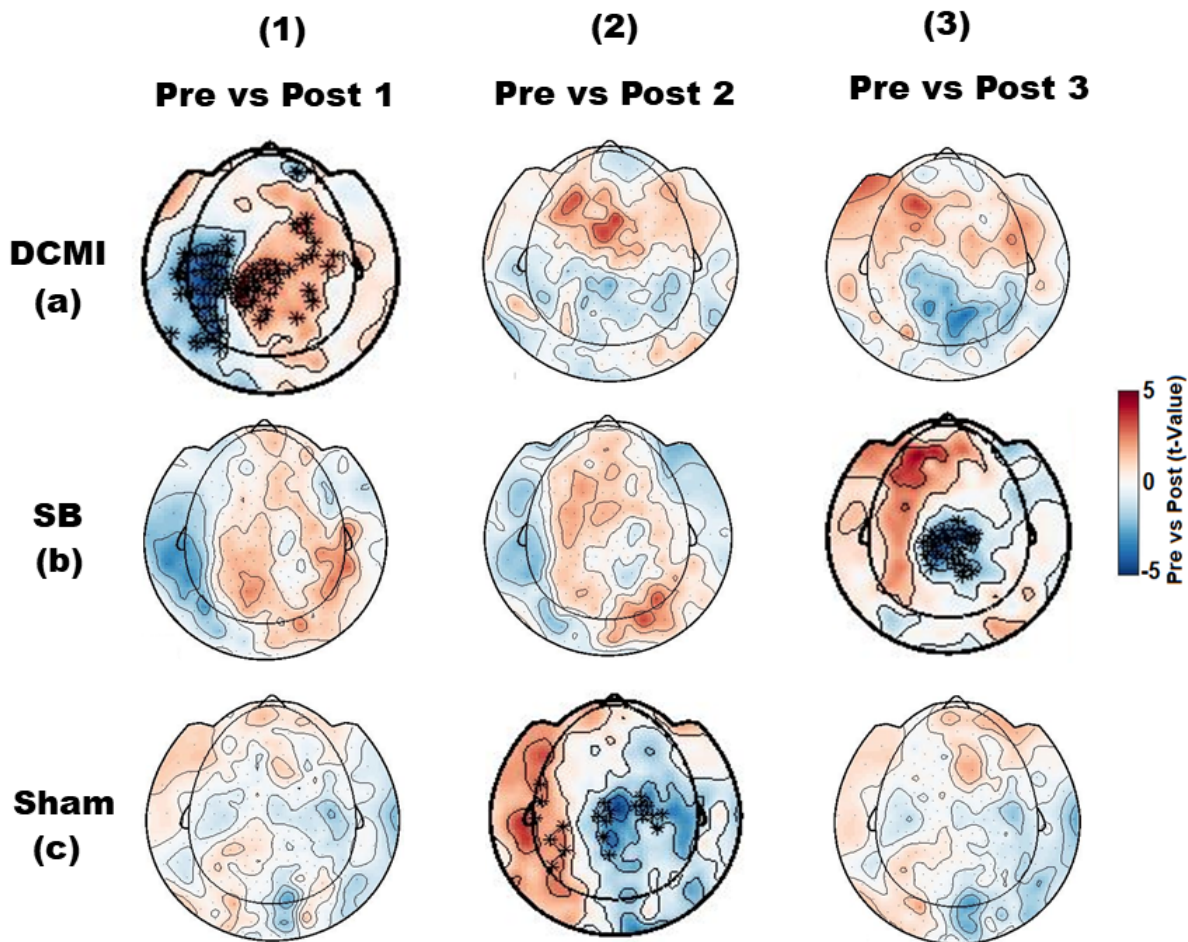


FIGURE 4.6: T-value topography differences resulting from a comparison of the M20 (range 19 to 21 ms) somatosensory evoked fields (SEF) component before and after tDCS with the non-parametric cluster based permutation t-test. Negative (blue) and positive (red) T-value differences are shown between time courses in columns (1) Pre vs Post 1 (2) Pre vs Post 2 (3) Pre vs Post 3 for conditions in rows (a) D-CMI (b) SB and (c) Sham separately. MEG sensors showing significant differences between conditions and time courses in the non-parametric test after randomization are marked by a cross. (\* $P < 0.05$ )

3 (Figure 4.6(a.3)) time course comparison. In the SB session, no significant negative or positive clusters were formed in the Pre vs Post 1 (Figure 4.6(b.1)) and Pre vs Post 2 (Figure 4.6(b.3)), while a significant negative cluster was observed for Pre vs Post 3 (Figure 4.6(b.1)) time course comparison. In the Sham condition, significant positive and negative clusters were observed for the Pre vs Post 2 (Figure 4.6(c.2)) and no significant clusters were observed for the Pre v Post 1 (Figure 4.6(c.1)) and Post 3 (Figure 4.6(c.3)) time course comparison.

**Questionnaire results:** Table 4.4, shows the results of the non-parametric Friedman test applied to the perceived sensation data for each condition separately. Table 4.5 shows the results of the non-parametric Friedman test applied on the sham perception data. All the subjects tolerated the application

TABLE 4.4: Group comparisons on intensity of perceived sensations (Itching, Pain, Burning and Warmth/Heat) separately among the conditions (D-CMI, SB and Sham) with a non-parametric Friedman ANOVA test from the questionnaire of sensations related to transcranial electrical stimulation [177]. Mean and standard deviation (Mean (SD)) of the scaled data are shown for the three conditions (D-CMI, SB and Sham) and each perceived sensation (Itching, Pain, Burning and Warmth/Heat) separately.

Sensations (N=13)	D-CMI (Mean(SD))	SB (Mean(SD))	Sham (Mean(SD))	$\chi^2$ , df, P
<b>Itching</b>	2.08(0.76)	1.85(0.80)	1.69(0.75)	3.16, 2, 0.21
<b>Pain</b>	1.69(0.75)	1.31(0.48)	1.23(0.44)	4.46, 2, 0.11
<b>Burning</b>	1.85(0.98)	1.46(0.48)	1.69(0.51)	4.33, 2, 0.12
<b>Warmth/Heat</b>	1.62(0.65)	1.54(0.66)	1.23(0.43)	3.25, 2, 0.19

of the currents in different conditions very well and there was no disruption of the experimental procedures due to adverse or side effects. Table 4.4 summarizes the mean intensity of the sensations according to the questionnaire for scaled sensations (itching, pain, burning and warmth/heat) on the scalp by the tDCS interventions (D-CMI, SB and Sham). The non-parametric Friedman ANOVA test for each sensation between conditions did not result in any significant group difference among the conditions. No significant differences in the intensity of perceived sensation for itching ( $\chi^2(2) = 3.161$ ,  $P = 0.206$ ), pain ( $\chi^2(2) = 4.45$ ,  $P = 0.108$ ), burning ( $\chi^2(2) = 4.33$ ,  $P = 0.115$ ) and warmth/heat ( $\chi^2(2) = 3.5$ ,  $P = 0.197$ ) was observed.

TABLE 4.5: The judgment of perceived stimulation as real or sham among the subjects for each condition (D-CMI, SB and Sham) separately is shown. Mean and standard deviation (Mean(SD)) is also shown of the scaled data for each stimulation condition separately.

Sensations	D-CMI (N=13)	SB (N=13)	Sham (N=13)	Total
<b>Real</b>	10	7	10	27
<b>Sham</b>	0	6	0	6
<b>I don't know</b>	3	0	3	6
<b>Mean (SD)</b>	1.46(0.84)	1.46(0.49)	1.46(0.84)	

The non-parametric Friedman ANOVA test showed no significant differences for the subject's judgment on sham or real stimulation (D-CMI and SB) ( $\chi^2(2) = 4.45$ ,  $P = 0.108$ ) (Table 4.4). Table 4.5 summarizes the subject's judgement on the stimulation conditions. As can be seen, the majority of the subjects (excluding subjects for "I don't know") in the conditions perceived

the tDCS stimulations as active or real conditions. Supporting the fact the sensation was perceived as the same throughout the conditions and sham blinding was successful.

## 4.6 Discussion

In the presented study, for the first time, the effects were examined of the largely individualized D-CMI targeted and optimized mc-tDCS approach [213] in a brain stimulation experiment. A well-controlled somatosensory setup was used in a group of 13 healthy subjects. The target area was the underlying source of the somatosensory evoked potential (SEP) and field (SEF) P20/N20 component in Brodmann area 3b (S1), elicited by electrical stimulation of the right index finger. Individual targeting has been performed by means of source analysis of the P20/N20 component using the complementary information of combined SEP/SEF data. Source analysis uses individual skull conductivity calibrated six compartment anisotropic finite element method (FEM) head models of the subjects. In the targeting, the strength of MEG is used to determine source location while EEG is exploited for the source moment (i.e., source orientation and strength) as well as for estimation of individual skull conductivity. The generated subject-specific FEM head models were then also used for tDCS forward simulations and optimizations of D-CMI electrode montages. Experimental effects of (i) the individually targeted and optimized D-CMI mc-tDCS (D-CMI), (ii) standard bipolar tDCS (SB) and (iii) sham stimulation (Sham) are then compared. Since D-CMI and SB stimulations of anodal type was used, an excitatory effect is expected when compared to Sham. While [63], [70] used EEG, in this study MEG was used, like in [64], to read out stimulation effects on the P20/N20 (or M20) target by projecting SEF measurements pre- and post- tDCS to the fixed source location and orientation from the targeting process, due to the much higher sensitivity of MEG to the lateral and mainly tangential S1 activity [16], [110], [150].

It was shown that inter-individual differences of the P20/N20 source can not only be found in target location, but especially also in orientation (Figure 4.3(a)). As also shown by others [22], [57], [185]–[187], [229], especially the orientation might play an important role in individualized targeting. It was then demonstrated also that the resulting targeted and D-CMI optimized mc-tDCS montages have large inter-individual differences (Figure 4.3(a) to (c)). FEM-based computer simulations then show that the individual D-CMI mc-tDCS montages, when compared to SB, lead to largely increased current directionality at the target side (DIR), while reducing uncontrolled stimulation of non-target sides by means of distribution over multiple electrodes. Thus, reduced side-effects as well as skin sensations, where the latter might also enable an easier sham conditioning can be expected.

The main hypothesis from FEM-based computer simulations was supported by the results in Tables 4.2 and 4.3) and in Figure 4.5. A significant interaction effect was observed between D-CMI and SB. The individually increased amplitudes shown in Figure 4.5 for D-CMI compared to SB also

shows an important individualized effect supporting better performance of D-CMI compared to SB. For D-CMI, 5 - 15 min (Post 1) after stimulation, a significantly increased SEF M20, both in signal (Figures 4.4 and 4.6) and source space (Figure 4.5, Tables 4.1 and 4.2), is observed (Pre vs Post 1), while no significant change is seen for the SB and Sham stimulations for Pre vs Post 1 (Tables 4.1 and 4.2). For SB, however, even if not significant, Figure 4.5 shows a slight increase in M20 source amplitude for Post 1 and in Figure 4.6(a) somatosensory topography is visible over the left hemisphere in Pre vs Post 1.

In previous studies, *in vitro* and *in vivo* recordings reported subthreshold modulation of neuronal activity that was induced by electric fields with intensities of 0.2 to 0.5 V/m [234]–[236]. Multiplication of these electric fields with cortical conductivity of 0.33 V/(Am) leads to 0.066 to 0.165 A/m<sup>2</sup>. In simulations, the D-CMI approach reached directional current densities at the P20/N20 dipole target of  $0.126 \pm 0.070$  A/m<sup>2</sup> (mean  $\pm$  SD over subjects), while SB remained at only  $0.085 \pm 0.044$  A/m<sup>2</sup>. The result that the directionality simulations are matching the experimental effect size thus support the hypothesis that simulated directionality can be used as a guide for planning of better controlled tDCS experiments.

The lack of a significant SB effect can have various reasons. It is first of all important to consider that Brodmann area 3b is a mainly tangentially-oriented target at the depths of the central sulcus, so that the voltage gradient along the pyramidal cells, i.e., the directionality (DIR), is rather small for SB. The result is in agreement with [70], where SB stimulation with a rectangular patch electrode placed over M1 could not achieve a significant effect on the P20/N20 SEP component. On the other side, [64] showed no significant difference in effect size between positionings of the SB anode over either M1 or S1 with regard to the M20 SEF component. One important difference to the study at hand is that [64], [70] only used 1 mA, while 2 mA was used here. Even more importantly, when considering the more posterior anodes in the successful D-CMI montages (see Figure 4.1 and 4.3(a)), both SB anode positionings over M1 and also S1 might be too frontal for an optimal DIR at the tangentially-oriented and deep S1 target. This has also been shown by [9] that in case of a tangential target, the placement of an SB pad over the target region misses the point of maximal stimulation, which lies between electrodes and not directly under the pad as commonly assumed.

Dieckhofer in [63] used 32 stimulation electrodes, from which 16 were placed over the parietal scalp (somatosensory cortex) and another 16 over the contralateral forehead. Their stimulation was thus comparable to an SB montage, too. While their anodal stimulation with a total injected current of 1 mA did not produce a significant effect on the P20/N20 SEP component, the mean amplitude of the P20/N20 SEP component did increase in four of the 10 min blocks after stimulation. The reasons for the missing significance might be the same as given for the SB montage above. Furthermore, the authors used standard modeling such as three layer sphere head modeling, fixed skull layer thickness and conductivity and a fixed tDCS montage for each of their 10 subjects without taking individual S1 target location and

orientation into consideration. Interestingly though in [228], a significantly increased effect was observed for the P20/N20 SEP component after anodal tDCS when the anodal patch of size  $18\text{cm}^2$  was placed over the motor association cortex, including the supplementary motor area (SMA) and the dorsal premotor cortex (PMd). In their study, a total injected current of 1 mA and a duration of 15 min was applied. The results indicated opposite effects on M1 and S1, i.e., M1 was inhibited whereas S1 was excited by activation of PM and SMA after anodal tDCS. Their study thus supports the hypothesis that areas 1 and 2, located in the postcentral gyrus, might also be involved in the modulations of S1 and might be directly affected by anodal tDCS applied over S1, as also discussed by [63], [237]. This might also have been the case in this study for both the D-CMI and SB montages. However, the SB approach did not lead to the same results as presented by [228] even though the anodal electrode ( $25\text{cm}^2$ ) was placed at the C3 electrode, i.e., over M1, and we stimulated with the higher intensity of 2 mA for 10 min.

In contrast to the above tDCS studies, in the presented study, individually targeted and D-CMI optimized mc-tDCS montages were produced. For the targeting, reconstruction of the P20/N20 source activity from combined SEP/SEF data in calibrated head models with regard to not only individual location, but especially also individual orientation was conducted. It was shown that especially target orientation has large inter-subject variability (Figure 4.3(a)). The D-CMI approach then produced optimized mc-tDCS montages according to both location and especially orientation of each subject's target in S1. It was shown that this complex and individualized procedure resulted in a significantly increased effect, in this case, M20 signal and underlying source strength, after stimulation (Pre vs Post 1). In contrast, the SB approach could not show a significant effect on the M20 SEF component (Pre vs Post 1) even though the same total injection current of 2 mA as in D-CMI was used. The comparison of the results between D-CMI and SB approaches, therefore, suggests that not only individual target location, but especially individual target orientation plays an important role as also investigated and proposed by [9], [22], [57], [185]–[187] and recently also found in a tACS study on the somatosensory cortex [229]. A total stimulation current of 2 mA might also be important, as it was earlier assumed that due to the depth of the central sulcus not enough currents reach the target area 3b with 1 mA [64], [70]. Bipolar montages are not necessarily less effective than mc-tDCS montages, since they can also be individually optimized for intensity. It is for example well known that maximum intensity optimization for a single tangential target source leads to two electrodes that take the target in the center [9] and, as [14], [189] have shown, due to Helmholtz reciprocity with the anode at the trough of the negative surface potential pole (for the somatosensory P20/N20 component the occipital trough of the N20) and the cathode at the peak of the positive surface potential pole (for the somatosensory P20/N20 component the frontal peak of the P20). D-CMI retains this basic idea but distributes the current over several electrodes around these two main electrodes, the farther the surface pole is from the target source, the more the current is distributed without much loss of directionality (see

Figures 4.1 and 4.3(a)). An optimized bipolar montage for a single tangential target source could thus possibly have achieved a similar effect, if the pads were centered around the two main electrodes and if the pads were cut to a size according to the size of the anodal and cathodal electrode surface areas of the D-CMI result. However, since not only factors such as pad electrode position, shape and size influence field distributions in the brain, but also electrode–skin contact impedance and electrode shunting effects [212], [238]. This reasoning is a rather theoretical one and expectation was that these factors were difficult to choose or control in bipolar montage stimulation, while D-CMI in combination with small gelled electrodes seems more practicable. Due to the practicality and because it was also used by others [64], [70], therefore, it was decided that standard bipolar (SB) montage should be used for comparisons here instead of individually-optimized bipolar montages.

While [70] showed a long-lasting increase in the amplitude of EEG somatosensory components after 1 mA anodal tDCS following median nerve stimulation, the situation is more complex in this evaluation. In the later time course comparison of Pre vs Post 2 and Pre vs Post 3, the D-CMI approach showed no significant changes on the peak amplitude of the MEG M20 source waveform, while SB and Sham showed a decreased effect while only significant in SB (Pre vs Post 2) (Table 4.3). Figure 4.5 shows even a continuous decrease in source amplitude over time from Post 1 down to Post 3 for all three stimulation conditions. Also in [63], the time course changes in EEG N20 amplitude evoked by stimulation of the contralateral median nerve of their Pre vs Post 2 and Pre vs Post 3 decreased when compared to their Pre vs Post 1 in their post-anodal 1 mA tDCS. Due to the expected robustness of the exogenous and stable EEG P20/N20 or MEG M20 for this chapter [16], [110], [230], [231], as shown in even the extreme case of anaesthesia [232], it was hypothesized that a decrease in reported source amplitude over time might be less due to fatigue of the subjects than to (i) changes in contact impedance of the electrodes for electric wrist and especially in this case for finger stimulation, as well as (ii) in case of EEG the electrode-skin contact impedance change and the electrode shunting effects [212], [238], [239] and in this case of MEG the increase in distance of the upper part of the head to the MEG dewar. The latter happens especially in sitting, but also even in lying positioning, resulting in registration errors and decreasing signal-to-noise ratio and thereby decreasing source amplitudes. This might then also explain why no longer significant effect was seen of D-CMI in the two later time course comparisons, where a possible increase in source amplitude might have been counterbalanced by (i) and (ii). While a recent study recommended an active-sham condition [227], mc-tDCS sham condition (Sham) was used here, which was based on montages created by the D-CMI approach (Figure 4.2). The results showed non-significant differences in perception between the stimulation conditions for the subjects (Tables 4.4 and 4.5). Table 4.5 shows that 10 subjects considered both D-CMI and Sham to be real stimulations, while 3 subjects were unsure. SB was the only condition rated as sham by a larger subgroup (6 times as sham and 7 times as real, see Table 4.4), possibly due to the larger SB stimulation patches and the resulting

decrease in skin sensations or just due to the change in electrode hardware between D-CMI/Sham and SB. This supports the hypothesis that the (D-CMI based) Sham condition was effective. Furthermore, the D-CMI eases sham conditioning: As D-CMI limits the maximal current per electrode and further distributes the injected currents over multiple electrodes, especially at distant sides to the target, it reduces skin sensations that can occur beneath the electrodes and thereby the contrast between the D-CMI and Sham conditions. Investigation of the effects of the stimulation on later components such as the P22 or the N30. This has various reasons and in short, the goal was to keep as good control over the experiment as possible. (1) First of all, a combined EEG/MEG instead of only MEG would have allowed us to also read out the effects of the stimulation on later and more radially oriented somatosensory components. However, this was not practicable with the available hardware. MEG alone is nearly blind to radial sources and thus not capable to read out stimulation effects on the P22, as also discussed by [64]. (2) Secondly, both the P22 and N30 have different origins with regard to both location and orientation than the P20. While the P22 from area 1 is at the crown of the gyrus and radially oriented [120], [240], recent investigations point to a whole network of sources that contribute to the N30 [210], namely Brodmann areas 3b and 1, the left ventrolateral thalamus and even frontal contributions. Even more importantly, since the N30 topography shows in most subjects inverted polarity to the P20, the orientation of the main contributor in Brodmann area 3b is inverted, too (Figure 4 in [210]). (3) Thirdly, similar to (constrained) maximum intensity (MI) optimization [9], [189], the D-CMI method used in this study was selected as a mainly intensity-based mc-tDCS with the goal of high directionality at the P20 target side. Due to the distribution of currents especially at distant electrodes from the target, side effects are reduced as well as sensations at the skin level such as tingling or pain. On the focality-intensity scale [9], [14], D-CMI is thus positioned close to MI, only slightly more focal. In contrast, focality-based optimization methods reach much lower intensity at non-target sides and thereby reduced side-effects, but on the cost of much lower directionality at the target side [9], [188], [213]. Therefore, due to the larger side-effects of the intensity-optimized D-CMI, the non-target P22 and N30 sources may have been stimulated by uncontrolled direct effects mixed with the incoming indirect effects from the P20 target. Due to the polarity-inverted N30 topography when compared to the P20, the possibly stronger excitatory indirect effects coming in from the exhibited P20 might have thus mixed up with the inhibitory direct stimulation effects of the main N30 source in Brodmann area 3b, leading possibly to an overall effect cancellation. (4) While the P20 is an exogenous component that can even be elicited under anaesthesia [16], [119], [232], the influence of attention and the basal state of the brain on later components increases. Also, the effects of tDCS might depend on the basal state of the brain at the time of its application [241], [242]. Although an effort was made to maintain a constant brain state in all subjects, their thoughts or expectations before, during, and after the stimulation could of course not be controlled.

---

This chapter in conclusion, shows the first application of the D-CMI mc-tDCS approach with integrated combined EEG/MEG target source reconstruction in a single blinded, sham-controlled somatosensory experiment. Results showed (9 subjects) a significant, though short-lasting stimulation effect on the P20/N20 source activity in Brodmann area 3b, while this could not be achieved with standard bipolar stimulation. Accurate targeting was performed using combined EEG/MEG in realistic skull-conductivity calibrated finite element head models. The new individualized targeting and stimulation approach might thus help to better control tDCS experiments and the well-known inter-individual stimulation effects.

# 5 Analysing inter-individual variability for simulated individually optimized transcranial electric fields

## 5.1 Introduction

In this chapter, the study [243] is presented, in which the author of this thesis had contributions as the second author. In this chapter, the term tES is used as a general approach for all types of transcranial electrical simulations. In this study, simulations of induced electric fields were conducted in FEM head models of 21 participants for tES generally. The optimization methods, the CMI (when the parameters  $S_{\text{maxelec}}$  and  $\lambda$  of D-CMI are fixed) and ADMM were compared with a fixed non-individually optimized 5x1 ring tDCS montage. A standard brain atlas was used to define the target location at the parietal cortex with three orthogonal orientations. Target 1 was defined as radial to the scalp surface (radial, RAD), target 2 as tangential to the scalp surface with an anterior-posterior orientation (tangential<sub>a-p</sub>, TAP), and target 3 as tangential with a left-right orientation (tangential<sub>l-r</sub>, TLR). By using this approach, it was possible to evaluate both the intensity and focality of the simulated electric fields and to compare them between the three methods (CMI, ADMM, 5x1). Realistic FEM head models were computed for twenty-one participants to assess parameter variability across subjects. Furthermore, the quantification parameter, parallelity of the electric fields to the stimulation targets, the targeting bias, and the heterogeneity of electric field properties across the three different target orientations were investigated. The hypothesis for this study was, that individually targeted tES montages computed with the CMI and ADMM algorithms will surpass the fixed control montage (5x1) with respect to target intensity and focality, respectively. In addition, it was assumed that targeted tES can adapt electrical fields in accordance with the stimulation target according to the variation in brain structure and orientation.

## 5.2 Materials and methods

Optimization of simulation electrode montages was applied, based on individual and automatically segmented six compartment FEM (6C FEM) head models using MATLAB (Natick, MA, USA), [SPM12](#), FieldTrip [233], and

METH [244] toolboxes, as well as custom MATLAB-scripts. Forward solutions were computed with the open-source toolbox SimBio.

### 5.2.1 Participants

Twenty-one right-handed participants (12 female,  $28.2 \pm 4.7$  years [range 20 to 37]) were included in this study. All participants reported no history of neurological or psychiatric disorders and had normal or corrected-to-normal visual acuity and hearing. Participants were reimbursed for participation and gave written informed consent prior to the experiment. The experiment was conducted in agreement with the declaration of Helsinki and the protocol was approved by the ethics committee of the Hamburg Medical Association (Ärztchamber Hamburg).

### 5.2.2 Data acquisition

For each subject structural T1 and T2-weighted (T1, T2) magnetic resonance (MR)-images were recorded with a 3T MR-scanner and a 64-channel head coil at an isotropic voxel resolution of  $1 \times 1 \times 1$  mm (Siemens Magnetom Prisma, Erlangen, Germany). Both, T1 and T2 images were acquired with an MP-RAGE pulse sequence (T1: TR/TE/TI/FA D 2300 ms/ 2.98 ms/ 1100 ms/ 9, FoV D  $192 \times 256 \times 256$  mm; T2: TR/TED 3200 ms/ 408 ms, FoVD  $192 \times 256 \times 256$  mm).

### 5.2.3 FEM head models

**Segmentation:** An SPM12 based automatic segmentation and custom image post-processing including Boolean and morphological operations [245], [246] was conducted incorporating T1 and T2 images. Structural T1 images were non-linearly co-registered onto the T2 images. SPM12 was then used to segment the images into five tissue compartments (white matter, gray matter, skull, skin, cerebrospinal fluid) for T1 images and T2 images separately. Binary gray scaled skin (SKIN), skull compacta (SC), skull spongiosa (SS), gray matter (GM), white matter (WM) and cerebrospinal fluid (CSF), compartment masks (Figure 5.1(a)-(d)) were produced by using Boolean and morphological operations and further processing the resulting probability maps. In order to distinguish SC from SS, the binary whole skull mask was eroded and thresholded using the original T2 probability maps [123], [183]. For the purpose of integrating the information contained in the different binary compartment masks, ambiguous labels were removed, while SC and SS were fixed to avoid leakage artifacts [247], [248]. Custom MATLAB software was used to interpolate missing tissue labels by using nominal information from neighboring voxel labels. The head volume was transformed to the CTF coordinate system (principal axes are going through fiducial points at the nasion and the bilateral tragi, X-axis towards nasion, Y-axis towards the left tragus, Z-axis towards the vertex). In order to reduce the size of the head model, the lower third of the volume was cut off.

**FEM Meshing:** A geometry-adapted hexahedral finite element mesh was computed for the 6C head model volume of each subject using software SimBio-VGRID. The geometry-adaptation was calculated using a node shift of 0.33 to ensure that the inferior angles at element vertices remain convex and the Jacobian determinant in the FEM computations remains positive.

**Tissue conductivities:** Tissue conductivities were defined as 0.33 (GM), 0.14 (WM), 1.79 (CSF), 0.43 (SKIN), 0.025 (SS) and 0.007 (SC), as well as 1.4 S/m for the electrodes [183], [188].

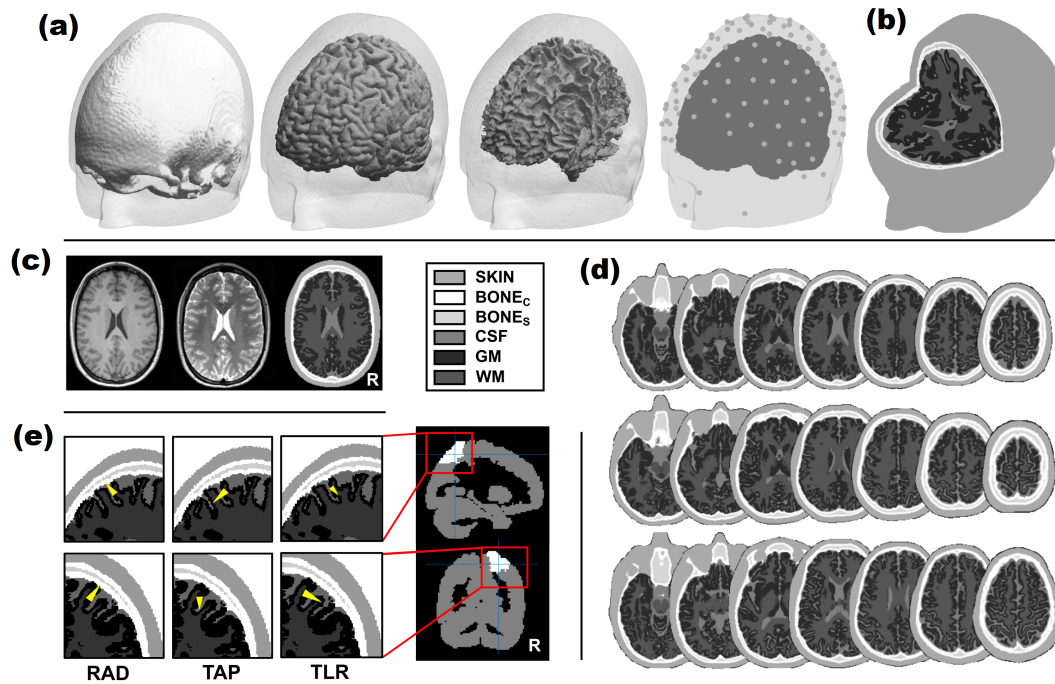


FIGURE 5.1: A) Isosurfaces of SC, GM and WM compartments (from left to right), plotted within the transparent SKIN compartment for one exemplary participant. Aligned electrode positions of the 126-channel layout and, electro-oculogram electrodes, as well as fiducials are shown with respect to the GM surface and projected onto the SKIN surface. B) Complete head model showing all six compartments for the same exemplary subject (see legend for color-codes). C) Correspondence between T1 and T2 MR images with the 6C segmentation in an axial slice of the same participant shown in A) and B). D) Exemplary MRI segmentations of three participants in axial slices. E) Stimulation target orientations (yellow cones) plotted on the 6C segmented volume as a close-up of the target region of interest in right SPL. Right SPL is highlighted (white) on the overall volume that is represented by the AAL atlas. Compartments are labeled as SKIN: scalp, SC: skull compacta, SS: skull spongiosa, CSF: cerebrospinal fluid, GM: gray matter, WM: white matter.

#### 5.2.4 Simulated brain targets and scalp electrodes

Individual electrode positions (for tES simulations) from 126-channel EEG caps (EasyCap, Herrsching, Germany) were optically registered (Xensor, ANT Neuro, Hengelo, The Netherlands) and averaged to a standardized template

across all subjects to eliminate potential measurement errors from the individual electrode registration. Template electrode positions were aligned to the individual head models, directed by the fiducial points (nasion and bilateral tragi, Figure 5.1(a)). Electrodes were simulated using a point electrode model [212], by projecting the aligned electrode position to the closest FEM node on the scalp surface. The overall stimulation current was scaled to 2 mA. In order to compare the different optimization and the control methods, the number of stimulation electrodes was fixed to  $n = 6$  for each individual stimulation montage. Stimulation targets were defined in the right superior parietal lobule (SPL) as a region of interest, based on the AAL brain atlas (Automated Anatomical Labeling) [249]. SPL was shown to be part of the dorsal fronto parietal attention network [250] and parietal cortex represents a realistic stimulation target for various tES applications [180],[251]. For each head model, individual 3D-grids (5 mm), sampling the combined CSF,GM and WM compartments were defined in CTF space. By linear normalization of the individual T1 images on the MNI152 template brain (Montreal Neurological Institute, Montreal, Canada), the individual grids were warped into MNI space to determine the average coordinate of all grid points within the right SPL in MNI-space. Using the inverse of the transformation matrix, target coordinates were then warped backed into the individual CTF coordinate system and projected on the closest GM node of the individual head models. Finally, three orthogonal target orientations were simulated with respect to the individual scalp surface (Figure 5.1(e)) to evaluate the reliability of electric fields for the two targeting algorithms and the control method across target orientations. One orientation was defined as radial to the scalp surface. Two tangential target orientations were computed along the anterior-posterior axis and along the left-right axis, respectively.

### 5.2.5 Multi-channel inverse optimization montages and induced electric fields flow simulations

In this study, the matrix  $\mathbf{A}$  was calculated with the same procedure as in Chapter 3. The matrix  $\mathbf{A}$  (as described in Chapter 3) can be used to find the best possible weighting of current at the stimulation electrodes under a defined set of constraints. As this study used a 128 channel EEG cap (EasyCap, Herrsching, Germany) so therefore there exists  $m = 1 \dots M$  with  $M = 127$  possible tDCS electrode positions. The  $M^{th}$  electrode again here is fixed as the reference electrode in all of the tDCS forward simulations (as defined in Chapter 3). Matrix  $\mathbf{A}$  was computed by combining the individual electrode positions and the 6C FEM head models with nodes ( $3.64 \pm 0.29$  million nodes [range 3.02 to 4.20 million]). The applied optimization algorithms compute the optimal stimulation montages by either maximizing the target current density or by applying additional constraints to the spatial extent of the electric field, in order to balance stimulation intensity and focality.

**ADMM:** For this study the ADMM method (also described in Chapter 3) was chosen for focality based electric field simulations. Following a two-step procedure for the ADMM ensured the fixed number of electrodes. The six

electrodes with the maximum current weighting were selected following an initial optimization. The applied currents were balanced, while separately preserving the optimized current weightings for anodes and cathodes, respectively. Results from pilot simulations showed reasonable electrode montages and current densities using this adapted version of the ADMM, while meeting the requirements of a fixed number of electrodes.  $S_{\text{Total}}$  was scaled to 2 mA.

**CMI:** For this study, the modified version of the Maximum Intensity algorithm [9], the Constrained Maximum Intensity (CMI) approach [213], [252] was used. As described in Chapter 3, by fixing the parameters ( $\lambda$  and  $S_{\text{maxelec}}$ ) for the D-CMI, the D-CMI can be modified to MI or CMI approach. So for this study  $\lambda = 250$  was chosen to slightly distribute the injected currents across six electrodes.  $S_{\text{Total}} = 2$  mA was set to fulfill the safety constraint and  $S_{\text{maxelec}} = 0.95$  mA to enforce a distribution of electrode currents and reduce the theoretical tactile perception of the stimulation under each electrode. In a two-step procedure, the stimulation montage was fixed to six electrodes for each individual stimulation montage.

**Fixed montage for control:** Fixed montages for typical tES applications, can be constructed by placing one central small electrode radially over the estimated stimulation target and placing four small electrodes with inverted polarity in a ring around the central electrode (4x1) [253]. This approach was shown to yield reasonable current densities, while limiting the spatial extent of the electric field, compared to tES using large and distant patch electrodes. In line with this procedure, a fixed controlled stimulation montage with five small electrodes was defined, arranged in a ring (5 x 1; considering the electrode layout in the current experiment) around a small center electrode that is placed closest to the radial projection of the target coordinate to the scalp, for the MNI152 template (Montreal Neurological Institute, Montreal, Canada). The defined 5 x 1 standard montage was applied to all individuals in order to simulate a normative stimulation montage design that was not individually optimized. The distance between the center-electrode and surrounding electrodes was optimized manually, with respect to intensity and spatial extent of the stimulation. This definition of the control montage mimics the conventional approach of tES applications which commonly neglects individual anatomy and orientation of the stimulation target.

### 5.2.6 Quantification and statistical analysis of modeling results

Current densities ( $\text{A}/\text{m}^2$ ) were computed for each node of the FEM head model. No significant leakage artifacts were revealed by the modeling results of current flow across participants and target orientations [247], [248]. Current density vectors were corrected for the angular deviation between the stimulated field and the target vector orientation. Stimulation intensity was defined as the 0.95 percentile of values within 5 mm distance to the target vector.

As can be seen in Figure 5.2(b) the highest intensity is not necessarily centered at the stimulation target, but a bias of the electric field orientation can be observed. In order to quantify the spatial extent of the electric field and taking this bias into account, the 0.95-percentile was computed as a function of the Euclidean distance to the stimulation target. Spatial extent was quantified as the distance (in mm) at 50 percent area under the curve of the normalized function.

Repeated measures 3x3-ANOVA were computed to compare the effect of three different stimulation methods (ADMM, CMI, 5x1) and three different target orientations (radial, tangential<sub>a-p</sub>, tangential<sub>l-r</sub>) for stimulation target intensity and focality, separately. Greenhouse-Geisser correction was applied, if the sphericity assumption was violated. Follow-up paired samples t-tests were computed and p-values were corrected for multiple comparisons using the Bonferroni-Holm method [250]. Non-parametric Spearman correlations were computed to describe the relationship between intensity and spatial extent for each method and target direction, separately. Sample means and standard deviations were reported, if not indicated otherwise.

Significance level was set to  $\alpha = 0.05$  and effect sizes  $\eta_p^2$  and  $r$  were reported, respectively. Corrected p-values are reported if not indicated otherwise. Detailed information on statistics is provided in tables 5.1 to 5.3.

## 5.3 Results and discussion

Current densities induced by individually optimized tES montages in realistic 6C FEM head models of twenty-one participants were simulated. A fixed control montage was compared with two individually targeted stimulation montages optimizing predominantly stimulation intensity or focality. Unilateral targets with three different vector orientations were positioned in the right SPL. It was shown that individual optimization allows to control variability due to individual structure, as well as target location and orientation. Although this effect was reliable across the sample, the results also reveal that even optimized electric fields are limited by individual anatomical properties. Taken together, the present results substantiate the need for integrating individual electric field simulations with tES applications.

### 5.3.1 Individual targeting adapts to individual stimulation requirements

Electrode montages provided by the ADMM and CMI algorithms showed the expected variation across subjects (see Figure 5.2). By recruiting more than one central stimulation electrode, the ADMM flexibly corrected the current flow, if the radial targets did not project directly on a stimulation electrode at the scalp surface. For tangential targets, ADMM provided two antagonistic electrode clusters that were placed close to one another along the target direction in order to preserve focality of the stimulation. For the CMI

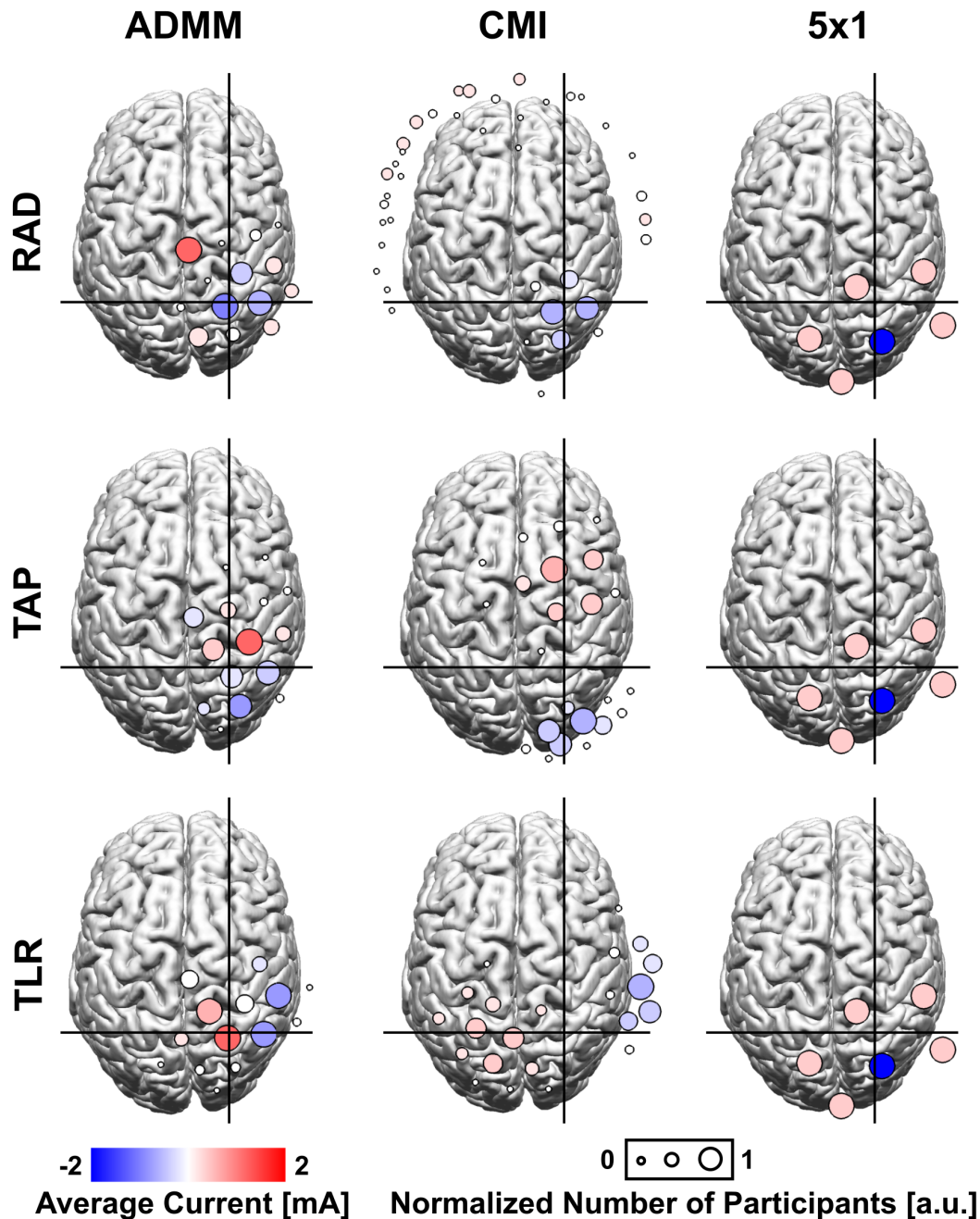


FIGURE 5.2: Three-dimensional illustration of the grand average electrode montages that were derived from the focality-optimizing ADMM, intensity-optimizing CMI and a 5x1 fixed control montage. A template cortical surface (FieldTrip) is plotted, viewed from the top. For each method (from left to right: ADMM, CMI, 5x1) and target orientation (from top to bottom: radial (RAD), tangential<sub>a-p</sub> (TAP), tangential<sub>l-r</sub> (TLR)) the electrode sizes reflect the number of participants for whom the respective electrode was part of the montage. Large circles illustrate that for all participants, this particular electrode was part of the montage. Smaller circles illustrate fewer usages of the particular electrode. The color of the circles shows the average current applied to the electrode across participants. Red and blue colors indicate that this particular electrode rather had the same polarity across subjects, as well as their relative weighting. White electrodes indicate either small current applied to the electrode or variable electrode polarity across participants. Electrodes that were not part of the resulting electrode montages were omitted, respectively. Crosshairs indicate the average location of the stimulation target in SPL. Control 5x1 montages show no variability in the electrode montages and uncorrected current densities, but are depicted here for illustrative reasons.

algorithm and the tangential target orientations, two similar electrode clusters were located with increased distance to one another, compared to the ADMM montages. In general, both optimization approaches made extensive use of the high density electrode layout in order to address the requirements of individual anatomy and variations in target location and orientation.

Furthermore, in practice the close distance of electrode positions in a high-density electrode layout enables the stimulation current to be split among a number of small electrodes [253]. Thus, still at increasing stimulation intensity, skin sensations can be minimized while preserving a minimal loss of focality of the electric field. The different electrode montages resulted in distinct properties of the induced electric fields with respect to parallelity (Figure 5.3) intensity, spatial extent, as well as reliability of the electric fields (Figure 5.4). Exemplary electrode montages and the resulting electric fields for one subject showed similar patterns as described for the sample (Figure 5.5).

The present data supports the conclusion that the utilization of high-density electrode layouts for the individual optimization of tES montages [189] is beneficial, in order to allow the adaptation to the stimulation target, under consideration of the individual anatomy of the participants. Exemplary electrode montages for one subject showed similar patterns as described above for the sample (Figure 5.5).

TABLE 5.1: Descriptive data for the bias and parallelity of the current density vector field, with respect to the stimulation target. Target orientations are labeled as RAD: radial, TAP: tangential<sub>a-p</sub> and TLR: tangential<sub>l-r</sub>. \* indicate =  $p < 0.05$ .

	Bias[mm]	Parallelity (%)
ADMM <sub>RAD</sub>	10.7 ±4.3	71 ±17
ADMM <sub>TAP</sub>	8.1 ±3.0	83 ±9
ADMM <sub>TLR</sub>	9.3 ±3.3	86 ±7
CMI <sub>RAP</sub>	26.4 ±21.5	81 ±15
CMI <sub>TAP</sub>	10.7 ±7.3	83 ±11
CMI <sub>TLR</sub>	10.5 ±6.3	86 ±10
5x1 <sub>RAD</sub>	24.3 ±4.8	50 ±17
5x1 <sub>TAP</sub>	10.0 ±3.5	74 ±17
5x1 <sub>TLR</sub>	23.6 ±6.4	24 ±15

### 5.3.2 Targeted electric field orientations

As expected, current density vectors resulting from the optimized tES montages were aligned with the target orientation (Figure 5.3 and 5.5, Table 5.1) [9], [188], [252]. In contrast, the control montage failed to reliably comply with the orientation of the electric field across the three target orientations. A significant interaction effect of the factors method and target orientation was

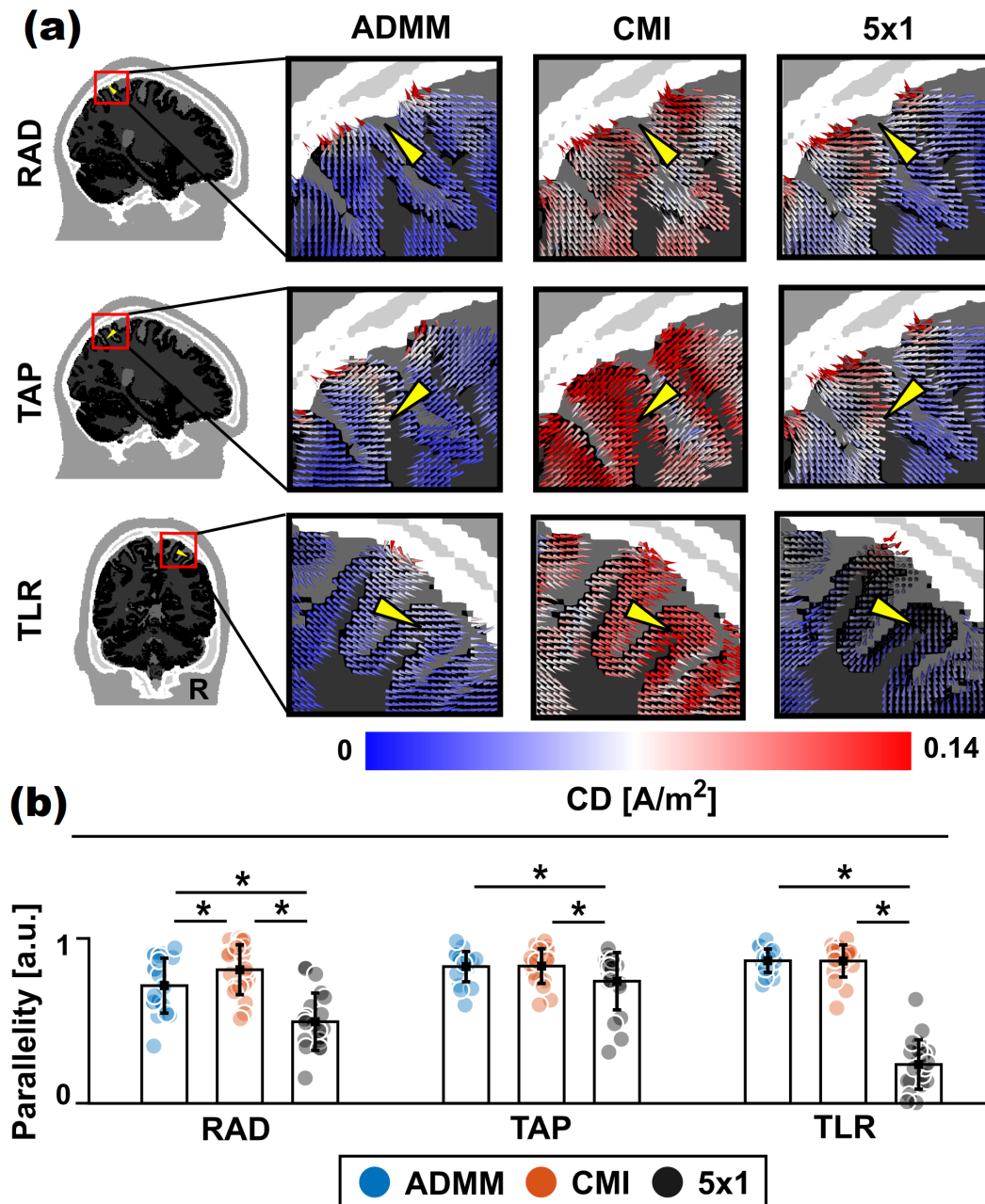


FIGURE 5.3: A) Close-up of the finite-element vector field and target vectors for all methods (from left to right: ADMM, CMI, 5x1) and target orientations (from top to bottom: radial, tangential<sub>a-p</sub>, tangential<sub>l-r</sub>) in one exemplary participant. To optimally depict the field alignment with the target vector orientation, sagittal slices are presented for the radial and tangential<sub>a-p</sub> targets and coronal slices are presented for the tangential<sub>l-r</sub> target. Vector fields were nicely aligned for both ADMM and CMI with varying spatial extent of the uncorrected current densities and varying maximal current densities. Control 5x1 montages showed no variability in the electric field, but clear misalignments of the target vector and the electric field were obvious, compared to the targeted electric fields and especially for the tangential<sub>l-r</sub> target orientation. B) On group level, parallelity (mean standard deviation; SD) was significantly smaller for the 5x1 control montage across all target orientations and showed large differences across target orientations for the 5x1 control montage. \* indicate  $p < 0.05$ .

observed (5.2) and follow-up t-tests revealed a consequently reduced parallelity for the electric fields, induced by the 5x1 montage, compared to the optimized montages for all target orientations (Table 5.3). In addition, for the radial orientation, CMI showed significantly higher parallelity, compared to the ADMM (Figure 5.3(b)).

Cortical pyramidal cells might be especially susceptible to electric fields that are oriented in parallel to the target orientation, and thus also to changes in the orientation of the electric field [Kieg2013, 1], [22], [57]. Although the specific role of the electric field orientation for tES-induced electric fields in humans is not yet resolved, in theory, an electric field that is orthogonal to a physiological dipole is not expected to exert an effect. Consequently, the alignment of tES-induced electric fields with the stimulation target is physiologically relevant. In the present study we explored the alignment of targeted electric fields compared to the alignment of the 5x1 control montage. Due to the deviating parallelity of electric fields in the control montage, corrected current densities are reported, considering the misalignment of the electric field vector and the respective target orientation.

The present study further indicates the importance to consider the target depth and orientation. Radial targets showed lower current densities, compared to both tangential orientations for ADMM and CMI (Figure 5.4) [9] while no difference was observed between the two tangential orientations, respectively. In the present study, stimulation targets were located in intermediate sulcal depth for all target orientations. Previous simulations of targeted tES investigated the effect of target depth, comparing superficial radial targets with intermediate or deep tangential targets [9], [188]. Herein, current densities were reduced, with increasing depth of the stimulation target [188]. However, these studies were inconclusive on how targeted stimulation can cope with varying target orientations, independent of target depth. I was concluded that - in intermediate depth of the simulated parietal target in the present experiment - targets with tangential orientations can be stimulated with a relatively higher current density, compared to radial targets, across individual participants. Nevertheless, the same does not necessarily hold for other stimulation targets in deeper [251], [254] or more superficial cortical areas, or other regions of the brain, other than parietal cortex [193].

### 5.3.3 Targeted stimulation intensities

In the present study target current densities ranged from  $0.007 \text{ A/m}^2$  (5x1, tangential<sub>l-r</sub>) to  $0.176 \text{ A/m}^2$  (CMI, radial). These observed target intensities fit into the range of previously reported FEM simulation results (Figure 5.2(a)) [77], [183], [188], [9], [255], [256]. Statistical analysis of target current densities revealed a significant interaction between the two included factors method and target orientation (Figure 5.4(a), Table 5.2). Across methods, CMI consistently showed significantly higher target current densities, compared to the ADMM and 5x1, as revealed by follow-up t-tests (Table 5.3)).

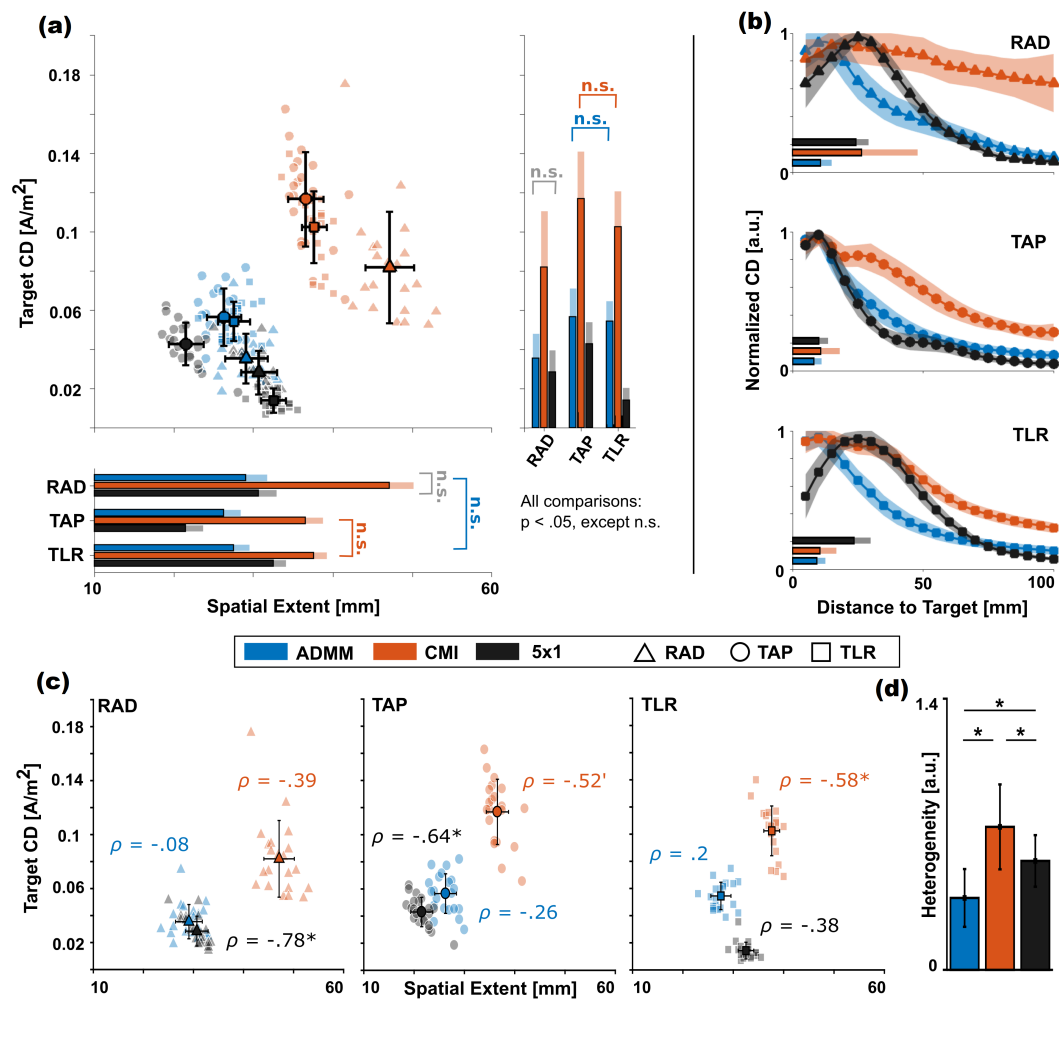


FIGURE 5.4: A) Target current densities (CD) plotted against the spatial extent for every method and target orientation. Group averages are represented by colored symbols with black edges (mean  $\pm$  SD). Single-subjects are plotted in light colors. Bar graphs illustrate the descriptive average target CD and spatial extent, respectively. Light colored stacked bars represent the SD. Statistical analysis, comparing target current densities and spatial extent reveals significant differences in both parameters. Results are reported in detail in Table 5.2 and 5.3. n.s. indicates not significant ( $p > 0.05$ ). B) Line plots represent averages of individually normalized current densities as a function of distance to the target vector for each of the applied methods and target orientations (from top to bottom: radial, tangential<sub>a-p</sub>, tangential<sub>l-r</sub>), illustrating the distribution of the electric field, independently of the intensity. Colored bars indicate bias (mean  $\pm$  SD) of the targeted electric fields (see Table 5.1). C) Non-parametric Spearman correlations were computed and revealed negative relations of target current densities and spatial extent in some method-target combination. In other words, some subjects showed an increased profile of the electric field parameters both being more intense and more specific, compared to other subjects, even for the targeted CMI. D) Heterogeneity (mean  $\pm$  SD) for each ADMM, CMI and 5x1 control montage across stimulation target orientations. Small heterogeneity reflects the reliability of the respective method across different stimulation target orientations (high values indicate heterogeneity; low values indicate homogeneity).

\* indicate  $p < 0.1$  and \*\* indicate  $p < 0.05$ .

For both tangential target orientations, ADMM showed increased target current densities, compared to the 5x1 control montages, but not for the radial orientation, indicating the feasibility of control montages for some specific applications. For the ADMM and the CMI, targeted electric fields at the radial target showed significantly lower current densities compared to both tangential targets (Table 5.3)), while no difference was observed between the two tangential orientations, respectively. For the 5x1 condition, higher target current densities were observed for the tangential<sub>a-p</sub> orientation, compared to the radial and tangential<sub>l-r</sub> target orientations. For the same method the tangential<sub>l-r</sub> orientation was significantly reduced, compared to the radial target.

In previous studies, *in vitro* and *in vivo* recordings reported subthreshold modulation of neuronal activity that were induced by electric fields with peak intensities at 0.2 to 0.5 V/m (approx. 0.066 to 0.165 A/m<sup>2</sup>) using alternating current stimulation [234], [236]. In line with previous modeling results [9], [77], [183], [188], [256], the present results indicate that tES is acting at the lower end at which electric fields were reported to modulate neural activity (see Figure 5.4) [234], [257]. Still, due to varying tissue conductivities [5], [115], [123], [196], effects of network electric activity [234], [257] and the effective state of the stimulated neuronal population in humans [258], [259], already relatively weak electric fields might potentially modulate neuronal activity in specific cases.

Using the CMI algorithm, the target current densities were increased for the given parietal stimulation target, compared to ADMM and the 5x1 control montages (Figure 5.4, Table 5.3). ADMM showed increased target current densities for the tangential stimulation targets, compared to the 5x1 control.

By increasing the target current density, the probability is increased that individual electric fields will take physiological effect within the stimulation target [196], [257].

Taken together, the present results substantiate the importance of targeting the electric field with respect to the stimulation target in order to maximize the potentially effective electric field intensity, as well as the physiologically relevant field orientation.

Although it is not yet resolved to what extent the electric field strength is affecting the behavioral tES outcome, preliminary results indicate its physiological relevance [222], [260].

### 5.3.4 Targeted electric field distribution and bias

Evaluation of the spatial extent across methods and target orientations revealed a significant interaction effect (Table 5.1)).

ADMM optimized electric fields were characterized by small spatial extent, i.e. maximal current densities in close vicinity to the target and steep slopes of current density as a function of distance to the stimulation target (Figure 5.4(a) and (b)).

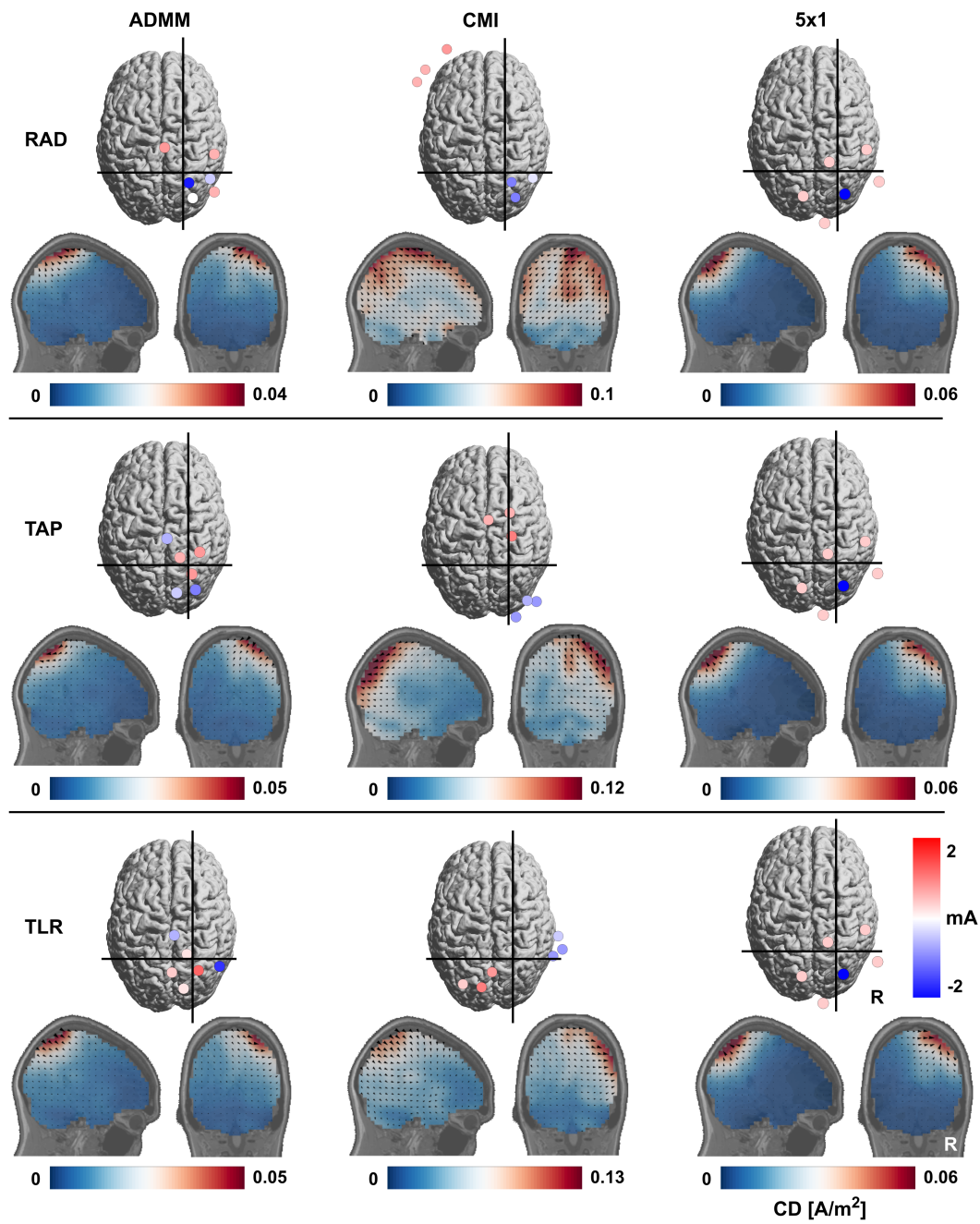


FIGURE 5.5: Close-up of the finite-element vector field and target vectors for all methods (from left to right: ADMM, CMI, 5x1) and target orientations (from top to bottom: radial, tangential<sub>a-p</sub>, tangential<sub>l-r</sub>) in one exemplary participant. To optimally depict the field alignment with the target vector orientation, sagittal slices are presented for the radial and tangential<sub>a-p</sub> targets and a coronal slice was chosen for the tangential<sub>l-r</sub> target. Vector fields were nicely aligned for both ADMM and CMI with varying spatial extent of the uncorrected current densities and varying maximal current densities. Control 5x1 montages showed no variability in the electric field, but clear misalignments of the target vector and the electric field were obvious, compared to the targeted electric fields and especially for the tangential<sub>l-r</sub> target orientation.

TABLE 5.2: Results of ANOVA's testing differences in target intensity, spatial extent, parallelity and bias. Repeated measures ANOVA's were computed across methods (ADMM, CMI, 5x1) and target orientations (radial, tangential<sub>a-p</sub>, tangential<sub>l-r</sub>). Significant main effects for both factors and a first order interaction effect were revealed. \* indicate  $p < 0.05$ .

		p	$F_{df}$	df	$\eta_p^2$
Intensity	Method	< .0001	509.8 *	2, 40	0.96
	Target orientation	< .0001	21.1 *	2, 40	0.51
	Method x Target orientation	< .0001	19 *	2.5, 49.9	0.49
Spatial extent	Method	< .0001	900.1 *	2, 40	0.98
	Target orientation	< .0001	180.6 *	2, 40	0.90
	Method x Target orientation	< .0001	70.5 *	2.6, 51.3	0.78
Bias	Method	< .0001	17.81 *	1.2, 23.9	0.47
	Target orientation	< .0001	22.74 *	2, 40	0.53
	Method x Target orientation	.0001	11.22 *	1.5, 30.5	0.36
Parallelity	Method	< .0001	372.8 *	2, 40	0.95
	Target orientation	0.003	8.3 *	1.5, 30.6	0.29
	Method x Target orientation	< .0001	47.3 *	2.5, 50.9	0.70

TABLE 5.3: Follow-up t-tests of the method x target orientation interaction showing differences in target intensity and spatial extent across target orientations. Target orientations are labeled as RAD: radial, TAP: tangential<sub>a-p</sub> and TLR: tangential<sub>l-r</sub>. \* indicate =  $p < 0.05$ .

		Intensity $t_{20,r}$	Spatial extent $t_{20,r}$	Bias $t_{20,r}$	Parallelity $t_{20,r}$
ADMM <sub>RAD</sub>	CMI <sub>RAD</sub>	-12.32*,0.94	-21.04*,0.98	-3.53*,0.62	-3.06*,0.56
ADMM <sub>RAD</sub>	5x1 <sub>RAD</sub>	2.46,0.48	-2.32,0.46	-9.79*,0.91	5.89*,0.80
CMI <sub>RAD</sub>	5x1 <sub>RAD</sub>	9.70*,0.91	19.44*,0.97	0.43,0.10	8.40*,0.88
ADMM <sub>TAP</sub>	CMI <sub>TAP</sub>	-16.33*,0.96	-28.08*,0.99	-1.86,0.38	-0.23,0.05
ADMM <sub>TAP</sub>	5x1 <sub>TAP</sub>	4.99*,0.74	8.22*,0.88	-2.61,0.50	2.70*,0.52
CMI <sub>TAP</sub>	5x1 <sub>TAP</sub>	20.52*,0.98	23.78*,0.98	0.51,0.11	3.17*,0.58
ADMM <sub>TLR</sub>	CMI <sub>TLR</sub>	-14.54*,0.96	-24.55*,0.98	-1.16,0.25	0.15,0.03
ADMM <sub>TLR</sub>	5x1 <sub>TLR</sub>	14.75*,0.96	-9.49*,0.90	-10.26*,0.92	18.29*,0.97
CMI <sub>TLR</sub>	5x1 <sub>TLR</sub>	23.76*,0.98	12.71*,0.94	-6.6,6*,0.83	18.44*,0.97

No difference in intensities and spatial extent of electric field was revealed between ADMM and 5x1 montages for the radial orientation by follow-up t-tests (Table 5.3)). At the same time, electrode montages computed with the CMI consistently showed the largest spatial extent of electric fields across all target orientations, compared to ADMM and the 5x1 control montage, spatial extent was largest for the tangential<sub>l-r</sub> and smallest for the tangential<sub>a-p</sub> orientation. All comparisons between the orientation conditions for the 5x1 revealed significant differences for the spatial extent.

At the same time, electrode montages computed with the CMI consistently showed the largest spatial extent of electric fields across all target orientations compared to ADMM and the 5x1 control montage. With respect to the tangential<sub>a-p</sub> target, 5x1 montages showed significantly reduced spatial extent of the simulated electric fields, compared to both optimized methods. The spatial extent of ADMM electric fields was reduced for the tangential<sub>l-r</sub> orientation, compared to both CMI and the 5x1 control.

In addition to the spatial extent of electric fields, an interaction effect of the factors method and target orientation was revealed for the targeting bias (Table 2). ADMM consistently resulted in small targeting bias of the electric field, with respect to the stimulation target (Figure 5.4(b), Table 5.1). Although CMI showed a small bias for both tangential target orientations comparable to ADMM. The CMI-derived electric fields for the radial orientation showed a high bias (26 mm) and descriptively high inter-individual variability (Table 5.1). Electric fields derived from the 5x1 montages showed a strong bias of up to 24 mm for the radial and tangential<sub>l-r</sub> orientations, compared to the ADMM-derived electric fields (Figure 5.4(b), Table 5.1 and 5.3). For the tangential<sub>a-p</sub> target orientation the electric fields bias of the 5x1 control montage was significantly reduced compared to ADMM (which showed a descriptively small bias already).

In sum, we conclude that ADMM was able to accurately direct the electric field to the stimulation target, while adapting to different target orientations and with reliable spatial extent of electric fields. The electrode montages for CMI and the radial orientation were widely distributed across the scalp (Figure 5.2) inducing widely distributed electric fields (Figure 5.4(a) and 5.5) which also resulted in an increased bias across subjects, however, only for the CMI and the radial orientation. For the tangential targets CMI achieved an accurate targeting, although the electric fields were extended across the brain compared to ADMM and 5x1 control montages. The 5x1 control montage showed quite focal electric fields across the different target orientations. However, for the radial and the tangential<sub>l-r</sub> targets the high bias compromised the spatial extent of the electric fields with respect to the stimulation target (and thereby also the target current densities). It has to be noted that for the tangential<sub>a-p</sub> target the 5x1 montage resulted in reasonable focality and only a small bias (in addition to a reasonable alignment of the electric field with the target orientation; Figure 5.4(a) and (b)). Therefore, it can be assumed that for some situations a standard montage can result in potentially effective electric fields. However, with respect to physiologically effective target current densities that can be assumed to modulate neuronal

activity [234]–[236], [257], even slight differences in the target current densities might decide on the tES treatment to take effect or not. In this context, the presented data indicates that it is important to consider the targeting of the electric field (spatial extent and bias), to effectively direct the electric field to the stimulation target.

### 5.3.5 Homogeneity of electric fields across target orientations

In order to describe the reliability of the targeting methods, we quantified the homogeneity of electric field intensities and focality of electric fields across the three different target orientations. A reliable method would need flexible handling of the electrode positioning, in order to control the electric field inside the head model with changing target orientation (this is similar to the size of the point cloud for each color in 5.4(a)).

On average, ADMM showed most homogenous results ( $0.37 \pm 0.15$  SD), followed by the 5x1 control ( $0.56 \pm 0.13$  SD) and CMI ( $0.74 \pm 0.22$  SD; 5.4(d)). A repeated measures ANOVA confirmed significant homogeneity differences between the methods ( $F_{1.5,30.2} = 35.25$ ,  $p < .001$ ). Follow-up t-tests revealed significant differences between all three comparisons (ADMM < CMI:  $t_{20} = -10.38$ ,  $p < .001$ ,  $r = .92$ ; ADMM < 5x1:  $t_{20} = -4.94$ ,  $p < .001$ ,  $r = .74$ ; CMI > 5x1:  $t_{20} = 3.22$ ,  $p = .004$ ,  $r = .58$ ).

In sum, ADMM showed more reliable results across the three different target orientations of the simulated parietal target in the present study, compared to the 5x1 control and the CMI in terms of electric field homogeneity. Although ADMM restricts the distance of electrode positions to the stimulation target (Figure 5.2), it manages to reliably adapt the target intensities and spatial extent of electric fields according to the target orientation, with only slight changes to the electrode positions. CMI likely resulted in heterogeneous results, due to its rationale to only control the target intensity, irrespective of the spatial extent of the induced electric fields. As can be seen in Figure 5.2 (especially for the radial orientation), CMI makes extensive use of the electrode layout to place the electrodes according to the individual anatomy. This results in increased target current densities, but also increased heterogeneity. As can be seen in Figure 5.2, the 5x1 control montage is not adapted to the stimulation target orientation and the resulting electric fields are highly dependent on the respective anatomical properties and target orientations. Overall, the 5x1 control shows less homogenous results, compared to the ADMM (Figure 5.4(d); Table 5.1), reduced alignment of the electric fields to the target orientation (5.3) and, at least partly, strong bias of the electric fields (Figure 5.4(b), Table 5.1).

### 5.3.6 Target dependent individual stimulation profiles

As described previously [9], a trade-off was observed between intensity and focality, when comparing focality optimizing (ADMM) and intensity - optimizing (CMI) algorithms for targeted tES (Figure 5.4(a)). However, both the ADMM and the CMI were not able to homogenize the variability of target

intensities across subjects, given that the same current was applied to the electrodes in all montages and head models (5.4(a)). Instead, the individually optimized target intensity was computed, which seemed to be limited by the individual anatomical properties of the head model for the given parietal stimulation target. Rather, ADMM and CMI both exhibited their effect by optimizing the electric field distribution and orientation with respect to the stimulation target and herein were less prone to varying anatomy, or exact location and orientation of the target within the individual parietal cortices. Both optimization algorithms were able to reliably reduce the bias of electric field maxima, with respect to the varying stimulation targets.

Across subjects an inverse relationship between intensity and focality was apparent in the present data (Figure 5.4(c)). Some subjects showed higher values of stimulation intensity and focality in parietal cortex for some CMI and 5x1 montages, relative to other subjects. This observation indicates that no within-subject trade-off between target intensity and spatial extent can be held accountable for the inter-subject variability of the electric field properties. The data rather indicate the existence of individual profiles that might determine the potential tES-efficacy for a given stimulation target, solely based on the individual anatomy. In sum, the a priori estimation and the post-hoc evaluation of individual tES-induced target current densities are highly recommended in order to evaluate effects of individual anatomy on the behavioral or neurophysiological efficacy of tES. Recent studies showed that the stimulation intensity and focality that can be achieved by targeting is strongly dependent on the respective location of the stimulation target within the cortex of one standard FEM head model [193], [218]. Critically, the present results further indicate that, in addition, inter-individual variability (i.e. across head models) should be considered for each target location, due to the high variability that is introduced by individual anatomy.

In this framework, individually targeted tES may improve the control over induced electric fields to raise the probability of tES to take effect. In the present study, ADMM and CMI both exhibited their effect by optimizing the electric field properties with respect to the stimulation target. CMI was able to maximize the target current densities along the target orientation (target intensity) for all target orientations and across subjects. ADMM produced electric fields that were less prone to varying orientations of the target within the individual parietal cortices (homogeneity; Figure 5.4(d)) compared to CMI and the 5x1 control. In addition, for ADMM the overall smallest bias was observed (Figure 5.4(b)).

## 5.4 Conclusion

Individual anatomical properties lead to variability of induced electric fields and thereby to differences in the potential tES efficacy. Targeting of tES electric fields using one of various optimization algorithms [9], [189], [193], [254] is suitable to increase the level of control over the individual intracranial current densities with respect to target intensities, as well as target orientation

and specificity of the electric field (bias and spatial extent). The intensity-optimizing CMI algorithm improves the target intensity of the electric fields estimated in individual head models, thereby raising the overall chance of a physiological tES effect [261]. The experimental sample size that was used allowed insight into the dependency of optimized stimulation montages and electric field properties on the individual anatomy. It was shown that optimized stimulation target intensity and focality show variation across inter-individual FEM head models for the given parietal stimulation target. These results complement recent studies that showed large variation across cortical regions in one FEM headmodel [193], [218]. The electric field showed variation in the target intensity that indicates differences in the potential efficacy of tES across subjects, given that the same current is applied to all participants. While a correspondence of the tES-induced electric fields and individual neurophysiological [222], [260] and behavioral tES effects seems absolute intuitive, until now this relation lacks of substantial experimental evidence. In conclusion, FEM simulation results might help to increase the physiological interpretability of tES effects using targeted tES. It was proposed that an algorithmic definition of individual stimulation montages a priori and the detailed analysis of estimated electric fields has potential to improve the understanding of mechanisms underlying tES and thus its' effectiveness in future applications.

## 5.5 Author's contribution

The author's contributions for this study are the following

- Providing Matlab codes and simulations running support for the CMI and ADMM optimization algorithms.
- Providing support and knowledge for running electric field simulations using SimBio for mc-tDCS methods(CMI and ADMM).
- Support for editing of text in sections regarding the CMI and ADMM algorithms, SimBio electric field simulation, quantification metrics and interpretation of results.

## 6 Conclusion and outlook

In this thesis, titled **“Modeling and measuring the effects of individually optimized multi-channel transcranial direct current stimulation on the human brain”**, tDCS simulations and an experimental stimulation studies were presented that together aimed to explore, potentially improve and control the effects of mc-tDCS. Below the complete thesis will be summarized succinctly, followed by a discussion of the results and future recommendations.

### 6.1 Summary

In Chapter 3, a novel mc-tDCS optimization approach, the D-CMI, is presented, investigated and compared to intensity, focality and standard methods i.e. the MI, ADMM and standard bipolar methods, respectively, to target the Brodmann area 3b sources of the somatosensory P20/N20 components in a group of ten healthy subjects. A combined EEG/MEG source analysis pipeline with calibrated realistic head models is motivated to be used to accurately reconstruct the target source (P20/N20 somatosensory source at Brodmann area 3b) with individualized target location and orientation for tDCS targeted simulations. The resulting simulated electric fields for the D-CMI, MI, ADMM and standard bipolar tDCS methods targeting the individualized P20/N20 somatosensory targets at Brodamann area 3b were compared by performance metrics such as directionality (DIR), intensity in target (IT), intensity in non-target (INT), parallelity (PAR) and focality (FOC). Significantly higher DIR and IT was achieved by the D-CMI and MI approaches compared to the ADMM and standard bipolar approaches. The D-CMI, MI and ADDM showed significantly higher PAR compared to the standard bipolar method which showed a better controlled stimulation for P20/N20 target. The D-CMI not only showed high similarity to MI but had an additional advantage of distributing the stimulation currents over multiple electrodes. This attribute has the potential to reduce skin sensations and electric field amplitude in distant brain areas. The D-CMI is preferred for the follow-up experiment validation in Chapter 4 to target the P20/N20 somatosensory component at the Brodaman area 3b and compared to the standard bipolar method.

In Chapter 4, the first application of the novel D-CMI mc-tDCS approach is conducted in a single-blinded, sham-controlled somatosensory experiment with a group of 13 healthy subjects. Similarly to Chapter 3, a combined EEG/MEG source analysis pipeline with calibrated realistic head models is used for reconstruction of the P20/N20 somatosensory targets at Brodmann area 3b for the 13 healthy subjects. Three experimental tDCS condition for the D-CMI, standard bipolar and Sham (D-CMI based), were conducted.

MEG was only used to sensitively read out tDCS stimulation effects on finger stimulated SEF data from the three tDCS conditions (D-CMI, standard bipolar and Sham) before and after tDCS stimulation. The statistical analysis of the M20 SEF component showed a significant increase in interaction effects of the D-CMI approach compared to the standard bipolar and Sham conditions. The D-CMI also showed a significantly increased amplitude, though short lasting (5-15 min) compared to before tDCS stimulation while standard bipolar showed no significant increased amplitude effects. These statistical observations tend to show that the D-CMI approach outperforms the standard bipolar method when stimulating the somatosensory P20/N20 component at Brodmann area 3b. A statistical comparison of sham perception among the tDCS conditions showed no significant differences supporting the hypothesis that Sham condition was also successful.

In Chapter 5, electric fields for, in general, tES were simulated with three different tES methods (CMI, ADMM and 5x1) for three different target orientations (RAD, TAP and TLR) in a study with 21 subjects. In this study, the CMI, when the parameters of D-CMI were fixed, is used as the intensity based method. The locations for the tES target was at the parietal cortex. As part of this study, all participants were subjected to two individually tailored tES montages (CMI and ADMM) and a fixed stimulation montage (5x1) that was not individually optimized. As a result of simulations of a parietal stimulation target with three different orientations, the individual current densities were found to show varying intensities near the lower limit where physiological efficacy can be assumed for electric fields. Targeting algorithms were able to control different electric field properties, by either maximizing the target current densities or by increasing the specificity of electric fields with respect to target location and orientation. The results shown in this study support the usage of individualized targeting, such as discussed in Chapter 3 and Chapter 4, for enhancing the efficacy of tES and for elucidating the underlying mechanisms of tES.

## 6.2 Discussion and future perspective

One common attribute observed in all the three studies was the persistence of inter-subject variability, even if at least, the variation (standard deviation) in parallelity was considerably reduced by mc-tDCS optimization approaches when compared to the standard approaches. The mc-tDCS optimization approaches were not able to reduce the inter-individual variability of target intensities on a descriptive level, given that the same current was applied to the electrodes in all montages and head models. Part of the variability might be due to for example a deeper target, a lower skull conductivity, or a thicker CSF compartment of a particular subject.

Intensity based mc-tDCS approaches such as the MI, CMI and D-CMI were preferred over focality (ADMM) or standard approaches when targeting tangentially oriented targets as high current intensity and directionality is achieved. Skull conductivity calibration is highly recommended if availability of both MEG and EEG is possible. Complementary information provided

from MEG and EEG is very advantageous to accurately reconstruct the location and orientation of the underlying EEG/MEG brain activity for targeting. As the mc-tDCS optimization approaches align according to the orientation of the target area, the resulting electric fields in parallel to the accurately reconstructed target orientation increases the probability of tDCS effects. This hypothesis is validated for the novel D-CMI mc-tDCS approach in an experimental study (Chapter 4) compared to the standard bipolar approach.

Possible effects of the electrode–electrolyte spatial mismatch [262] and electrode displacement [263] were ignored in the presented studies. However, these important aspects should be considered in future simulations and comparisons of different mc-tDCS optimization methods. Factors such as electrode shape and size, electrode–skin contact impedance and electrode shunting effects can also influence field distributions in the brain [238], [264] and should also be considered for tDCS based electric field simulation in the future. Due to the maximum principle [15], none of the presented stimulation approaches is able to generate a peak intensity at a deeper target side, intensity maxima were always at the closest cortical areas to the stimulation electrodes. For non-invasive deep brain stimulation, other technologies were therefore needed such as temporally interfering electric fields [265].

With regard to forward modeling, individualized six compartment geometry adapted hexahedral FEM head models were used for source analysis (Chapter 3 and 4) and tDCS (optimized mc-tDCS and standard tDCS methods) induced electric field simulations (Chapter 3, 4 and 5). White matter anisotropy was integrated for studies in Chapter 3 and Chapter 4 while in Chapter 5 only isotropic conductivities were used for all tissue compartments. Studies incorporating source analysis for reconstruction of the target (Chapter 3 and 4), conductivity of the skull was individually estimated by using the complementary information from a combined EEG/MEG approach. In the absence of EEG and MEG modalities, a brain atlas based automated anatomical labeling (AAL) method was used to define the target in Chapter 5. In Chapter 3 and Chapter 4, the somatosensory target's location and orientation at Brodmann area 3b was calculated from combined EEG/MEG source analysis, while in Chapter 5, it was simulated at right superior parietal lobule (SPL) with three different orientations (two tangential and one radial) with respect to the individual scalp surface. With regard to skull conductivity, it is the most influential conductivity parameter for both EEG source analysis [6] and tES simulation [5], [193] and is considerably varying inter-individually [182]. However, the possibility of skin conductivity influencing inter-subject variability [5], [6], [193] cannot be excluded. The brain skull interface does not only contain CSF [266], but also the meninges (dura matter [267], arachnoid mater, and pia mater) as well as blood vessels [268]. Therefore, even if first simulations show that SEF/SEP skull conductivity calibration procedure can compensate at least for parts of these individual modeling inaccuracies, the accuracy of the forward modeling should be further improved by these additional tissue compartments.

Finally, the main focus in the future should be given to clinical applications of the presented novel D-CMI approach and mc-tDCS optimization

approaches for different target regions in the brain such as dorsolateral prefrontal cortex (dlPFC), motor cortex (M1), auditory cortex and possibly with different non-invasive brain stimulation techniques such as tACS and tRNS. As it was shown in [269], that quasistatic approximation is fairly good even for rapid stimulation pulses using higher frequencies (above 1 kHz). Therefore, it should be possible to generalize the findings in this thesis to at least low-frequency (e.g. below 100 Hz) tACS. Brain disorders such as focal epilepsy can be potentially reduced with tDCS as recently shown in [216], [270]. Application of the D-CMI approach has also shown promising results for a single patient with epilepsy [271]. Moreover, the software framework Duneuro [272] can also be used for improved and faster automatic pipelining for D-CMI, mc-tDCS and tES in general, calibration and accurate forward modeling.

## References

- [1] M. A. Nitsche and W. Paulus, "Excitability changes induced in the human motor cortex by weak transcranial direct current stimulation," *The Journal of Physiology*, vol. 527, no. 3, pp. 633–639, Sep. 2000.
- [2] W. Paulus, "Transcranial electrical stimulation (tes – tdc; trns, tacs) methods," *Neuropsychological Rehabilitation*, vol. 21, no. 5, pp. 602–617, Oct. 2011.
- [3] H. McCann, G. Pisano, and L. Beltrachini, "Variation in reported human head tissue electrical conductivity values," *Brain Topography*, vol. 32, no. 5, pp. 825–858, May 2019.
- [4] M. Akhtari, H. Bryant, A. Mamelak, E. Flynn, L. Heller, J. Shih, M. Mandelkem, A. Matlachov, D. Ranken, E. Best, M. DiMauro, R. Lee, and W. Sutherling, "Conductivities of three-layer live human skull," *Brain Topography*, vol. 14, no. 3, pp. 151–167, 2002.
- [5] C. Schmidt, S. Wagner, M. Burger, U. van Rienen, and C. H. Wolters, "Impact of uncertain head tissue conductivity in the optimization of transcranial direct current stimulation for an auditory target," *Journal of Neural Engineering*, vol. 12, no. 4, p. 046 028, Jul. 2015.
- [6] J. Vorwerk, Ü. Aydin, C. H. Wolters, and C. R. Butson, "Influence of head tissue conductivity uncertainties on EEG dipole reconstruction," *Frontiers in Neuroscience*, vol. 13, Jun. 2019.
- [7] J. C. Horvath, J. D. Forte, and O. Carter, "Quantitative review finds no evidence of cognitive effects in healthy populations from single-session transcranial direct current stimulation (tdcs)," *Brain Stimulation*, vol. 8, no. 3, pp. 535–550, May 2015.
- [8] I. Laakso, S. Tanaka, S. Koyama, V. D. Santis, and A. Hirata, "Inter-subject variability in electric fields of motor cortical tDCS," *Brain Stimulation*, vol. 8, no. 5, pp. 906–913, Sep. 2015.
- [9] J. P. Dmochowski, A. Datta, M. Bikson, Y. Su, and L. C. Parra, "Optimized multi-electrode stimulation increases focality and intensity at target," *Journal of Neural Engineering*, vol. 8, no. 4, p. 046 011, Jun. 2011.
- [10] J. P. Dmochowski, A. Datta, Y. Huang, J. D. Richardson, M. Bikson, J. Fridriksson, and L. C. Parra, "Targeted transcranial direct current stimulation for rehabilitation after stroke," *NeuroImage*, vol. 75, pp. 12–19, Jul. 2013.
- [11] R. J. Sadleir, T. D. Vannorsdall, D. J. Schretlen, and B. Gordon, "Target optimization in transcranial direct current stimulation," *Frontiers in Psychiatry*, vol. 3, 2012.

- [12] G. Ruffini, M. D. Fox, O. Ripolles, P. C. Miranda, and A. Pascual-Leone, "Optimization of multifocal transcranial current stimulation for weighted cortical pattern targeting from realistic modeling of electric fields," *NeuroImage*, vol. 89, pp. 216–225, Apr. 2014.
- [13] M. Fernández-Corazza, S. Turovets, P. Luu, and D. Tucker, "Optimization in transcranial electrical neuromodulation based on the reciprocity principle," *Brain Stimulation*, vol. 8, no. 2, p. 403, Mar. 2015.
- [14] M. Fernández-Corazza, S. Turovets, and C. H. Muravchik, "Unification of optimal targeting methods in transcranial electrical stimulation," *NeuroImage*, vol. 209, p. 116 403, Apr. 2020.
- [15] S. Wagner, F. Lucka, J. Vorwerk, C. Herrmann, G. Nolte, M. Burger, and C. Wolters, "Using reciprocity for relating the simulation of transcranial current stimulation to the EEG forward problem," *NeuroImage*, vol. 140, pp. 163–173, Oct. 2016.
- [16] P. Riitta Hari MD and P. Aina Puce, *MEG-EEG Primer*. Oxford University Press, Mar. 2017.
- [17] D. Purves, G. J. Augustine, D. Fitzpatrick, W. C. Hall, A.-S. Lamantia, R. Mooney, and L. E. White, Eds., *Neuroscience*, en, 6th ed. Sinauer Associates, Jan. 2018.
- [18] I. Jocks, *The compositiones medicamentorum of scribonius largus*, 2013.
- [19] M. Piccolino, "Animal electricity and the birth of electrophysiology: The legacy of luigi galvani," *Brain Research Bulletin*, vol. 46, no. 5, pp. 381–407, Jul. 1998.
- [20] A. Parent, "Giovanni Aldini: From animal electricity to human brain stimulation," *Canadian Journal of Neurological Sciences / Journal Canadien des Sciences Neurologiques*, vol. 31, no. 4, pp. 576–584, Nov. 2004.
- [21] A. Priori, "Brain polarization in humans: A reappraisal of an old tool for prolonged non-invasive modulation of brain excitability," *Clinical Neurophysiology*, vol. 114, no. 4, pp. 589–595, Apr. 2003.
- [22] O. D. Creutzfeldt, G. H. Fromm, and H. Kapp, "Influence of transcor-tical d-c currents on cortical neuronal activity," *Experimental Neurology*, vol. 5, no. 6, pp. 436–452, Jun. 1962.
- [23] D. P. Purpura and J. G. McMurtry, "INTRACELLULAR ACTIVITIES AND EVOKED POTENTIAL CHANGES DURING POLARIZATION OF MOTOR CORTEX," *Journal of Neurophysiology*, vol. 28, no. 1, pp. 166–185, Jan. 1965.
- [24] L. J. Bindman, O. C. J. Lippold, and J. W. T. Redfearn, "The action of brief polarizing currents on the cerebral cortex of the rat (1) during current flow and (2) in the production of long-lasting after-effects," *The Journal of Physiology*, vol. 172, no. 3, pp. 369–382, Aug. 1964.

- [25] Z. Esmaeilpour, P. Schestatsky, M. Bikson, A. R. Brunoni, A. Pellegrinelli, F. X. Piovesan, M. M. S. A. Santos, R. B. Menezes, and F. Fregni, "Notes on human trials of transcranial direct current stimulation between 1960 and 1998," *Frontiers in Human Neuroscience*, vol. 11, Feb. 2017.
- [26] O. C. J. Lippold and J. W. T. Redfearn, "Mental changes resulting from the passage of small direct currents through the human brain," *British Journal of Psychiatry*, vol. 110, no. 469, pp. 768–772, Nov. 1964.
- [27] M. W. P. Carney, M. D. Cashman, and B. F. Sheffield, "Polarization in depression," *British Journal of Psychiatry*, vol. 117, no. 539, pp. 474–475, Oct. 1970.
- [28] A. P. Baker, "Brain stem polarization in the treatment of depression," *S. Afr. Med. J.*, vol. 44, no. 16, pp. 473–475, Apr. 1970.
- [29] S. C. Rosen and J. S. Stamm, "Transcortical polarization: Facilitation of delayed response performance by monkeys," *Experimental Neurology*, vol. 35, no. 2, pp. 282–289, May 1972.
- [30] D. Albert, "The effects of polarizing currents on the consolidation of learning," *Neuropsychologia*, vol. 4, no. 1, pp. 65–77, Feb. 1966.
- [31] F. Szeligo, "Electrophysiological and behavioral effects of transcortical polarizing current: Comparison with the behaviorally determined characteristics of learning," *Brain Research*, vol. 103, no. 3, pp. 463–475, Feb. 1976.
- [32] A. Priori, A. Berardelli, S. Rona, N. Accornero, and M. Manfredi, "Polarization of the human motor cortex through the scalp," *NeuroReport*, vol. 9, no. 10, pp. 2257–2260, Jul. 1998.
- [33] C. J. Stagg and M. A. Nitsche, "Physiological basis of transcranial direct current stimulation," *The Neuroscientist*, vol. 17, no. 1, pp. 37–53, Feb. 2011.
- [34] A. V. Peterchev, T. A. Wagner, P. C. Miranda, M. A. Nitsche, W. Paulus, S. H. Lisanby, A. Pascual-Leone, and M. Bikson, "Fundamentals of transcranial electric and magnetic stimulation dose: Definition, selection, and reporting practices," *Brain Stimulation*, vol. 5, no. 4, pp. 435–453, Oct. 2012.
- [35] H. Knotkova, M. A. Nitsche, M. Bikson, and A. J. Woods, Eds., *Practical guide to transcranial direct current stimulation*, 1st ed. Springer International Publishing, Feb. 2019.
- [36] A. F. DaSilva, M. S. Volz, M. Bikson, and F. Fregni, "Electrode positioning and montage in transcranial direct current stimulation," *Journal of Visualized Experiments*, no. 51, May 2011.
- [37] T. Furubayashi, Y. Terao, N. Arai, S. Okabe, H. Mochizuki, R. Hanajima, M. Hamada, A. Yugeta, S. Inomata-Terada, and Y. Ugawa, "Short and long duration transcranial direct current stimulation (tDCS) over the human hand motor area," *Experimental Brain Research*, vol. 185, no. 2, pp. 279–286, Oct. 2008.

- [38] G. Kronberg and M. Bikson, "Electrode assembly design for transcranial direct current stimulation: A FEM modeling study," in *2012 Annual International Conference of the IEEE Engineering in Medicine and Biology Society*, IEEE, Aug. 2012.
- [39] M. A. Nitsche, S. Doemkes, T. Karaköse, A. Antal, D. Liebetanz, N. Lang, F. Tergau, and W. Paulus, "Shaping the effects of transcranial direct current stimulation of the human motor cortex," *Journal of Neurophysiology*, vol. 97, no. 4, pp. 3109–3117, Apr. 2007.
- [40] M. A. Nitsche, M. S. Nitsche, C. C. Klein, F. Tergau, J. C. Rothwell, and W. Paulus, "Level of action of cathodal DC polarisation induced inhibition of the human motor cortex," *Clinical Neurophysiology*, vol. 114, no. 4, pp. 600–604, Apr. 2003.
- [41] M. A. Nitsche and W. Paulus, "Sustained excitability elevations induced by transcranial DC motor cortex stimulation in humans," *Neurology*, vol. 57, no. 10, pp. 1899–1901, Nov. 2001.
- [42] M. A. Nitsche, A. Seeber, K. Frommann, C. C. Klein, C. Rochford, M. S. Nitsche, K. Fricke, D. Liebetanz, N. Lang, A. Antal, W. Paulus, and F. Tergau, "Modulating parameters of excitability during and after transcranial direct current stimulation of the human motor cortex," *The Journal of Physiology*, vol. 568, no. 1, pp. 291–303, Sep. 2005.
- [43] S. Wiethoff, M. Hamada, and J. C. Rothwell, "Variability in response to transcranial direct current stimulation of the motor cortex," *Brain Stimulation*, vol. 7, no. 3, pp. 468–475, May 2014.
- [44] V. López-Alonso, B. Cheeran, D. Rio-Rodríguez, and M. Fernández-del-Olmo, "Inter-individual variability in response to non-invasive brain stimulation paradigms," *Brain Stimulation*, vol. 7, no. 3, pp. 372–380, May 2014.
- [45] K. Monte-Silva, M.-F. Kuo, S. Hessenthaler, S. Fresnoza, D. Liebetanz, W. Paulus, and M. A. Nitsche, "Induction of late LTP-like plasticity in the human motor cortex by repeated non-invasive brain stimulation," *Brain stimulation*, vol. 6, no. 3, pp. 424–432, May 2013.
- [46] M. A. Nitsche, L. G. Cohen, E. M. Wassermann, A. Priori, N. Lang, A. Antal, W. Paulus, F. Hummel, P. S. Boggio, F. Fregni, and A. Pascual-Leone, "Transcranial direct current stimulation: State of the art 2008," *Brain Stimulation*, vol. 1, no. 3, pp. 206–223, Jul. 2008.
- [47] L. Marshall, H. Helgadóttir, M. Mölle, and J. Born, "Boosting slow oscillations during sleep potentiates memory," *Nature*, vol. 444, no. 7119, pp. 610–613, Nov. 2006.
- [48] S. Groppa, T. Bergmann, C. Siems, M. Mölle, L. Marshall, and H. Siebner, "Slow-oscillatory transcranial direct current stimulation can induce bidirectional shifts in motor cortical excitability in awake humans," *Neuroscience*, vol. 166, no. 4, pp. 1219–1225, Apr. 2010.

- [49] A. Antal, K. Boros, C. Poreisz, L. Chaieb, D. Terney, and W. Paulus, "Comparatively weak after-effects of transcranial alternating current stimulation (tACS) on cortical excitability in humans," *Brain Stimulation*, vol. 1, no. 2, pp. 97–105, Apr. 2008.
- [50] T. Zaehle, S. Rach, and C. S. Herrmann, "Transcranial alternating current stimulation enhances individual alpha activity in human EEG," *PLoS ONE*, vol. 5, no. 11, A. Aleman, Ed., e13766, Nov. 2010.
- [51] D. Terney, L. Chaieb, V. Moliadze, A. Antal, and W. Paulus, "Increasing human brain excitability by transcranial high-frequency random noise stimulation," *Journal of Neuroscience*, vol. 28, no. 52, pp. 14 147–14 155, Dec. 2008.
- [52] M. Cappelletti, E. Gessaroli, R. Hithersay, M. Mitolo, D. Didino, R. Kanai, R. C. Kadosh, and V. Walsh, "Transfer of cognitive training across magnitude dimensions achieved with concurrent brain stimulation of the parietal lobe," *Journal of Neuroscience*, vol. 33, no. 37, pp. 14 899–14 907, Sep. 2013.
- [53] P. C. Miranda, M. Lomarev, and M. Hallett, "Modeling the current distribution during transcranial direct current stimulation," *Clinical Neurophysiology*, vol. 117, no. 7, pp. 1623–1629, Jul. 2006.
- [54] A. Rahman, D. Reato, M. Arlotti, F. Gasca, A. Datta, L. C. Parra, and M. Bikson, "Cellular effects of acute direct current stimulation: Somatic and synaptic terminal effects," *The Journal of Physiology*, vol. 591, no. 10, pp. 2563–2578, Apr. 2013.
- [55] T. Wagner, F. Fregni, S. Fecteau, A. Grodzinsky, M. Zahn, and A. Pascual-Leone, "Transcranial direct current stimulation: A computer-based human model study," *NeuroImage*, vol. 35, no. 3, pp. 1113–1124, Apr. 2007.
- [56] P. Elliott, "Electricity and the brain," in *The Stimulated Brain*, Elsevier, 2014, pp. 3–33.
- [57] T. Radman, R. L. Ramos, J. C. Brumberg, and M. Bikson, "Role of cortical cell type and morphology in subthreshold and suprathreshold uniform electric field stimulation in vitro," *Brain Stimulation*, vol. 2, no. 4, 215–228.e3, Oct. 2009.
- [58] S. Zaghi, M. Acar, B. Hultgren, P. S. Boggio, and F. Fregni, "Noninvasive brain stimulation with low-intensity electrical currents: Putative mechanisms of action for direct and alternating current stimulation," *The Neuroscientist*, vol. 16, no. 3, pp. 285–307, Dec. 2010.
- [59] E. M. Wassermann and J. Grafman, "Recharging cognition with DC brain polarization," *Trends in Cognitive Sciences*, vol. 9, no. 11, pp. 503–505, Nov. 2005.
- [60] M. A. Nitsche, "Catecholaminergic consolidation of motor cortical neuroplasticity in humans," *Cerebral Cortex*, vol. 14, no. 11, pp. 1240–1245, May 2004.

- [61] A. Barker, R. Jalinous, and I. Freeston, "Non-invasive magnetic stimulation of human motor cortex," *The Lancet*, vol. 325, no. 8437, pp. 1106–1107, May 1985.
- [62] A. Priori, F. Mameli, F. Cogiamanian, S. Marceglia, M. Tiriticco, S. Mrakic-Sposta, R. Ferrucci, S. Zago, D. Polezzi, and G. Sartori, "Lie-specific involvement of dorsolateral prefrontal cortex in deception," *Cerebral Cortex*, vol. 18, no. 2, pp. 451–455, Jun. 2008.
- [63] A. Dieckhöfer, T. D. Waberski, M. Nitsche, W. Paulus, H. Buchner, and R. Gobbelé, "Transcranial direct current stimulation applied over the somatosensory cortex – differential effect on low and high frequency SEPs," *Clinical Neurophysiology*, vol. 117, no. 10, pp. 2221–2227, Oct. 2006.
- [64] K. Sugawara, H. Onishi, K. Yamashiro, S. Kojima, S. Miyaguchi, H. Kirimoto, A. Tsubaki, H. Tamaki, H. Shirozu, and S. Kameyama, "The effect of anodal transcranial direct current stimulation over the primary motor or somatosensory cortices on somatosensory evoked magnetic fields," *Clinical Neurophysiology*, vol. 126, no. 1, pp. 60–67, Jan. 2015.
- [65] S. Kojima, H. Onishi, S. Miyaguchi, S. Kotan, K. Sugawara, H. Kirimoto, and H. Tamaki, "Effects of cathodal transcranial direct current stimulation to primary somatosensory cortex on short-latency afferent inhibition," *NeuroReport*, vol. 26, no. 11, pp. 634–637, Aug. 2015.
- [66] Y. Wang, Y. Hao, J. Zhou, P. J. Fried, X. Wang, J. Zhang, J. Fang, A. Pascual-Leone, and B. Manor, "Direct current stimulation over the human sensorimotor cortex modulates the brain's hemodynamic response to tactile stimulation," *European Journal of Neuroscience*, vol. 42, no. 3, pp. 1933–1940, Jun. 2015.
- [67] L. Grundmann, R. Rolke, M. A. Nitsche, G. Pavlakovic, S. Happe, R.-D. Treede, W. Paulus, and C. G. Bachmann, "Effects of transcranial direct current stimulation of the primary sensory cortex on somatosensory perception," *Brain Stimulation*, vol. 4, no. 4, pp. 253–260, Oct. 2011.
- [68] R. Rehmman, M. Sczesny-Kaiser, M. Lenz, T. Gučia, A. Schliesing, P. Schwenkreis, M. Tegenthoff, and O. Höffken, "Polarity-specific cortical effects of transcranial direct current stimulation in primary somatosensory cortex of healthy humans," *Frontiers in Human Neuroscience*, vol. 10, May 2016.
- [69] S. Song, M. Sandrini, and L. G. Cohen, "Modifying somatosensory processing with non-invasive brain stimulation," *Restorative Neurology and Neuroscience*, vol. 29, no. 6, pp. 427–437, 2011.
- [70] K. Matsunaga, "Effect of transcranial DC sensorimotor cortex stimulation on somatosensory evoked potentials in humans," *Clinical Neurophysiology*, vol. 115, no. 2, pp. 456–460, Feb. 2004.

- [71] J. Huttunen, S. Komssi, and L. Lauronen, "Spatial dynamics of population activities at s1 after median and ulnar nerve stimulation revisited: An MEG study," *NeuroImage*, vol. 32, no. 3, pp. 1024–1031, Sep. 2006.
- [72] F. Mauguière and L. Garcia-Larrea, *Somatosensory and Pain Evoked Potentials*, D. L. Schomer and F. H. L. da Silva, Eds. Oxford University Press, Nov. 2017.
- [73] B. Paneri, D. Adair, C. Thomas, N. Khadka, V. Patel, W. J. Tyler, L. Parra, and M. Bikson, "Tolerability of repeated application of transcranial electrical stimulation with limited outputs to healthy subjects," *Brain Stimulation*, vol. 9, no. 5, pp. 740–754, Sep. 2016.
- [74] P. C. Gandiga, F. C. Hummel, and L. G. Cohen, "Transcranial DC stimulation (tDCS): A tool for double-blind sham-controlled clinical studies in brain stimulation," *Clinical Neurophysiology*, vol. 117, no. 4, pp. 845–850, Apr. 2006.
- [75] D. Wallace, N. R. Cooper, S. Paulmann, P. B. Fitzgerald, and R. Russo, "Perceived comfort and blinding efficacy in randomised sham-controlled transcranial direct current stimulation (tDCS) trials at 2 mA in young and older healthy adults," *PLOS ONE*, vol. 11, no. 2, F. Tremblay, Ed., e0149703, Feb. 2016.
- [76] M. A. Nitsche, M. S. Nitsche, C. C. Klein, F. Tergau, J. C. Rothwell, and W. Paulus, "Level of action of cathodal DC polarisation induced inhibition of the human motor cortex," *Clinical Neurophysiology*, vol. 114, no. 4, pp. 600–604, Apr. 2003.
- [77] A. Opitz, W. Paulus, S. Will, A. Antunes, and A. Thielscher, "Determinants of the electric field during transcranial direct current stimulation," *NeuroImage*, vol. 109, pp. 140–150, Apr. 2015.
- [78] Z. Turi, G. G. Ambrus, K.-A. Ho, T. Sengupta, W. Paulus, and A. Antal, "When size matters: Large electrodes induce greater stimulation-related cutaneous discomfort than smaller electrodes at equivalent current density," *Brain Stimulation*, vol. 7, no. 3, pp. 460–467, May 2014.
- [79] M. Parazzini, E. Rossi, R. Ferrucci, I. Liorni, A. Priori, and P. Ravazzani, "Modelling the electric field and the current density generated by cerebellar transcranial DC stimulation in humans," *Clinical Neurophysiology*, vol. 125, no. 3, pp. 577–584, Mar. 2014.
- [80] E. R. Buch, E. Santarnecchi, A. Antal, J. Born, P. A. Celnik, J. Classen, C. Gerloff, M. Hallett, F. C. Hummel, M. A. Nitsche, A. Pascual-Leone, W. J. Paulus, J. Reis, E. M. Robertson, J. C. Rothwell, M. Sandrini, H. M. Schambra, E. M. Wassermann, U. Ziemann, and L. G. Cohen, "Effects of tDCS on motor learning and memory formation: A consensus and critical position paper," *Clinical Neurophysiology*, vol. 128, no. 4, pp. 589–603, Apr. 2017.

- [81] S. Kim, M. C. Stephenson, P. G. Morris, and S. R. Jackson, "tDCS-induced alterations in GABA concentration within primary motor cortex predict motor learning and motor memory: A 7t magnetic resonance spectroscopy study," *NeuroImage*, vol. 99, pp. 237–243, Oct. 2014.
- [82] G. Kronberg, M. Bridi, T. Abel, M. Bikson, and L. C. Parra, "Direct current stimulation modulates LTP and LTD: Activity dependence and dendritic effects," *Brain Stimulation*, vol. 10, no. 1, pp. 51–58, Jan. 2017.
- [83] A. R. Brunoni, M. A. Nitsche, N. Bolognini, M. Bikson, T. Wagner, L. Merabet, D. J. Edwards, A. Valero-Cabre, A. Rotenberg, A. Pascual-Leone, R. Ferrucci, A. Priori, P. S. Boggio, and F. Fregni, "Clinical research with transcranial direct current stimulation (tDCS): Challenges and future directions," *Brain Stimulation*, vol. 5, no. 3, pp. 175–195, Jul. 2012.
- [84] S. Furuya, M. A. Nitsche, W. Paulus, and E. Altenmüller, "Surmounting retraining limits in musicians' dystonia by transcranial stimulation," *Annals of Neurology*, vol. 75, no. 5, pp. 700–707, May 2014.
- [85] J.-P. Lefaucheur, A. Antal, S. S. Ayache, D. H. Benninger, J. Brunelin, F. Cogiamanian, M. Cotelli, D. D. Ridder, R. Ferrucci, B. Langguth, P. Marangolo, V. Mylius, M. A. Nitsche, F. Padberg, U. Palm, E. Poulet, A. Priori, S. Rossi, M. Schecklmann, S. Vanneste, U. Ziemann, L. Garcia-Larrea, and W. Paulus, "Evidence-based guidelines on the therapeutic use of transcranial direct current stimulation (tDCS)," *Clinical Neurophysiology*, vol. 128, no. 1, pp. 56–92, Jan. 2017.
- [86] A. Naro, D. Milardi, M. Russo, C. Terranova, V. Rizzo, A. Cacciola, S. Marino, R. S. Calabro, and A. Quartarone, "Non-invasive brain stimulation, a tool to revert maladaptive plasticity in neuropathic pain," *Frontiers in Human Neuroscience*, vol. 10, Jul. 2016.
- [87] P. S. Boggio, L. P. Khoury, D. C. S. Martins, O. E. M. S. Martins, E. C. de Macedo, and F. Fregni, "Temporal cortex direct current stimulation enhances performance on a visual recognition memory task in alzheimer disease," *Journal of Neurology, Neurosurgery & Psychiatry*, vol. 80, no. 4, pp. 444–447, Dec. 2009.
- [88] R. Ferrucci, M. Bortolomasi, M. Vergari, L. Tadini, B. Salvaro, M. Giacomuzzi, S. Barbieri, and A. Priori, "Transcranial direct current stimulation in severe, drug-resistant major depression," *Journal of Affective Disorders*, vol. 118, no. 1-3, pp. 215–219, Nov. 2009.
- [89] G. Schlaug, V. Renga, and D. Nair, "Transcranial direct current stimulation in stroke recovery," *Archives of Neurology*, vol. 65, no. 12, Dec. 2008.
- [90] P. S. Boggio, S. Zaghi, M. Lopes, and F. Fregni, "Modulatory effects of anodal transcranial direct current stimulation on perception and pain thresholds in healthy volunteers," *European Journal of Neurology*, vol. 15, no. 10, pp. 1124–1130, Aug. 2008.

- [91] B. W. Fenton, P. A. Palmieri, P. Boggio, J. Fanning, and F. Fregni, "A preliminary study of transcranial direct current stimulation for the treatment of refractory chronic pelvic pain," *Brain Stimulation*, vol. 2, no. 2, pp. 103–107, Apr. 2009.
- [92] F. Fregni, R. Marcondes, P. S. Boggio, M. A. Marcolin, S. P. Rigonatti, T. G. Sanchez, M. A. Nitsche, and A. Pascual-Leone, "Transient tinnitus suppression induced by repetitive transcranial magnetic stimulation and transcranial direct current stimulation," *European Journal of Neurology*, vol. 13, no. 9, pp. 996–1001, Sep. 2006.
- [93] L. Gabis, B. Shklar, Y. Baruch, R. Raz, E. Gabis, and D. Geva, "Pain reduction using transcranial electrostimulation: A double blind "active placebo" controlled trial," *Journal of Rehabilitation Medicine*, vol. 41, no. 4, pp. 256–261, 2009.
- [94] S. Zaghi, B. Thiele, D. Pimentel, T. Pimentel, and F. Fregni, "Assessment and treatment of pain with non-invasive cortical stimulation," *Restorative Neurology and Neuroscience*, vol. 29, no. 6, pp. 439–451, 2011.
- [95] V. F. Bueno, A. R. Brunoni, P. S. Boggio, I. M. Bensenor, and F. Fregni, "Mood and cognitive effects of transcranial direct current stimulation in post-stroke depression," *Neurocase*, vol. 17, no. 4, pp. 318–322, Aug. 2011.
- [96] U. G. Kalu, C. E. Sexton, C. K. Loo, and K. P. Ebmeier, "Transcranial direct current stimulation in the treatment of major depression: A meta-analysis," *Psychological Medicine*, vol. 42, no. 9, pp. 1791–1800, Jan. 2012.
- [97] J.-P. Lefaucheur, A. Antal, R. Ahdab, D. C. de Andrade, F. Fregni, E. M. Khedr, M. Nitsche, and W. Paulus, "The use of repetitive transcranial magnetic stimulation (rTMS) and transcranial direct current stimulation (tDCS) to relieve pain," *Brain Stimulation*, vol. 1, no. 4, pp. 337–344, Oct. 2008.
- [98] J. Nizard, J.-P. Lefaucheur, M. Helbert, E. de Chauvigny, and J.-P. Nguyen, "Non-invasive stimulation therapies for the treatment of refractory pain," *Discovery medicine*, vol. 14, no. 74, pp. 21–31, 2012.
- [99] A. F. DaSilva, M. E. Mendonca, S. Zaghi, M. Lopes, M. F. DosSantos, E. L. Spierings, Z. Bajwa, A. Datta, M. Bikson, and F. Fregni, "tDCS-induced analgesia and electrical fields in pain-related neural networks in chronic migraine," *Headache: The Journal of Head and Face Pain*, vol. 52, no. 8, pp. 1283–1295, Apr. 2012.
- [100] F. Fregni, P. S. Boggio, M. C. Lima, M. J. Ferreira, T. Wagner, S. P. Rigonatti, A. W. Castro, D. R. Souza, M. Riberto, S. D. Freedman, M. A. Nitsche, and A. Pascual-Leone, "A sham-controlled, phase II trial of transcranial direct current stimulation for the treatment of central pain in traumatic spinal cord injury," *Pain*, vol. 122, no. 1, pp. 197–209, May 2006.

- [101] T. Z. Kincses, A. Antal, M. A. Nitsche, O. Bártfai, and W. Paulus, "Facilitation of probabilistic classification learning by transcranial direct current stimulation of the prefrontal cortex in the human," *Neuropsychologia*, vol. 42, no. 1, pp. 113–117, Jan. 2004.
- [102] J. M. Galea and P. Celnik, "Brain polarization enhances the formation and retention of motor memories," *Journal of Neurophysiology*, vol. 102, no. 1, pp. 294–301, Jul. 2009.
- [103] P. G. Mulquiney, K. E. Hoy, Z. J. Daskalakis, and P. B. Fitzgerald, "Improving working memory: Exploring the effect of transcranial random noise stimulation and transcranial direct current stimulation on the dorsolateral prefrontal cortex," *Clinical Neurophysiology*, vol. 122, no. 12, pp. 2384–2389, Dec. 2011.
- [104] S. H. Ohn, C.-I. Park, W.-K. Yoo, M.-H. Ko, K. P. Choi, G.-M. Kim, Y. T. Lee, and Y.-H. Kim, "Time-dependent effect of transcranial direct current stimulation on the enhancement of working memory," *NeuroReport*, vol. 19, no. 1, pp. 43–47, Jan. 2008.
- [105] P. S. Boggio, F. Fregni, C. Valasek, S. Ellwood, R. Chi, J. Gallate, A. Pascual-Leone, and A. Snyder, "Temporal lobe cortical electrical stimulation during the encoding and retrieval phase reduces false memories," *PLoS ONE*, vol. 4, no. 3, B. Baune, Ed., e4959, Mar. 2009.
- [106] R. P. Chi, F. Fregni, and A. W. Snyder, "Visual memory improved by non-invasive brain stimulation," *Brain Research*, vol. 1353, pp. 168–175, Sep. 2010.
- [107] M. F. Bear, B. W. Connors, and M. A. Paradiso, *Neuroscience*, 4th ed. Philadelphia, PA: Lippincott Williams and Wilkins, Feb. 2015.
- [108] G. D. Dawson, "CEREBRAL RESPONSES TO ELECTRICAL STIMULATION OF PERIPHERAL NERVE IN MAN," *Journal of Neurology, Neurosurgery & Psychiatry*, vol. 10, no. 3, pp. 134–140, Aug. 1947.
- [109] G. Cruccu, M. Aminoff, G. Curio, J. Guerit, R. Kakigi, F. Mauguiere, P. Rossini, R.-D. Treede, and L. Garcia-Larrea, "Recommendations for the clinical use of somatosensory-evoked potentials," *Clinical Neurophysiology*, vol. 119, no. 8, pp. 1705–1719, Aug. 2008.
- [110] A. Nakamura, T. Yamada, A. Goto, T. Kato, K. Ito, Y. Abe, T. Kachi, and R. Kakigi, "Somatosensory homunculus as drawn by MEG," *NeuroImage*, vol. 7, no. 4, pp. 377–386, May 1998.
- [111] C. C. Wood, D. Cohen, B. N. Cuffin, M. Yarita, and T. Allison, "Electrical sources in human somatosensory cortex: Identification by combined magnetic and potential recordings," *Science*, vol. 227, no. 4690, pp. 1051–1053, Mar. 1985.
- [112] R. W. Brown, Y.-C. N. Cheng, E. M. Haacke, M. R. Thompson, and R. Venkatesan, Eds., *Magnetic Resonance Imaging*. John Wiley & Sons Ltd, Apr. 2014.

- [113] D. S. Tuch, V. J. Wedeen, A. M. Dale, J. S. George, and J. W. Belliveau, "Conductivity tensor mapping of the human brain using diffusion tensor MRI," *Proceedings of the National Academy of Sciences*, vol. 98, no. 20, pp. 11 697–11 701, Sep. 2001.
- [114] M. Hämäläinen, R. Hari, R. J. Ilmoniemi, J. Knuutila, and O. V. Lounasmaa, "Magnetoencephalography—theory, instrumentation, and applications to noninvasive studies of the working human brain," *Reviews of Modern Physics*, vol. 65, no. 2, pp. 413–497, Apr. 1993.
- [115] Y. Huang, A. A. Liu, B. Lafon, D. Friedman, M. Dayan, X. Wang, M. Bikson, W. K. Doyle, O. Devinsky, and L. C. Parra, "Measurements and models of electric fields in the in vivo human brain during transcranial electric stimulation," *eLife*, vol. 6, Feb. 2017.
- [116] G. Dassios, A. S. Fokas, and D. Hadjiloizi, "On the complementarity of electroencephalography and magnetoencephalography," *Inverse Problems*, vol. 23, no. 6, pp. 2541–2549, Nov. 2007.
- [117] J. Haueisen, M. Funke, D. Güllmar, and R. Eichardt, "Tangential and radial epileptic spike activity," *Journal of Clinical Neurophysiology*, vol. 29, no. 4, pp. 327–332, Aug. 2012.
- [118] R. Brette and A. Destexhe, Eds., *Handbook of Neural Activity Measurement*. Cambridge University Press, 2009.
- [119] H. Buchner, M. Fuchs, H. -A. Wischmann, O. Dssel, I. Ludwig, A. Knepper, and P. Berg, "Source analysis of median nerve and finger stimulated somatosensory evoked potentials: Multichannel simultaneous recording of electric and magnetic fields combined with 3d-MR tomography," *Brain Topography*, vol. 6, no. 4, pp. 299–310, Jun. 1994.
- [120] M. Fuchs, M. Wagner, H.-A. Wischmann, T. Köhler, A. Theißen, R. Drenckhahn, and H. Buchner, "Improving source reconstructions by combining bioelectric and biomagnetic data," *Electroencephalography and Clinical Neurophysiology*, vol. 107, no. 2, pp. 93–111, Apr. 1998.
- [121] H. Onishi, K. Sugawara, K. Yamashiro, D. Sato, M. Suzuki, H. Kirimoto, H. Tamaki, H. Murakami, and S. Kameyama, "Effect of the number of pins and inter-pin distance on somatosensory evoked magnetic fields following mechanical tactile stimulation," *Brain Research*, vol. 1535, pp. 78–88, Oct. 2013.
- [122] J. Vorwerk, J.-H. Cho, S. Rampp, H. Hamer, T. R. Knösche, and C. H. Wolters, "A guideline for head volume conductor modeling in EEG and MEG," *NeuroImage*, vol. 100, pp. 590–607, Oct. 2014.
- [123] Ü. Aydin, J. Vorwerk, P. Küpper, M. Heers, H. Kugel, A. Galka, L. Hamid, J. Wellmer, C. Kellinghaus, S. Rampp, and C. H. Wolters, "Combining EEG and MEG for the reconstruction of epileptic activity using a calibrated realistic volume conductor model," *PLoS ONE*, vol. 9, no. 3, G. R. Barnes, Ed., e93154, Mar. 2014.

- [124] M.-X. Huang, T. Song, D. J. Hagler, I. Podgorny, V. Jousmaki, L. Cui, K. Gaa, D. L. Harrington, A. M. Dale, R. R. Lee, J. Elman, and E. Halgren, "A novel integrated MEG and EEG analysis method for dipolar sources," *NeuroImage*, vol. 37, no. 3, pp. 731–748, Sep. 2007.
- [125] E. C. Morales, C. D. Acosta-Medina, G. Castellanos-Dominguez, and D. Mantini, "A finite-difference solution for the EEG forward problem in inhomogeneous anisotropic media," *Brain Topography*, vol. 32, no. 2, pp. 229–239, Oct. 2019.
- [126] L. Ruthotto, H. Kugel, J. Olesch, B. Fischer, J. Modersitzki, M. Burger, and C. H. Wolters, "Diffeomorphic susceptibility artifact correction of diffusion-weighted magnetic resonance images," *Physics in Medicine and Biology*, vol. 57, no. 18, pp. 5715–5731, Sep. 2012.
- [127] N. Lynnerup, J. G. Astrup, and B. Sejrsen, "Thickness of the human cranial diploe in relation to age, sex and general body build," *Head & Face Medicine*, vol. 1, no. 1, Dec. 2005.
- [128] M. Dannhauer, B. Lanfer, C. H. Wolters, and T. R. Knösche, "Modeling of the human skull in EEG source analysis," *Human Brain Mapping*, vol. 32, no. 9, pp. 1383–1399, Aug. 2011.
- [129] S. van den Broek, F. Reinders, M. Donderwinkel, and M. Peters, "Volume conduction effects in EEG and MEG," *Electroencephalography and Clinical Neurophysiology*, vol. 106, no. 6, pp. 522–534, Jun. 1998.
- [130] G. Marin, C. Guerin, S. Baillet, L. Garnero, and G. Meunier, "Influence of skull anisotropy for the forward and inverse problem in EEG: Simulation studies using FEM on realistic head models," *Human Brain Mapping*, vol. 6, no. 4, pp. 250–269, 1998.
- [131] H. Hallez, B. Vanrumste, P. V. Hese, S. Delputte, and I. Lemahieu, "Dipole estimation errors due to differences in modeling anisotropic conductivities in realistic head models for EEG source analysis," *Physics in Medicine and Biology*, vol. 53, no. 7, pp. 1877–1894, Mar. 2008.
- [132] O. Steinsträter, S. Sillekens, M. Junghoefer, M. Burger, and C. H. Wolters, "Sensitivity of beamformer source analysis to deficiencies in forward modeling," *Human Brain Mapping*, vol. 31, no. 12, pp. 1907–1927, May 2010.
- [133] V. Montes-Restrepo, P. van Mierlo, G. Strobbe, S. Staelens, S. Vandenberghe, and H. Hallez, "Influence of skull modeling approaches on EEG source localization," *Brain Topography*, vol. 27, no. 1, pp. 95–111, Sep. 2014.
- [134] S. Goncalves, J. de Munck, J. Verbunt, F. Bijma, R. Heethaar, and F. L. da Silva, "In vivo measurement of the brain and skull resistivities using an eit-based method and realistic models for the head," *IEEE Transactions on Biomedical Engineering*, vol. 50, no. 6, pp. 754–767, Jun. 2003.

- [135] N. Gao, S. A. Zhu, and B. He, "A new magnetic resonance electrical impedance tomography (MREIT) algorithm: The RSM-MREIT algorithm with applications to estimation of human head conductivity," *Physics in Medicine and Biology*, vol. 51, no. 12, pp. 3067–3083, May 2006.
- [136] X. Li, K. Yu, and B. He, "Magnetoacoustic tomography with magnetic induction (MAT-MI) for imaging electrical conductivity of biological tissue: A tutorial review," *Physics in Medicine and Biology*, vol. 61, no. 18, R249–R270, Aug. 2016.
- [137] R. Hoekema, G. Wieneke, F. Leijten, C. van Veelen, P. van Rijen, G. Huiskamp, J. Ansems, and A. van Huffelen, *Brain Topography*, vol. 16, no. 1, pp. 29–38, 2003.
- [138] R. Plonsey and D. B. Heppner, "Considerations of quasi-stationarity in electrophysiological systems," *The Bulletin of Mathematical Biophysics*, vol. 29, no. 4, pp. 657–664, Dec. 1967.
- [139] C. Wolters, A. Anwander, G. Berti, and U. Hartmann, "Geometry-adapted hexahedral meshes improve accuracy of finite-element-method-based EEG source analysis," *IEEE Transactions on Biomedical Engineering*, vol. 54, no. 8, pp. 1446–1453, Aug. 2007.
- [140] J. Mosher, P. Lewis, and R. Leahy, "Multiple dipole modeling and localization from spatio-temporal MEG data," *IEEE Transactions on Biomedical Engineering*, vol. 39, no. 6, pp. 541–557, Jun. 1992.
- [141] M. Huang, C. Aine, S. Supek, E. Best, D. Ranken, and E. Flynn, "Multi-start downhill simplex method for spatio-temporal source localization in magnetoencephalography," *Electroencephalography and Clinical Neurophysiology/Evoked Potentials Section*, vol. 108, no. 1, pp. 32–44, Jan. 1998.
- [142] C. M. Michel, M. M. Murray, G. Lantz, S. Gonzalez, L. Spinelli, and R. G. de Peralta, "EEG source imaging," *Clinical Neurophysiology*, vol. 115, no. 10, pp. 2195–2222, Oct. 2004.
- [143] T. Bast, T. Boppel, A. Rupp, I. Harting, K. Hoehstetter, S. Fauser, A. Schulze-Bonhage, D. Rating, and M. Scherg, "Noninvasive source localization of interictal EEG spikes: Effects of signal-to-noise ratio and averaging," *Journal of Clinical Neurophysiology*, vol. 23, no. 6, pp. 487–497, Dec. 2006.
- [144] J. Haueisen, C. Ramon, M. Eiselt, H. Brauer, and H. Nowak, "Influence of tissue resistivities on neuromagnetic fields and electric potentials studied with a finite element model of the head," *IEEE Transactions on Biomedical Engineering*, vol. 44, no. 8, pp. 727–735, 1997.
- [145] S. Vallaghe and M. Clerc, "A global sensitivity analysis of three- and four-layer EEG conductivity models," *IEEE Transactions on Biomedical Engineering*, vol. 56, no. 4, pp. 988–995, Apr. 2009.

- [146] S. Lew, D. D. Sliva, M.-s. Choe, P. E. Grant, Y. Okada, C. H. Wolters, and M. S. Hämäläinen, "Effects of sutures and fontanels on MEG and EEG source analysis in a realistic infant head model," *NeuroImage*, vol. 76, pp. 282–293, Aug. 2013.
- [147] C. H. Wolters, S. Lew, R. Macleod, and M. S. Hämäläinen, "Combined EEG/MEG source analysis using calibrated finite element head models," 2010.
- [148] K. Sekihara, S. Nagarajan, D. Poeppel, A. Marantz, and Y. Miyashita, "Reconstructing spatio-temporal activities of neural sources using an MEG vector beamformer technique," *IEEE Transactions on Biomedical Engineering*, vol. 48, no. 7, pp. 760–771, Jul. 2001.
- [149] H. Azizollahi, A. Aarabi, and F. Wallois, "Effects of uncertainty in head tissue conductivity and complexity on EEG forward modeling in neonates," *Human Brain Mapping*, vol. 37, no. 10, pp. 3604–3622, May 2016.
- [150] M. Antonakakis, S. Schrader, A. Wollbrink, R. Oostenveld, S. Rampp, J. Haueisen, and C. H. Wolters, "The effect of stimulation type, head modeling, and combined EEG and MEG on the source reconstruction of the somatosensory p20/n20 component," *Human Brain Mapping*, vol. 40, no. 17, pp. 5011–5028, Aug. 2019.
- [151] S. Murakami and Y. Okada, "Contributions of principal neocortical neurons to magnetoencephalography and electroencephalography signals," *The Journal of Physiology*, vol. 575, no. 3, pp. 925–936, Sep. 2006.
- [152] C. Wolters, A. Anwander, X. Tricoche, D. Weinstein, M. Koch, and R. MacLeod, "Influence of tissue conductivity anisotropy on EEG/MEG field and return current computation in a realistic head model: A simulation and visualization study using high-resolution finite element modeling," *NeuroImage*, vol. 30, no. 3, pp. 813–826, Apr. 2006.
- [153] K. A. Salayev, N. Nakasato, M. Ishitobi, H. Shamoto, A. Kanno, and K. Inuma, "Spike orientation may predict epileptogenic side across cerebral sulci containing the estimated equivalent dipole," *Clinical Neurophysiology*, vol. 117, no. 8, pp. 1836–1843, Aug. 2006.
- [154] M. Rullmann, A. Anwander, M. Dannhauer, S. Warfield, F. Duffy, and C. Wolters, "EEG source analysis of epileptiform activity using a 1 mm anisotropic hexahedra finite element head model," *NeuroImage*, vol. 44, no. 2, pp. 399–410, Jan. 2009.
- [155] H. Tarao, H. Kuisti, L. Korpinen, N. Hayashi, and K. Isaka, "Effects of tissue conductivity and electrode area on internal electric fields in a numerical human model for ELF contact current exposures," *Physics in Medicine and Biology*, vol. 57, no. 10, pp. 2981–2996, Apr. 2012.
- [156] M. D. Lucia, G. Parker, K. Embleton, J. Newton, and V. Walsh, "Diffusion tensor MRI-based estimation of the influence of brain tissue anisotropy on the effects of transcranial magnetic stimulation," *NeuroImage*, vol. 36, no. 4, pp. 1159–1170, Jul. 2007.

- [157] A. Thielscher, A. Opitz, and M. Windhoff, "Impact of the gyral geometry on the electric field induced by transcranial magnetic stimulation," *NeuroImage*, vol. 54, no. 1, pp. 234–243, Jan. 2011.
- [158] A. Datta, X. Zhou, Y. Su, L. C. Parra, and M. Bikson, "Validation of finite element model of transcranial electrical stimulation using scalp potentials: Implications for clinical dose," *Journal of Neural Engineering*, vol. 10, no. 3, p. 036 018, May 2013.
- [159] A. Opitz, N. Zafar, V. Bockermann, V. Rohde, and W. Paulus, "Validating computationally predicted TMS stimulation areas using direct electrical stimulation in patients with brain tumors near precentral regions," *NeuroImage: Clinical*, vol. 4, pp. 500–507, 2014.
- [160] V. D. Santis, X. L. Chen, I. Laakso, and A. Hirata, "An equivalent skin conductivity model for low-frequency magnetic field dosimetry," *Biomedical Physics & Engineering Express*, vol. 1, no. 1, p. 015 201, Jun. 2015.
- [161] V. D. Santis, X. L. Chen, S. Cruciani, T. Campi, and M. Feliziani, "A novel homogenization procedure to model the skin layers in LF numerical dosimetry," *Physics in Medicine and Biology*, vol. 61, no. 12, pp. 4402–4411, May 2016.
- [162] IT'IS Foundation, *Tissue properties database v4.0*, en, 2018.
- [163] S. Gabriel, R. W. Lau, and C. Gabriel, "The dielectric properties of biological tissues: II. measurements in the frequency range 10 Hz to 20 GHz," *Physics in Medicine and Biology*, vol. 41, no. 11, pp. 2251–2269, Nov. 1996.
- [164] T. Wagner, M. Zahn, A. Grodzinsky, and A. Pascual-Leone, "Three-dimensional head model simulation of transcranial magnetic stimulation," *IEEE Transactions on Biomedical Engineering*, vol. 51, no. 9, pp. 1586–1598, Sep. 2004.
- [165] T. Yamamoto and Y. Yamamoto, "Electrical properties of the epidermal stratum corneum," *Medical & Biological Engineering*, vol. 14, no. 2, pp. 151–158, Mar. 1976.
- [166] C. Gabriel, A. Peyman, and E. H. Grant, "Electrical conductivity of tissue at frequencies below 1 MHz," *Physics in Medicine and Biology*, vol. 54, no. 16, pp. 4863–4878, Jul. 2009.
- [167] J. Mosher, R. Leahy, and P. Lewis, "EEG and MEG: Forward solutions for inverse methods," *IEEE Transactions on Biomedical Engineering*, vol. 46, no. 3, pp. 245–259, Mar. 1999.
- [168] R. Grech, T. Cassar, J. Muscat, K. P. Camilleri, S. G. Fabri, M. Zervakis, P. Xanthopoulos, V. Sakkalis, and B. Vanrumste, "Review on solving the inverse problem in EEG source analysis," *Journal of NeuroEngineering and Rehabilitation*, vol. 5, no. 1, Nov. 2008.

- [169] C. Wolters, R. Beckmann, A. Rienäcker, and H. Buchner, "Comparing regularized and non-regularized nonlinear dipole fit methods: A study in a simulated sulcus structure," *Brain Topography*, vol. 12, no. 1, pp. 3–18, 1999.
- [170] J. C. de Munck, C. H. Wolters, and M. Clerc, "EEG and MEG: Forward modeling," in *Handbook of Neural Activity Measurement*, R. Brette and A. Destexhe, Eds., Cambridge University Press, pp. 192–256.
- [171] S. Pursiainen, J. Vorwerk, and C. H. Wolters, "Electroencephalography (EEG) forward modeling via H(div) finite element sources with focal interpolation," *Physics in Medicine and Biology*, vol. 61, no. 24, pp. 8502–8520, Nov. 2016.
- [172] C. H. Wolters, L. Grasedyck, and W. Hackbusch, "Efficient computation of lead field bases and influence matrix for the FEM-based EEG and MEG inverse problem," *Inverse Problems*, vol. 20, no. 4, pp. 1099–1116, May 2004.
- [173] D. L. Camacho, R. H. Hopper, G. M. Lin, and B. S. Myers, "An improved method for finite element mesh generation of geometrically complex structures with application to the skullbase," *Journal of Biomechanics*, vol. 30, no. 10, pp. 1067–1070, Oct. 1997.
- [174] F. Lucka, S. Pursiainen, M. Burger, and C. H. Wolters, "Hierarchical bayesian inference for the EEG inverse problem using realistic FE head models: Depth localization and source separation for focal primary currents," *NeuroImage*, vol. 61, no. 4, pp. 1364–1382, Jul. 2012.
- [175] C. M. Michel and B. He, "EEG source localization," in *Clinical Neurophysiology: Basis and Technical Aspects*, Elsevier, 2019, pp. 85–101.
- [176] J. S. Ebersole and M. Wagner, "Relative yield of MEG and EEG spikes in simultaneous recordings," *Journal of Clinical Neurophysiology*, vol. 35, no. 6, pp. 443–453, Nov. 2018.
- [177] A. Antal, I. Alekseichuk, M. Bikson, J. Brockmöller, A. Brunoni, R. Chen, L. Cohen, G. Douthwaite, J. Ellrich, A. Flöel, F. Fregni, M. George, R. Hamilton, J. Haueisen, C. Herrmann, F. Hummel, J. Lefaucheur, D. Liebetanz, C. Loo, C. McCaig, C. Miniussi, P. Miranda, V. Moliadze, M. Nitsche, R. Nowak, F. Padberg, A. Pascual-Leone, W. Poppendieck, A. Priori, S. Rossi, P. Rossini, J. Rothwell, M. Rueger, G. Ruffini, K. Schellhorn, H. Siebner, Y. Ugawa, A. Wexler, U. Ziemann, M. Hallett, and W. Paulus, "Low intensity transcranial electric stimulation: Safety, ethical, legal regulatory and application guidelines," *Clinical Neurophysiology*, vol. 128, no. 9, pp. 1774–1809, Sep. 2017.
- [178] J.-P. Lefaucheur, "A comprehensive database of published tDCS clinical trials (2005–2016)," *Neurophysiologie Clinique/Clinical Neurophysiology*, vol. 46, no. 6, pp. 319–398, Dec. 2016.
- [179] D. J. Schutter and M. Wischniewski, "A meta-analytic study of exogenous oscillatory electric potentials in neuroenhancement," *Neuropsychologia*, vol. 86, pp. 110–118, Jun. 2016.

- [180] D. Veniero, C. S. Benwell, M. M. Ahrens, and G. Thut, "Inconsistent effects of parietal  $\alpha$ -tACS on pseudo neglect across two experiments: A failed internal replication," *Frontiers in Psychology*, vol. 8, Jun. 2017.
- [181] A. Antal, D. Keeser, A. Priori, F. Padberg, and M. Nitsche, "Conceptual and procedural shortcomings of the systematic review "evidence that transcranial direct current stimulation (tDCS) generates little-to-no reliable neurophysiologic effect beyond MEP amplitude modulation in healthy human subjects: A systematic review" by horvath and co-workers," *Brain Stimulation*, vol. 8, no. 4, pp. 846–849, Jul. 2015.
- [182] M. Antonakakis, S. Schrader, Ü. Aydin, A. Khan, J. Gross, M. Zervakis, S. Rapp, and C. H. Wolters, "Inter-subject variability of skull conductivity and thickness in calibrated realistic head models," *NeuroImage*, vol. 223, p. 117353, Dec. 2020.
- [183] S. Wagner, S. M. Rampersad, Ü. Aydin, J. Vorwerk, T. F. Oostendorp, T. Neuling, C. S. Herrmann, D. F. Stegeman, and C. H. Wolters, "Investigation of tDCS volume conduction effects in a highly realistic head model," *Journal of Neural Engineering*, vol. 11, no. 1, p. 016002, Dec. 2014.
- [184] I. Laakso, M. Mikkonen, S. Koyama, A. Hirata, and S. Tanaka, "Can electric fields explain inter-individual variability in transcranial direct current stimulation of the motor cortex?" *Scientific Reports*, vol. 9, no. 1, Jan. 2019.
- [185] T. D. Krieg, F. S. Salinas, S. Narayana, P. T. Fox, and D. J. Mogul, "PET-based confirmation of orientation sensitivity of TMS-induced cortical activation in humans," *Brain Stimulation*, vol. 6, no. 6, pp. 898–904, Nov. 2013.
- [186] T. D. Krieg, F. S. Salinas, S. Narayana, P. T. Fox, and D. J. Mogul, "Computational and experimental analysis of TMS-induced electric field vectors critical to neuronal activation," *Journal of Neural Engineering*, vol. 12, no. 4, p. 046014, Jun. 2015.
- [187] H. Seo and S. C. Jun, "Multi-scale computational models for electrical brain stimulation," *Frontiers in Human Neuroscience*, vol. 11, Oct. 2017.
- [188] S. Wagner, M. Burger, and C. H. Wolters, "An optimization approach for well-targeted transcranial direct current stimulation," *SIAM Journal on Applied Mathematics*, vol. 76, no. 6, pp. 2154–2174, Jan. 2016.
- [189] S. Guler, M. Dannhauer, B. Erem, R. Macleod, D. Tucker, S. Turovets, P. Luu, D. Erdogmus, and D. H. Brooks, "Optimization of focality and direction in dense electrode array transcranial direct current stimulation (tDCS)," *Journal of Neural Engineering*, vol. 13, no. 3, p. 036020, May 2016.

- [190] A. Liu, M. Vöröslakos, G. Kronberg, S. Henin, M. R. Krause, Y. Huang, A. Opitz, A. Mehta, C. C. Pack, B. Krekelberg, A. Berényi, L. C. Parra, L. Melloni, O. Devinsky, and G. Buzsáki, "Immediate neurophysiological effects of transcranial electrical stimulation," *Nature Communications*, vol. 9, no. 1, Nov. 2018.
- [191] P. C. Miranda, A. Mekonnen, R. Salvador, and G. Ruffini, "The electric field in the cortex during transcranial current stimulation," *NeuroImage*, vol. 70, pp. 48–58, Apr. 2013.
- [192] R. Polania, M. A. Nitsche, and C. C. Ruff, "Studying and modifying brain function with non-invasive brain stimulation," *Nature Neuroscience*, vol. 21, no. 2, pp. 174–187, Jan. 2018.
- [193] G. B. Saturnino, H. R. Siebner, A. Thielscher, and K. H. Madsen, "Accessibility of cortical regions to focal TES: Dependence on spatial position, safety, and practical constraints," *NeuroImage*, vol. 203, p. 116 183, Dec. 2019.
- [194] T. Allison, G. McCarthy, C. C. Wood, and S. J. Jones, "Potentials evoked in human and monkey cerebral cortex by stimulation of the median nerve," *Brain*, vol. 114, no. 6, pp. 2465–2503, 1991.
- [195] R. Hari, J. Karhu, M. Hämäläinen, J. Knuutila, O. Salonen, M. Sams, and V. Vilkmán, "Functional organization of the human first and second somatosensory cortices: A neuromagnetic study," *European Journal of Neuroscience*, vol. 5, no. 6, pp. 724–734, Jun. 1993.
- [196] Ü. Aydin, S. Rampp, A. Wollbrink, H. Kugel, J. -H. Cho, T. R. Knösche, C. Grova, J. Wellmer, and C. H. Wolters, "Zoomed MRI guided by combined EEG/MEG source analysis: A multimodal approach for optimizing presurgical epilepsy work-up and its application in a multifocal epilepsy patient case study," *Brain Topography*, vol. 30, no. 4, pp. 417–433, May 2017.
- [197] Ü. Aydin, J. Vorwerk, M. Dümpelmann, P. Küpper, H. Kugel, M. Heers, J. Wellmer, C. Kellinghaus, J. Haueisen, S. Rampp, H. Stefan, and C. H. Wolters, "Combined EEG/MEG can outperform single modality EEG or MEG source reconstruction in presurgical epilepsy diagnosis," *PLOS ONE*, vol. 10, no. 3, D. Marinazzo, Ed., e0118753, Mar. 2015.
- [198] A. Baltus, S. Wagner, C. H. Wolters, and C. S. Herrmann, "Optimized auditory transcranial alternating current stimulation improves individual auditory temporal resolution," *Brain Stimulation*, vol. 11, no. 1, pp. 118–124, Jan. 2018.
- [199] J. K. Rice, C. Rorden, J. S. Little, and L. C. Parra, "Subject position affects EEG magnitudes," *NeuroImage*, vol. 64, pp. 476–484, Jan. 2013.
- [200] M. Jenkinson, C. F. Beckmann, T. E. Behrens, M. W. Woolrich, and S. M. Smith, "FSL," *NeuroImage*, vol. 62, no. 2, pp. 782–790, Aug. 2012.

- [201] B. Lanfer, M. Scherg, M. Dannhauer, T. Knösche, M. Burger, and C. Wolters, "Influences of skull segmentation inaccuracies on EEG source analysis," *NeuroImage*, vol. 62, no. 1, pp. 418–431, Aug. 2012.
- [202] C. Ramon, P. Schimpf, J. Haueisen, M. Holmes, and A. Ishimaru, "Role of soft bone, CSF and gray matter in EEG simulations," *Brain Topography*, vol. 16, no. 4, pp. 245–248, 2004.
- [203] S. Baumann, D. Wozny, S. Kelly, and F. Meno, "The electrical conductivity of human cerebrospinal fluid at body temperature," *IEEE Transactions on Biomedical Engineering*, vol. 44, no. 3, pp. 220–223, Mar. 1997.
- [204] T. Medani, D. Lautru, D. Schwartz, Z. Ren, and G. Sou, "FEM method for the EEG forward problem and improvement based on modification of the saint venant's method," *Progress In Electromagnetics Research*, vol. 153, pp. 11–22, 2015.
- [205] S. Lew, C. Wolters, T. Dierkes, C. Röer, and R. MacLeod, "Accuracy and run-time comparison for different potential approaches and iterative solvers in finite element method based EEG source analysis," *Applied Numerical Mathematics*, vol. 59, no. 8, pp. 1970–1988, Aug. 2009.
- [206] C. Wolters, M. Kuhn, A. Anwander, and S. Reitzinger, "A parallel algebraic multigrid solver for finite element method based source localization in the human brain," *Computing and Visualization in Science*, vol. 5, no. 3, pp. 165–177, Dec. 2002.
- [207] T. Götz, R. Huonker, O. W. Witte, and J. Haueisen, "Thalamocortical impulse propagation and information transfer in EEG and MEG," *Journal of Clinical Neurophysiology*, vol. 31, no. 3, pp. 253–260, Jun. 2014.
- [208] R. Kakigi, "Somatosensory evoked magnetic fields following median nerve stimulation," *Neuroscience Research*, vol. 20, no. 2, pp. 165–174, Aug. 1994.
- [209] M. C. Piastra, A. Nüßing, J. Vorwerk, M. Clerc, C. Engwer, and C. H. Wolters, "A comprehensive study on electroencephalography and magnetoencephalography sensitivity to cortical and subcortical sources," *Human Brain Mapping*, vol. 42, no. 4, pp. 978–992, Nov. 2020.
- [210] A. Rezaei, M. Antonakakis, M. Piastra, C. H. Wolters, and S. Pursiainen, "Parametrizing the conditionally gaussian prior model for source localization with reference to the p20/n20 component of median nerve SEP/SEF," *Brain Sciences*, vol. 10, no. 12, p. 934, Dec. 2021.
- [211] R. J. Sadleir, T. D. Vannorsdall, D. J. Schretlen, and B. Gordon, "Transcranial direct current stimulation (tDCS) in a realistic head model," *NeuroImage*, vol. 51, no. 4, pp. 1310–1318, Jul. 2010.
- [212] S. Pursiainen, B. Agsten, S. Wagner, and C. H. Wolters, "Advanced boundary electrode modeling for tES and parallel tES/EEG," *IEEE Transactions on Neural Systems and Rehabilitation Engineering*, vol. 26, no. 1, pp. 37–44, Jan. 2018.

- [213] A. Khan, M. Antonakakis, N. Vogenauer, J. Haueisen, and C. H. Wolters, "Individually optimized multi-channel tDCS for targeting somatosensory cortex," *Clinical Neurophysiology*, vol. 134, pp. 9–26, Feb. 2022.
- [214] H. S., *Comparison of optimization approaches in high-definition transcranial current stimulation in the mammalian brain*, 2016.
- [215] M. Grant and S. Boyd, *CVX: Matlab software for disciplined convex programming, version 2.1*, <http://cvxr.com/cvx>, Mar. 2014.
- [216] D. Yang, Q. Wang, C. Xu, F. Fang, J. Fan, L. Li, Q. Du, R. Zhang, Y. Wang, Y. Lin, Z. Huang, H. Wang, C. Chen, Q. Xu, Y. Wang, Y. Zhang, Z. Zhang, X. Zhao, X. Zhao, T. Li, C. Liu, Y. Niu, Q. Zhou, Q. Zhou, Y. Duan, X. Liu, T. Yu, Q. Xue, J. Li, X. Dai, J. Han, C. Ren, H. Xu, N. Li, J. Zhang, N. Xu, K. Yang, and Y. Wang, "Transcranial direct current stimulation reduces seizure frequency in patients with refractory focal epilepsy: A randomized, double-blind, sham-controlled, and three-arm parallel multicenter study," *Brain Stimulation*, vol. 13, no. 1, pp. 109–116, Jan. 2020.
- [217] R. Campbell, *Notboxplot*, <https://github.com/raacampbell/notBoxPlot>, Sep. 2022.
- [218] J. P. Dmochowski, L. Koessler, A. M. Norcia, M. Bikson, and L. C. Parra, "Optimal use of EEG recordings to target active brain areas with transcranial electrical stimulation," *NeuroImage*, vol. 157, pp. 69–80, Aug. 2017.
- [219] F. Guarienti, W. Caumo, P. Shiozawa, Q. Cordeiro, P. S. Boggio, I. M. Benseñor, P. A. Lotufo, M. Bikson, and A. R. Brunoni, "Reducing transcranial direct current stimulation-induced erythema with skin pretreatment: Considerations for sham-controlled clinical trials," *Neuro-modulation: Technology at the Neural Interface*, vol. 18, no. 4, pp. 261–265, Sep. 2014.
- [220] J. L. McFadden, J. J. Borckardt, M. S. George, and W. Beam, "Reducing procedural pain and discomfort associated with transcranial direct current stimulation," *Brain Stimulation*, vol. 4, no. 1, pp. 38–42, Jan. 2011.
- [221] M. Bikson, P. Grossman, C. Thomas, A. L. Zannou, J. Jiang, T. Adnan, A. P. Mourdoukoutas, G. Kronberg, D. Truong, P. Boggio, A. R. Brunoni, L. Charvet, F. Fregni, B. Fritsch, B. Gillick, R. H. Hamilton, B. M. Hampstead, R. Jankord, A. Kirton, H. Knotkova, D. Liebetanz, A. Liu, C. Loo, M. A. Nitsche, J. Reis, J. D. Richardson, A. Rotenberg, P. E. Turkeltaub, and A. J. Woods, "Safety of transcranial direct current stimulation: Evidence based update 2016," *Brain Stimulation*, vol. 9, no. 5, pp. 641–661, Sep. 2016.
- [222] F. H. Kasten, K. Duecker, M. C. Maack, A. Meiser, and C. S. Herrmann, "Integrating electric field modeling and neuroimaging to explain inter-individual variability of tACS effects," *Nature Communications*, vol. 10, no. 1, Nov. 2019.

- [223] C. Y. Looi, J. Lim, F. Sella, S. Lolliot, M. Duta, A. A. Avramenko, and R. C. Kadosh, "Transcranial random noise stimulation and cognitive training to improve learning and cognition of the atypically developing brain: A pilot study," *Scientific Reports*, vol. 7, no. 1, Jul. 2017.
- [224] M. Splittgerber, R. Salvador, H. Brauer, C. Breitling-Ziegler, A. Prehn-Kristensen, K. Krauel, R. Nowak, G. Ruffini, V. Moliadze, and M. Siniatchkin, "Individual baseline performance and electrode montage impact on the effects of anodal tDCS over the left dorsolateral prefrontal cortex," *Frontiers in Human Neuroscience*, vol. 14, Sep. 2020.
- [225] A. Kuck, D. F. Stegeman, and E. H. F. van Asseldonk, "Modeling trans-spinal direct current stimulation for the modulation of the lumbar spinal motor pathways," *Journal of Neural Engineering*, vol. 14, no. 5, p. 056014, Sep. 2017.
- [226] D. Fischer, P. Fried, G. Ruffini, O. Ripolles, R. Salvador, J. Banus, W. Ketchabaw, E. Santarnecchi, A. Pascual-Leone, and M. Fox, "Multifocal tDCS targeting the resting state motor network increases cortical excitability beyond traditional tDCS targeting unilateral motor cortex," *NeuroImage*, vol. 157, pp. 34–44, Aug. 2017.
- [227] F. Neri, L. Mencarelli, A. Menardi, F. Giovannelli, S. Rossi, G. Sprugnoli, A. Rossi, A. Pascual-Leone, R. Salvador, G. Ruffini, and E. Santarnecchi, "A novel tDCS sham approach based on model-driven controlled shunting," *Brain Stimulation*, vol. 13, no. 2, pp. 507–516, Mar. 2020.
- [228] H. Kirimoto, K. Ogata, H. Onishi, M. Oyama, Y. Goto, and S. Tobimatsu, "Transcranial direct current stimulation over the motor association cortex induces plastic changes in ipsilateral primary motor and somatosensory cortices," *Clinical Neurophysiology*, vol. 122, no. 4, pp. 777–783, Apr. 2011.
- [229] M. F. M. Zulkifly, A. Lehr, D. van de Velden, A. Khan, N. K. Focke, C. H. Wolters, and W. Paulus, "Directionality of the injected current targeting the p20/n20 source determines the efficacy of 140 hz transcranial alternating current stimulation (tACS)-induced aftereffects in the somatosensory cortex," *PLOS ONE*, vol. 17, no. 3, P. Schwenkreis, Ed., e0266107, Mar. 2022.
- [230] J. E. Desmedt and C. Tomberg, "Mapping early somatosensory evoked potentials in selective attention: Critical evaluation of control conditions used for titrating by difference the cognitive p30, p40, p100 and n140," *Electroencephalography and Clinical Neurophysiology/Evoked Potentials Section*, vol. 74, no. 5, pp. 321–346, Sep. 1989.
- [231] R. C. Josiassen, C. Shagass, R. A. Roemer, S. Slepner, and B. Czartorysky, "Early cognitive components of somatosensory event-related potentials," *International Journal of Psychophysiology*, vol. 9, no. 2, pp. 139–149, Sep. 1990.

- [232] V. Jääntti, E. Sonkajärvi, S. Mustola, S. Rytky, P. Kiiski, and K. Suominen, "Single-sweep cortical somatosensory evoked potentials: N20 and evoked bursts in sevoflurane anaesthesia," *Electroencephalography and Clinical Neurophysiology/Evoked Potentials Section*, vol. 108, no. 3, pp. 320–324, Apr. 1998.
- [233] R. Oostenveld, P. Fries, E. Maris, and J.-M. Schoffelen, "FieldTrip: Open source software for advanced analysis of MEG, EEG, and invasive electrophysiological data," *Computational Intelligence and Neuroscience*, vol. 2011, pp. 1–9, 2011.
- [234] J. T. Francis, B. J. Gluckman, and S. J. Schiff, "Sensitivity of neurons to weak electric fields," *The Journal of Neuroscience*, vol. 23, no. 19, pp. 7255–7261, Aug. 2003.
- [235] F. Fröhlich and D. A. McCormick, "Endogenous electric fields may guide neocortical network activity," *Neuron*, vol. 67, no. 1, pp. 129–143, Jul. 2010.
- [236] J. K. Deans, A. D. Powell, and J. G. R. Jefferys, "Sensitivity of coherent oscillations in rat hippocampus to AC electric fields," *The Journal of Physiology*, vol. 583, no. 2, pp. 555–565, Aug. 2007.
- [237] B. Sehm, M. Hoff, C. Gundlach, M. Taubert, V. Conde, A. Villringer, and P. Ragert, "A novel ring electrode setup for the recording of somatosensory evoked potentials during transcranial direct current stimulation (tDCS)," *Journal of Neuroscience Methods*, vol. 212, no. 2, pp. 234–236, Jan. 2013.
- [238] G. B. Saturnino, A. Antunes, and A. Thielscher, "On the importance of electrode parameters for shaping electric field patterns generated by tDCS," *NeuroImage*, vol. 120, pp. 25–35, Oct. 2015.
- [239] S. Pursiainen, F. Lucka, and C. H. Wolters, "Complete electrode model in EEG: Relationship and differences to the point electrode model," *Physics in Medicine and Biology*, vol. 57, no. 4, pp. 999–1017, Feb. 2012.
- [240] H. Buchner, T. D. Waberski, M. Fuchs, R. Drenckhahn, M. Wagner, and H.-A. Wichmann, "Postcentral origin of p22: Evidence from source reconstruction in a realistically shaped head model and from a patient with a postcentral lesion," *Electroencephalography and Clinical Neurophysiology/Evoked Potentials Section*, vol. 100, no. 4, pp. 332–342, Jul. 1996.
- [241] A. Woods, A. Antal, M. Bikson, P. Boggio, A. Brunoni, P. Celnik, L. Cohen, F. Fregni, C. Herrmann, E. Kappenman, H. Knotkova, D. Liebetanz, C. Miniussi, P. Miranda, W. Paulus, A. Priori, D. Reato, C. Stagg, N. Wenderoth, and M. Nitsche, "A technical guide to tDCS, and related non-invasive brain stimulation tools," *Clinical Neurophysiology*, vol. 127, no. 2, pp. 1031–1048, Feb. 2016.
- [242] L. M. Li, K. Uehara, and T. Hanakawa, "The contribution of interindividual factors to variability of response in transcranial direct current stimulation studies," *Frontiers in Cellular Neuroscience*, vol. 9, May 2015.

- [243] J.-O. Radecke, A. Khan, A. K. Engel, C. H. Wolters, and T. R. Schneider, "Individual targeting increases control over inter-individual variability in simulated transcranial electric fields," *IEEE Access*, vol. 8, pp. 182 610–182 624, 2020.
- [244] G. Nolte, "MEG and EEG Toolbox of Hamburg (METH)," *Computational Intelligence and Neuroscience*, vol. 2011, pp. 1–9, 2011.
- [245] Y. Huang, J. P. Dmochowski, Y. Su, A. Datta, C. Rorden, and L. C. Parra, "Automated MRI segmentation for individualized modeling of current flow in the human head," *Journal of Neural Engineering*, vol. 10, no. 6, p. 066 004, Oct. 2013.
- [246] J. D. Nielsen, K. H. Madsen, O. Puonti, H. R. Siebner, C. Bauer, C. G. Madsen, G. B. Saturnino, and A. Thielscher, "Automatic skull segmentation from MR images for realistic volume conductor models of the head: Assessment of the state-of-the-art," *NeuroImage*, vol. 174, pp. 587–598, Jul. 2018.
- [247] J. Vorwerk, C. Engwer, S. Pursiainen, and C. H. Wolters, "A mixed finite element method to solve the EEG forward problem," *IEEE Transactions on Medical Imaging*, vol. 36, no. 4, pp. 930–941, Apr. 2017.
- [248] C. Engwer, J. Vorwerk, J. Ludewig, and C. H. Wolters, "A discontinuous galerkin method to solve the EEG forward problem using the subtraction approach," *SIAM Journal on Scientific Computing*, vol. 39, no. 1, B138–B164, Jan. 2017.
- [249] N. Tzourio-Mazoyer, B. Landeau, D. Papathanassiou, F. Crivello, O. Etard, N. Delcroix, B. Mazoyer, and M. Joliot, "Automated anatomical labeling of activations in SPM using a macroscopic anatomical parcellation of the MNI MRI single-subject brain," *NeuroImage*, vol. 15, no. 1, pp. 273–289, Jan. 2002.
- [250] S. Holm, "A simple sequentially rejective multiple test procedure," *Scandinavian Journal of Statistics*, vol. 6, no. 2, pp. 65–70, 1979.
- [251] Y. Huang and L. C. Parra, "Can transcranial electric stimulation with multiple electrodes reach deep targets?" *Brain Stimulation*, vol. 12, no. 1, pp. 30–40, Jan. 2019.
- [252] A. Khan, J. Haueisen, C. H. Wolters, M. Antonakakis, N. Vogenauer, A. Wollbrink, S. Suntrup-Krueger, T. R. Schneider, C. S. Herrmann, M. Nitsche, and W. Paulus, "Constrained maximum intensity optimized multi-electrode tDCS targeting of human somatosensory network," in *2019 41st Annual International Conference of the IEEE Engineering in Medicine and Biology Society (EMBC)*, IEEE, Jul. 2019.
- [253] A. Datta, V. Bansal, J. Diaz, J. Patel, D. Reato, and M. Bikson, "Gyri-precise head model of transcranial direct current stimulation: Improved spatial focality using a ring electrode versus conventional rectangular pad," *Brain Stimulation*, vol. 2, no. 4, 201–207.e1, Oct. 2009.

- [254] S. Rampersad, B. Roig-Solvas, M. Yarossi, P. P. Kulkarni, E. Santarnecchi, A. D. Dorval, and D. H. Brooks, "Prospects for transcranial temporal interference stimulation in humans: A computational study," *NeuroImage*, vol. 202, p. 116 124, Nov. 2019.
- [255] N. M. Boayue, G. Csifcsák, O. Puonti, A. Thielscher, and M. Mittner, "Head models of healthy and depressed adults for simulating the electric fields of non-invasive electric brain stimulation," *F1000Research*, vol. 7, p. 704, Nov. 2018.
- [256] A. Datta, D. Truong, P. Minhas, L. C. Parra, and M. Bikson, "Inter-individual variation during transcranial direct current stimulation and normalization of dose using MRI-derived computational models," *Frontiers in Psychiatry*, vol. 3, 2012.
- [257] D. Reato, A. Rahman, M. Bikson, and L. C. Parra, "Effects of weak transcranial alternating current stimulation on brain activity—a review of known mechanisms from animal studies," *Frontiers in Human Neuroscience*, vol. 7, 2013.
- [258] T. Neuling, S. Rach, and C. S. Herrmann, "Orchestrating neuronal networks: Sustained after-effects of transcranial alternating current stimulation depend upon brain states," *Frontiers in Human Neuroscience*, vol. 7, 2013.
- [259] S. Alagapan, S. L. Schmidt, J. Lefebvre, E. Hadar, H. W. Shin, and F. Fröhlich, "Modulation of cortical oscillations by low-frequency direct cortical stimulation is state-dependent," *PLOS Biology*, vol. 14, no. 3, O. Jensen, Ed., e1002424, Mar. 2016.
- [260] L. Johnson, I. Alekseichuk, J. Krieg, A. Doyle, Y. Yu, J. Vitek, M. Johnson, and A. Opitz, "Dose-dependent effects of transcranial alternating current stimulation on spike timing in awake nonhuman primates," *Science Advances*, vol. 6, no. 36, eaaz2747, Sep. 2020.
- [261] A. Antal and C. S. Herrmann, "Transcranial alternating current and random noise stimulation: Possible mechanisms," *Neural Plasticity*, vol. 2016, pp. 1–12, 2016.
- [262] L. Chen, X. Zou, R. Tang, A. Ke, and J. He, "Effect of electrode-electrolyte spatial mismatch on transcranial direct current stimulation: A finite element modeling study," *Journal of Neural Engineering*, vol. 16, no. 5, p. 056 012, Aug. 2019.
- [263] S. Ramaraju, M. A. Roula, and P. W. McCarthy, "Modelling the effect of electrode displacement on transcranial direct current stimulation (tDCS)," *Journal of Neural Engineering*, vol. 15, no. 1, p. 016 019, Jan. 2018.
- [264] S. Pursiainen, S. Lew, and C. H. Wolters, "Forward and inverse effects of the complete electrode model in neonatal EEG," *Journal of Neurophysiology*, vol. 117, no. 3, pp. 876–884, Mar. 2017.

- [265] N. Grossman, D. Bono, N. Dedic, S. B. Kodandaramaiah, A. Rudenko, H.-J. Suk, A. M. Cassara, E. Neufeld, N. Kuster, L.-H. Tsai, A. Pascual-Leone, and E. S. Boyden, "Noninvasive deep brain stimulation via temporally interfering electric fields," *Cell*, vol. 169, no. 6, 1029–1041.e16, Jun. 2017.
- [266] J. Jiang, D. Q. Truong, Z. Esmaeilpour, Y. Huang, B. W. Badran, and M. Bikson, "Enhanced tES and tDCS computational models by meninges emulation," *Journal of Neural Engineering*, vol. 17, no. 1, p. 016 027, Jan. 2020.
- [267] C. Ramon, P. Garguilo, E. A. Fridgerisson, and J. Haueisen, "Changes in scalp potentials and spatial smoothing effects of inclusion of dura layer in human head models for EEG simulations," *Frontiers in Neuro-engineering*, vol. 7, Aug. 2014.
- [268] L. Fiederer, J. Vorwerk, F. Lucka, M. Dannhauer, S. Yang, M. Dümpelmann, A. Schulze-Bonhage, A. Aertsen, O. Speck, C. Wolters, and T. Ball, "The role of blood vessels in high-resolution volume conductor head modeling of EEG," *NeuroImage*, vol. 128, pp. 193–208, Mar. 2016.
- [269] C. A. Bossetti, M. J. Birdno, and W. M. Grill, "Analysis of the quasi-static approximation for calculating potentials generated by neural stimulation," *Journal of Neural Engineering*, vol. 5, no. 1, pp. 44–53, Dec. 2007.
- [270] E. Kaufmann, M. Hordt, M. Lauseker, U. Palm, and S. Noachtar, "Acute effects of spaced cathodal transcranial direct current stimulation in drug resistant focal epilepsies.," *Clinical neurophysiology : official journal of the International Federation of Clinical Neurophysiology*, vol. 132, no. 7, pp. 1444–1451, Jul. 2021.
- [271] F. Kaiser, *Optimization of transcranial electrical stimulation montages to reduce seizure frequency and severity in patients with refractory focal epilepsy*, 2022.
- [272] S. Schrader, M. Antonakakis, S. Rampp, C. Engwer, and C. H. Wolters, "A novel method for calibrating head models to account for variability in conductivity and its evaluation in a sphere model," *Physics in Medicine & Biology*, vol. 65, no. 24, p. 245 043, Dec. 2020.